

Effect of the Air Plasma Spray Process on Rare Earth Silicate Coating Life

A Dissertation

Presented to

the faculty of the School of Engineering and Applied Science

University of Virginia

in partial fulfillment
of the requirements for the degree

Doctor of Philosophy

by

Cory G Parker

May 2020

APPROVAL SHEET

This Dissertation
is submitted in partial fulfillment of the requirements
for the degree of
Doctor of Philosophy

Author Signature: Cory Packer

This Dissertation has been read and approved by the examining committee:

Advisor: Elizabeth Opila

Committee Member: Robert Kelly

Committee Member: John Ihlefeld

Committee Member: Patrick Hopkins

Committee Member: Veena Tikare, PhD

Committee Member: _____

Accepted for the School of Engineering and Applied Science:



Craig H. Benson, School of Engineering and Applied Science

May 2020

All science would be superfluous if the outward appearance and the essence of things directly coincided.

Karl Marx, Capital, Volume III (edited by Fredrich Engels), 1894

Acknowledgements

I would like to thank Rolls-Royce Corporation and program managers Dr. Kang Lee and Dr. Stephanie Gong for funding this research. Thank you to Beth Opila for her guidance and understanding throughout my PhD. Thank you to my committee for their helpful comments. Much of this research would not have been possible without help from Jeroen Deijkers and Dr. Haydn Wadley, who were instrumental in the fabrication of APS $Y_2Si_2O_7$. Dr. Rick Weber and MDI and Dr. Chris Benmore at Argonne National Laboratory were instrumental in the success of the high-temperature X-ray diffraction portion of my research. Many conversations with Dr. Rob Golden allowed for the alteration of the steam-jet furnace that drove the results of Chapter 3. Thank you to Dr. Veena Tikare and Dr. John Mitchell at Sandia National Laboratories for their guidance through SPPARKS and the modeling process. Thank you to all members of the NMCF at UVA for their knowledge and support with characterizing my materials. I'd like to thank all current and former members of the Opila Lab Group for making the laboratory atmosphere supportive and exciting. I'd finally like to thank my family, friends, and therapist for their love and support over the 6 years I've been at UVA. I would not have been able to finish this research without them, especially my parents, my brother, Bekah Webster, Lavina Backman, Laura Duke, and Sarah D'Onofrio.

Abstract

SiC/SiC ceramic matrix composites (CMCs) entered commercial jet turbine service in 2016. SiC forms a protective SiO₂ layer at operating temperatures in oxidizing environments, however, H₂O(g) produced in the combustion environment reacts with the SiO₂ layer to form Si(OH)₄(g). Environmental barrier coatings (EBCs) are required to protect the underlying CMC from H₂O(g) in the combustion stream. Rare earth (RE) disilicate (RE₂Si₂O₇) coatings, where RE is either Y or Yb, are state-of-the-art EBCs. These coatings are typically deposited using an air plasma spray (APS) process resulting in a heterogeneous microstructure with multiple phases present such as RE₂O₃, RE₂SiO₅, and RE₂Si₂O₇. Cracks and pores are also likely to result from this process. This complex microstructure results in thermal expansion and thermochemical response to H₂O(g) that differ from homogeneous RE₂Si₂O₇ materials processed in conventional ways. The aim of this research is to quantify property differences that arise due to the APS process and incorporate them into a lifing model to predict EBC behavior at temperatures, pressures, gas velocities, and times relevant for turbine engine applications.

Thermal expansion of Y₂Si₂O₇ material deposited using APS was measured by dilatometry at temperatures between 25 and 1400°C. APS Y₂Si₂O₇ had a coefficient of thermal expansion (CTE) higher than phase pure Y₂Si₂O₇ tested in the same manner, likely due to the presence of constituent phases such as Y₂O₃ and Y₂SiO₅ that have CTE values higher than Y₂Si₂O₇. In addition, anisotropy in CTE was determined for δ-Y₂Si₂O₇, X2-Y₂SiO₅, β-Yb₂Si₂O₇, and X2-Yb₂SiO₅ using high-temperature XRD performed at the Advanced Photon Source at Argonne National Laboratory. Low expansion planes were found along with large differences in expansion along different axes, especially in the monosilicates.

The thermochemical stability of RE₂Si₂O₇ is an important factor in the lifetime prediction of EBCs for SiC/SiC CMCs. Samples of Y₂Si₂O₇ processed with SPS have been exposed to H₂O(g) with a gas velocity of 125-250 m/s at 1200 and 1300°C for 60h and 1400°C for times of 60 – 250 h in a steam-jet furnace. Samples were then observed in plan view and cross section using scanning electron microscopy (SEM) and energy dispersive spectroscopy (EDS). Phase pure SPS Y₂Si₂O₇ reacted with H₂O(g) forming Y₂SiO₅ and porosity, releasing Si(OH)₄(g). Analysis of the change in Y₂SiO₅ layer thickness with time has shown parabolic reaction kinetics, suggesting a diffusion limited mechanism. For the first time the reaction of Y₂SiO₅ with H₂O(g) to form Y₂O₃ was also observed. APS Yb₂Si₂O₇ provided by Rolls-Royce was tested in the steam-jet furnace as well, showing reaction between H₂O(g) and Yb₂Si₂O₇ similar to that seen in the Y₂O₃-SiO₂ system. Local microstructural features in the APS coatings, such as splats, cracks, and pores, were found to heavily influence SiO₂ depletion.

A hybrid Potts/diffusion model of the phase and microstructural evolution was developed. Currently the model simulates the formation of Y_2SiO_5 and porosity from phase pure $Y_2Si_2O_7$ with parabolic kinetics. Once calibrated, the model will be used to predict $Y_2Si_2O_7$ reactions with $H_2O(g)$ and the corresponding microstructural evolution as a function of time, temperature, P_{H_2O} and gas velocity. The model also allows for the introduction of new phases like the formation of Y_2O_3 from Y_2SiO_5 reacting with $H_2O(g)$ and pores and cracks in the microstructure.

This work together will give a better understanding of how the APS process used in EBC deposition alters material properties compared to phase pure materials and how these alterations must be considered for lifetime prediction of the coatings.

Contents

1	Introduction	1
1.1	Rare Earth Environmental Barrier Coatings	1
1.1.1	RE ₂ O ₃ -SiO ₂ Systems Overview	2
1.2	Thermal Expansion of Rare Earth Silicates	7
1.3	Thermochemical Stability of Rare Earth Silicates in Water Vapor	8
1.3.1	Dense Phase Pure Y ₂ Si ₂ O ₇ Thermochemical Stability in High Temperature, High Velocity Water Vapor	9
1.4	Thermochemical Model of Phase and Microstructural Evolution	12
1.5	Overview of Dissertation Research Objectives and Results	12
2	Thermal Expansion of Rare Earth Silicates	14
2.1	Objectives	14
2.2	Experimental	14
2.2.1	Materials	14
2.2.2	Characterization	15
2.3	Results	17
2.3.1	XRD of APS Y ₂ Si ₂ O ₇	17
2.3.2	SEM Phase Contrast Analysis of APS Y ₂ Si ₂ O ₇	18
2.3.3	DSC and Dilatometry of APS Y ₂ Si ₂ O ₇	19
2.3.4	High Temperature XRD of Y and Yb mono- and disilicates	22
2.4	Discussion	29
2.4.1	APS Y ₂ Si ₂ O ₇	29
2.4.2	High Temperature XRD of Y and Yb mono- and disilicates	30
2.5	Conclusions	33
2.6	Recommendations for Future Work	33

3 Thermochemical Stability of Phase Pure and Air Plasma Sprayed Rare Earth Silicates in High-Temperature, High-Velocity Water Vapor	34
3.1 Objectives	34
3.2 Experimental	35
3.2.1 Material	35
3.2.2 Steam-jet Furnace	35
3.2.3 Characterization	38
3.3 Results	39
3.3.1 Stability of Phases in the Y_2O_3 - SiO_2 System at $1400^\circ C$	40
3.3.2 Time Dependence of SiO_2 Depletion in Dense Phase Pure $Y_2Si_2O_7$ at $1400^\circ C$	49
3.3.3 Temperature Dependence of SiO_2 Depletion in Dense Phase Pure $Y_2Si_2O_7$	51
3.3.4 Velocity Dependence of SiO_2 Depletion in Dense Phase Pure $Y_2Si_2O_7$	53
3.3.5 Effect of APS on SiO_2 Depletion Kinetics and Microstructural Evolution	54
3.4 Discussion	65
3.4.1 SiO_2 Volatility	65
3.4.2 Time Dependence of the Reaction Between $H_2O(g)$ and $Y_2Si_2O_7$	66
3.4.3 Temperature Dependence of the Reaction Between $H_2O(g)$ and $Y_2Si_2O_7$	66
3.4.4 Effect of Velocity on SiO_2 Volatility in Disilicates	68
3.4.5 Possible Mechanisms for the Formation of Dense Monosilicate Layers	69
3.4.6 Stability of Y_2O_3	70
3.4.7 Air Plasma Sprayed $Yb_2Si_2O_7$ Microstructure and Kinetics of SiO_2 Depletion	71
3.5 Conclusions	72
3.6 Recommendations for Future Work	73
4 Lifetime Modeling of EBC Thermochemical Stability in High-Temperature, High-Velocity Water Vapor	75
4.1 Objectives	75
4.2 Methods	76
4.3 Results	80
4.4 Discussion	84
4.5 Conclusions	86
4.6 Recommendations for Future Work	87
5 Summary and Impact	88

List of Figures

1.1	Phase diagram of the Y_2O_3 - SiO_2 system for temperatures between 800 and 2600°C [8].	3
1.2	Phase diagram of the Yb_2O_3 - SiO_2 system for temperatures between 1500 and 2300°C [13]. . .	4
1.3	Stability diagram of polymorphs of $RE_2Si_2O_7$ compared to the ionic radius of the rare earth cation from 800 to 1800°C. Reproduced from Turcer, using data from Felsche [15] [14].	4
1.4	Crystal structures of the polymorphs in the $RE_2Si_2O_7$ and RE_2SiO_5 systems. $Y_2Si_2O_7$ exhibits all of the shown polymorphs, while $Yb_2Si_2O_7$ only exhibits β . Y_2SiO_5 shows both the X1 and X2 polymorphs, but only X2 exists for Yb_2SiO_5 [17].	5
1.5	Schematic of an APS torch with temperatures and velocities of the torch flame. Figure courtesy of Deijkers, Wadley.	6
1.6	BSE cross-sectional micrograph of annealed Y_2SiO_5 APS coating as-fabricated. Note the large amount of cracks, splat boundaries, and mixture of phases. [18]	7
1.7	Backscatter secondary electron (BSE) image of the initial surface of a $Y_2Si_2O_7$ sample after spark plasma sintering (SPS) processing. The light triangle is a piece of ZrO_2 left over from the ball milling process. Initial grain size is $\sim 12\mu m$. [12]	10
1.8	BSE images in plan view of SPS phase pure $Y_2Si_2O_7$ samples after 60, 125, and 250 hours at 1200°C in 1 atm of $H_2O(g)$ with gas velocity of 158 - 174 m/s from left to right. All samples show complete transformation of the surface to Y_2SiO_5 . Note the coarsening of the Y_2SiO_5 grains and the pore structure.	10
1.9	BSE images in cross-section of phase pure $Y_2Si_2O_7$ samples after 60, 125, and 250 hours at 1200°C in 1 atm of $H_2O(g)$ with gas velocity of 158 - 174 m/s from left to right. Uniform SiO_2 depletion to form Y_2SiO_5 is observed. The layer thickness increases with time [12].	11

1.10	Weight loss vs. \sqrt{t} for a dense phase pure $Y_2Si_2O_7$ sample exposed over 250 hours with intermittent removal at 1200°C in 1 atm of $H_2O(g)$ with gas velocity of 168 m/s shows excellent agreement with the parabolic rate law. The red lines represent when a new fused quartz capillary was inserted. Reproduced from Golden [12].	11
2.1	A schematic of the experimental setup for high temperature XRD of RE silicates on the beamline. Figure courtesy of Rachel Guarriello.	16
2.2	A photograph of beamline hutch 6ID-D at the Advanced Photon Source of Argonne National Laboratory.	16
2.3	XRD patterns of as-received, as-sprayed, and post-anneal $Y_2Si_2O_7$ material. Note that the patterns for as-received and post-anneal are different. Y_2SiO_5 , α , and ζ $Y_2Si_2O_7$ appear after annealing at 1200°C for 20h.	17
2.4	BSE plan view image of a typical as-processed $Y_2Si_2O_7$ APS microstructure with surface polish. Note the four phase features present: 1. SiO_2 -poor regions 2. $RE_2Si_2O_7$ 3. phases with middling SiO_2 content 4. porosity.	18
2.5	A BSE cross-sectional image of an as-processed APS $Y_2Si_2O_7$ sample. Large amounts of cracking and porosity, along with a variety of phases, are present.	19
2.6	Contrast thresholding analysis of Figure 2.5 to estimate phase and defect content. Black in each figure represents the constituent being identified.	19
2.7	Heat flow vs. temperature for unannealed APS $Y_2Si_2O_7$ obtained by DSC. A crystallization peak was observed at 1050°C.	20
2.8	$\delta l/L_0$ vs. temperature for unannealed APS $Y_2Si_2O_7$. The sample reduces in length during crystallization at 1050°C.	20
2.9	Dilatometry results of linear CTE vs. temperature for phase pure SPS $Y_2Si_2O_7$ and Y_2SiO_5 as well as three successive runs of one sample of APS $Y_2Si_2O_7$ that had been annealed at 1200°C for 20h.	21
2.10	A comparison of the XRD results for $Y_2Si_2O_7$ APS material after each processing and testing step. The relative intensity of the two highest intensity peaks for β - $Y_2Si_2O_7$ change between annealing and the first dilatometry measurement. Polymorphs of $Y_2Si_2O_7$ such as α and δ are no longer measurable after a second annealing. Phase identification was done on peaks with an intensity $\geq 10\%$ of the maximum intensity.	21
2.11	X-ray diffraction pattern of $Yb_2Si_2O_7$ measured at Argonne National Laboratory from room temperature to 1700°C.	22

2.12 X-ray diffraction pattern of Yb_2SiO_5 measured at Argonne National Laboratory from room temperature to 1800°C	22
2.13 X-ray diffraction pattern of $\text{Y}_2\text{Si}_2\text{O}_7$ measured at Argonne National Laboratory from room temperature to 1800°C	23
2.14 X-ray diffraction pattern of Y_2SiO_5 measured at Argonne National Laboratory from room temperature to 1900°C	23
2.15 The monoclinic crystal structure of $\text{Yb}_2\text{Si}_2\text{O}_7$, matched to high-temperature XRD patterns. The teal atoms are Yb, blue atoms are Si, and the red atoms are O.	24
2.16 The monoclinic crystal structure of Yb_2SiO_5 , matched to high-temperature XRD patterns. The teal atoms are Yb, blue atoms are Si, and the red atoms are O.	24
2.17 The orthorhombic δ polymorph of $\text{Y}_2\text{Si}_2\text{O}_7$, matched to high-temperature XRD patterns. The green atoms are Y, the blue atoms are Si, and the red atoms are O.	25
2.18 The monoclinic X2 polymorph of Y_2SiO_5 , matched to high-temperature XRD patterns. The green atoms are Y, the blue atoms are Si, and the red atoms are O.	25
2.19 The x_T/x_0 values of a, b, c, β , and volume parameters of the $\text{Yb}_2\text{Si}_2\text{O}_7$ crystal measured vs temperature. Each parameter value is normalized with respect to that parameter value at room temperature.	26
2.20 The x_T/x_0 values of a, b, c, β , and volume parameters of the Yb_2SiO_5 crystal measured vs temperature. Each parameter value is normalized with respect to that parameter value at room temperature.	26
2.21 The x_T/x_0 values of a, b, c, and volume parameters of the δ $\text{Y}_2\text{Si}_2\text{O}_7$ crystal measured vs temperature. Each parameter value is normalized with respect to that parameter value at room temperature.	27
2.22 The x_T/x_0 values of a, b, c, β , and volume parameters of the X2 Y_2SiO_5 crystal measured vs temperature. Each parameter value is normalized with respect to that parameter value at room temperature.	27
2.23 CTE ellipsoid output from CTEAS software for β - $\text{Yb}_2\text{Si}_2\text{O}_7$ at 1500°C . As this is a monoclinic structure the Z axis is parallel to the c crystallographic direction in the structure, while the X and Y axes are not parallel to the a and b directions.	28
2.24 CTE ellipsoid output from CTEAS software for X2- Yb_2SiO_5 at 1500°C . As this is a monoclinic structure the Z axis is parallel to the c crystallographic direction in the structure, while the X and Y axes are not parallel to the a and b directions.	28

2.25	CTE ellipsoid output from CTEAS software for δ -Y ₂ Si ₂ O ₇ at 1500°C. The δ polymorph is orthorhombic, and so all three axes are parallel to the three crystallographic directions. . . .	29
2.26	CTE ellipsoid output from CTEAS software for X2-Y ₂ SiO ₅ at 1500°C. As this is a monoclinic structure the Z axis is parallel to the c crystallographic direction in the structure, while the X and Y axes are not parallel to the a and b directions.	29
3.1	A schematic drawing of the steam-jet furnace (top) and details of the sample holder.	36
3.2	A velocity profile on the surface of a sample tested in the steam-jet at 1400°C with an assumed deionized water flow rate of 2.0 mL/min. This velocity distribution was modeled using ANSYS. The high velocity location represents the steam impingement point 1 mm from the capillary outlet.	37
3.3	XRD results for Y ₂ Si ₂ O ₇ and Y ₂ SiO ₅ before exposure and all samples after exposure at 1400°C for 60h. Note that the Y ₂ Si ₂ O ₇ sample after exposure shows only peaks from the surface layer of Y ₂ SiO ₅ product phase.	41
3.4	A surface profile map of a SiO ₂ sample exposed in the steam-jet furnace with 1 atm H ₂ O(g) at 1400°C for 60h. There is a large amount of signal dropout in the impingement site area due to the depth of the impingement site. The few data points collected come from the edges of pits measured at the bottom of the impingement site.	41
3.5	A line profile for SiO ₂ , exposed in the steam-jet furnace with 1 atm H ₂ O(g) at 1400°C for 60h, created from the surface profile map shown in Figure 3.4. The points show the areas of measured data in the impingement site. The dotted line is an interpolation from these points.	42
3.6	A line profile of the depth of recession of SiO ₂ exposed in the steam-jet furnace with 1 atm H ₂ O(g) at 1400°C for 60h obtained from contact profilometry.	42
3.7	A surface profile map of a SiO ₂ sample exposed in the steam-jet furnace with 1 atm H ₂ O(g) at 1400°C for 8h. Signal dropout (yellow areas) is observed.	42
3.8	A line profile for SiO ₂ , exposed in the steam-jet furnace with 1 atm H ₂ O(g) at 1400°C for 8h, created from the surface profile map shown in Figure 3.7. More data were obtained here as compared to Figure 3.5.	43
3.9	A contact profile of the surface of the SiO ₂ sample exposed at 1400°C for 8h in the steam-jet furnace.	43
3.10	A backscattered electron SEM plan view image of the as-processed microstructure of SPS Y ₂ Si ₂ O ₇ . ZrO ₂ contamination from the milling media can be seen in the pore as the brightest phase, pointed out by the blue arrow.	44

3.11	A backscattered electron SEM plan view image of SPS $Y_2Si_2O_7$ exposed in the steam-jet furnace at 1400°C for 60 h with $\text{PH}_2\text{O} = 1$ atm and $v_g = 195$ m/s. Y_2SiO_5 is the only phase visible at this location, with pores forming from the volume change that occurred upon reaction of $Y_2Si_2O_7$ with $\text{H}_2\text{O}(\text{g})$	45
3.12	A backscattered electron SEM cross-sectional image of SPS $Y_2Si_2O_7$ exposed in the steam-jet furnace at 1400°C for 60 h with $\text{PH}_2\text{O} = 1$ atm and $v_g = 180$ m/s.	45
3.13	A backscattered electron SEM cross-sectional image of SPS $Y_2Si_2O_7$ exposed in the steam-jet furnace at 1400°C for 60 h with $\text{PH}_2\text{O} = 1$ atm and $v_g = 225$ m/s.	45
3.14	A backscattered electron SEM cross-sectional image of SPS $Y_2Si_2O_7$ exposed in the steam-jet furnace at 1400°C for 60 h with $\text{PH}_2\text{O} = 1$ atm and $v_g = 200$ m/s. This higher magnification image shows the Y_2O_3 formation on the surface from Figure 3.13.	46
3.15	A backscattered electron SEM plan view image of SPS Y_2SiO_5 exposed in the steam-jet furnace at 1400°C for 60 h with $\text{PH}_2\text{O} = 1$ atm and $v_g = 10$ m/s.	46
3.16	A backscattered electron SEM plan view image of SPS Y_2SiO_5 exposed in the steam-jet furnace at 1400°C for 60 h with $\text{PH}_2\text{O} = 1$ atm and $v_g = 195$ m/s.	47
3.17	A backscattered electron SEM plan view image of SPS Y_2SiO_5 exposed in the steam-jet furnace at 1400°C for 60 h with $\text{PH}_2\text{O} = 1$ atm and $v_g = 150$ m/s. A clear boundary can be observed between the formation of Y_2O_3 on the left and the original Y_2SiO_5 on the right.	47
3.18	A backscattered electron SEM cross-sectional image of SPS Y_2SiO_5 exposed in the steam-jet furnace at 1400°C for 60 h with $\text{PH}_2\text{O} = 1$ atm and $v_g = 195$ m/s.	48
3.19	A backscattered electron SEM image of Y_2O_3 exposed in a stagnant air box furnace at 1400°C for 24 h.	48
3.20	A backscattered electron SEM image of Y_2O_3 exposed in the steam-jet furnace at 1400°C for 60 h with $\text{PH}_2\text{O} = 1$ atm and $v_g = 225$ m/s.	49
3.21	A surface map obtained from optical profilometry showing no loss of material in the impingement area of the Y_2O_3 sample.	49
3.22	A line profile obtained from Figure 3.21 showing a maximum height difference of $2\ \mu\text{m}$ on the surface of the Y_2O_3 sample.	49
3.23	A comparison of backscattered electron cross-sectional images showing the SiO_2 depletion depth for dense, phase pure $Y_2Si_2O_7$ samples exposed at 1400°C for 60 (a), 125 (b), and 250h (c). Average gas velocity in these figures is 130-170 m/s.	50

3.24 Average SiO ₂ depletion depth vs $t^{1/2}$ for phase pure Y ₂ Si ₂ O ₇ samples exposed in the steam-jet furnace at 1400°C for 60, 125, and 250h with v_g between 150 and 175 m/s. The dotted line is the linear fit to these data.	50
3.25 A comparison of backscattered electron images taken 1 mm downstream of the impingement site showing the surface morphology change for dense, phase pure Y ₂ Si ₂ O ₇ samples exposed at 1200 ($v_g = 175$ m/s) (a), 1300 ($v_g = 185$ m/s) (b), and 1400°C ($v_g = 195$ m/s) (c) for 60h. The red dot on image a corresponds to the location of the EDS spectrum shown in Figure 3.26. 51	51
3.26 EDS spectrum taken at the location designated by the red dot in Figure 3.25. The Y:Si ratio in these microstructural features is approximately 5, which does not match with any equilibrium phase in the SiO ₂ - Y ₂ O ₃ system. The large peak at 0 keV is a measurement artifact.	52
3.27 A comparison of backscattered electron images taken in cross-section showing the depletion depth for dense, phase pure Y ₂ Si ₂ O ₇ samples exposed at 1200 (a), 1300 (b), and 1400°C (c) for 60h with v_g between 150 and 170 m/s.	53
3.28 Average SiO ₂ depletion depth vs. temperature for dense, phase pure Y ₂ Si ₂ O ₇ samples exposed in the steam-jet furnace at 1200, 1300, and 1400°C for 60h with v_g between 150 and 170 m/s. Results from steam-jet exposures carried out using a fused quartz capillary at 1200°C for 60h by Rob Golden (UVA) are shown in red [12].	53
3.29 $\ln(\text{recession rate}^2)$ vs. $10000/T$ for phase pure Y ₂ Si ₂ O ₇ exposed at 1200, 1300, and 1400°C for 60h, $v_g = 150$ -170 m/s, with a linear fit to the data. The calculated E_a is 382 ± 34 kJ/mol with a 95% confidence interval.	54
3.30 Backscattered electron images showing the change in depletion depth and morphology of dense, phase pure Y ₂ Si ₂ O ₇ tested at 1400°C for 60h with approximate velocities of 150 (a), 200 (b), and 240 m/s (c).	54
3.31 A backscattered electron image showing the polished surface in plan view of dense APS Yb ₂ Si ₂ O ₇ coatings provided by Rolls-Royce.	55
3.32 A backscattered electron image showing the initial morphology and splat structure in polished cross-section of dense APS Yb ₂ Si ₂ O ₇ coatings provided by Rolls-Royce.	55
3.33 A collection of backscattered electron images showing the surface morphology of 1 mm downstream of the impingement site on dense APS Yb ₂ Si ₂ O ₇ coatings exposed at 1200 ($v_g = 175$ m/s), 1300 ($v_g = 185$ m/s), and 1400°C ($v_g = 195$ m/s) for 60, 125, and 250h.	57
3.34 A backscattered electron image showing the typical material loss (erosion) experienced at the steam impingement site by dense APS Yb ₂ Si ₂ O ₇ coatings exposed in the steam-jet furnace at 1400°C for 60h. The $v_g = 250$ m/s at the center of the impingement site.	58

3.35	Stitched backscattered electron images showing material loss (erosion) experienced at the steam impingement site by dense APS $\text{Yb}_2\text{Si}_2\text{O}_7$ coatings exposed in the steam-jet furnace at 1200°C for 250h. The highest v_g experienced in this area was 230 m/s.	58
3.36	Backscattered electron images showing representative cross-sections on APS $\text{Yb}_2\text{Si}_2\text{O}_7$ coatings exposed at 1200, 1300, and 1400°C for 60, 125, and 250h with v_g between 150 and 200 m/s represented here. The steam-exposed surface is on the right side of all images.	59
3.37	XRD results for APS $\text{Yb}_2\text{Si}_2\text{O}_7$ as-received as well as after exposure in the steam-jet furnace for 125h at 1200, 1300, and 1400°C. After exposure in the steam-jet furnace the dominant phase present is Yb_2SiO_5 at all temperatures. Yb_2O_3 becomes more abundant with increasing temperature.	60
3.38	A backscattered electron image showing the complex microstructure of the depletion layer that results from local cracks, blue arrow, and pores found in a dense APS $\text{Yb}_2\text{Si}_2\text{O}_7$ coatings exposed in the steam-jet furnace at 1400°C for 125h with an approximate surface gas velocity of 190 m/s. The red circle denotes an area of unreacted coated surrounded by Yb_2SiO_5 formed from several reaction fronts due to these local microstructures.	60
3.39	A backscattered electron image showing an example of an SiO_2 -poor splat, blue arrow, from the initial processing of the APS coating arresting progress of the depletion layer in a dense APS $\text{Yb}_2\text{Si}_2\text{O}_7$ coatings exposed in the steam-jet furnace at 1300°C for 125h with a surface gas velocity of approximately 150 m/s.	61
3.40	A backscattered electron image showing the polished morphology in plan view of porous APS $\text{Yb}_2\text{Si}_2\text{O}_7$ coatings provided by Rolls-Royce.	62
3.41	A collection of backscattered electron images showing the surface morphology of 1 mm downstream of the impingement site on porous APS $\text{Yb}_2\text{Si}_2\text{O}_7$ coatings exposed at 1200 ($v_g = 175$ m/s), 1300 ($v_g = 185$ m/s), and 1400°C ($v_g = 195$ m/s) for 60, 125, and 250h.	63
3.42	A collection of backscattered electron images showing the cross-sectional morphology on porous APS $\text{Yb}_2\text{Si}_2\text{O}_7$ coatings exposed at 1200, 1300, and 1400°C for 60, 125, and 250h with v_g between 150 and 200 m/s represented here. The steam-exposed surface is on the right side of all images.	64
3.43	Average SiO_2 depletion depth vs. temperature for phase pure $\text{Y}_2\text{Si}_2\text{O}_7$ exposed at 1000, 1100, 1200, and 1400°C for 125h.	67

3.44	The natural log of (depletion rate) ² plotted against inverse temperature for phase pure Y ₂ Si ₂ O ₇ exposed in the steam-jet furnace at 1000 - 1400°C for 60 and 125h. The activation energy for depletion at 125h is higher, 461 ± 47 kJ/mol within a 95% confidence interval, compared to at 60h, 382 ± 34 kJ/mol. This suggests that the activation energy of the reaction between Y ₂ Si ₂ O ₇ and H ₂ O(g) increases with time. The depletion mechanism seems to change between 1000 and 1100°C, as there is a discontinuity in the data at 1100°C.	67
4.1	A simplified example in 2D of neighboring grains interacting and possibly coarsening. The green hashed cell in bolded black is the cell considered in the example described in the text. .	77
4.2	A simplified example of a solid grain neighboring a pore and surface diffusion occurring. The solid grain (either RE ₂ Si ₂ O ₇ or RE ₂ SiO ₅) is yellow and the pore is black. The example shown here does not change the energy of the system.	78
4.3	A simplified example of a reaction between RE ₂ Si ₂ O ₇ and H ₂ O(g) that occurs in the model presented in 2D. The red cells indicate the highest concentration of Si(OH) ₄ (g). After the reaction between H ₂ O(g) and RE ₂ Si ₂ O ₇ has occurred the new gas site has a high concentration of Si(OH) ₄ (g). This will then diffuse out of the system.	78
4.4	Still images from a Version 1 simulation animation of the RE ₂ Si ₂ O ₇ EBC coating reacting with water vapor resulting in linear reaction kinetics. Time steps are 50, 100, 200, moving from left to right. The initial simulation box was simply a single RE ₂ Si ₂ O ₇ grain with several elements of gas states above. Black areas are RE ₂ Si ₂ O ₇ , gray areas are different grains of RE ₂ SiO ₅ , and the colors represent Si(OH) ₄ (g) partial pressures.	80
4.5	Still images from a Version 2 simulation animation of the RE ₂ Si ₂ O ₇ EBC coating reacting with water vapor resulting in parabolic reaction kinetics. Time steps are 50, 1000, 5000, moving from left to right. The initial simulation box was simply a single RE ₂ Si ₂ O ₇ grain with several elements of gas states above. Black areas are RE ₂ Si ₂ O ₇ , gray areas are different grains of RE ₂ SiO ₅ , and the colors represent Si(OH) ₄ (g) partial pressures.	81
4.6	Comparison of the Version 3 simulation after 100, 500, and 1000 steps. The gas boundary layer saturates over time. Black areas are RE ₂ Si ₂ O ₇ , gray areas are different grains of RE ₂ SiO ₅ , and the colors represent Si(OH) ₄ (g) partial pressures.	81
4.7	A comparison of a cropped in view of each Version 3 simulation box showing the pore detail over time. Black areas are RE ₂ Si ₂ O ₇ , gray areas are different grains of RE ₂ SiO ₅ , and the colors represent Si(OH) ₄ (g) partial pressures.	82

- 4.8 Direct comparison between a backscattered electron cross-sectional image from an SPS $Y_2Si_2O_7$ sample exposed in the steam-jet furnace at 1200°C for 60h and a simulation after 500 steps. The experimental depletion depth is 6.5 μm over 60h, with the simulation depth being 80 sites. 83
- 4.9 Direct comparison between a backscattered electron cross-sectional image from an SPS $Y_2Si_2O_7$ sample exposed in the steam-jet furnace at 1200°C for 60h and a simulation after 500 steps. The experimental depletion depth is 6.3 μm over 60h, with the simulation depth being 80 sites. 83
- 4.10 Direct comparison between a backscattered electron cross-sectional image from an SPS $Y_2Si_2O_7$ sample exposed in the steam-jet furnace at 1200°C for 60h and a simulation after 500 steps. The experimental depletion depth is 5.7 μm over 60h, with the simulation depth being 80 sites. 84
- 4.11 Total number of RE_2SiO_5 sites present in the simulation plotted over number of timesteps. Left is Version 1, right is Version 2. 84
- 4.12 Total number of RE_2SiO_5 sites present in simulation Version 3 plotted over time steps. 85

List of Tables

1.1	Comparison of the properties of Y_2SiO_5 , $Y_2Si_2O_7$, Yb_2SiO_5 , and $Yb_2Si_2O_7$ as they relate to EBC considerations.	2
2.1	The CTE values calculated from the linear fit of the lattice parameter change values from 800-2000°C for each material.	23
2.2	Comparison of the CTE values for each principal crystallographic direction in the $X_2-Y_2SiO_5$ monoclinic cell between the current study and those done by O’Bryan and Fukuda [27] [28].	32
3.1	Parameters used in Equations 3.1 and 3.2 for SiO_2 volatility	39
3.2	Bounded experimental recession rate results of SiO_2 exposures to $H_2O(g)$ at 1400°C and a maximum gas velocity of 250 m/s compared to calculation.	43
3.3	Collected SiO_2 depletion measurements for phase pure $Y_2Si_2O_7$ samples exposed in the steam-jet at 1400°C for 60, 125, and 250h with a gas velocity of 130-170 m/s.	51
3.4	Collected SiO_2 depletion measurements for phase pure $Y_2Si_2O_7$ samples exposed in the steam-jet at 1200, 1300, and 1400°C for 60h with a gas velocity of 130-170 m/s.	52
3.5	Bounded experimental recession rate results of SiO_2 exposures to $H_2O(g)$ at 1400°C and a maximum gas velocity of 250 m/s compared to calculation. Reproduced here for convenience.	65

Chapter 1

Introduction

1.1 Rare Earth Environmental Barrier Coatings

SiC/SiC ceramic matrix composites (CMCs) entered service in commercial jet turbine engines as shrouds in 2016 [1]. These CMCs reduce weight compared to heavier nickel-base super alloys currently in use in jet turbines and allow for higher operating temperatures leading to greater operating efficiency. The stability of SiC/SiC CMCs in this environment is a key concern. SiC forms SiO₂ at the operating temperatures of the turbine. The combustion gas stream of the turbine contains H₂O(g) which reacts with SiO₂, to form the gaseous species Si(OH)₄(g) given in Equation 1 below.



This reaction causes unacceptable rates of material loss. The kinetics of the reaction were determined to be parabolic by Opila [2], with more work on the thermodynamics and gaseous diffusion done by Opila, Smialek, and Robinson [3] [4]. Rare earth (RE) silicate environmental barrier coatings (EBCs) are currently used to mitigate this reaction with water vapor.

The major considerations for EBC materials suitable for SiC/SiC CMCs include: 1. Chemical compatibility with the underlying substrate; 2. Coefficient of thermal expansion (CTE) that has reasonable agreement with SiC; 3. Slower reaction rate with H₂O(g) than thermally grown SiO₂; 4. Barrier to oxidant transport to the underlying material. RE silicates meet these requirements to some extent where RE elements considered for EBCs are Y and Yb [5] [6].

Table 1.1: Comparison of the properties of Y_2SiO_5 , $Y_2Si_2O_7$, Yb_2SiO_5 , and $Yb_2Si_2O_7$ as they relate to EBC considerations.

	Y_2SiO_5	$Y_2Si_2O_7$	Yb_2SiO_5	$Yb_2Si_2O_7$
Chemical Compatibility	adequate	good	adequate	good
CTE	fair	good	fair	good
Stability in Water Vapor	good	adequate	good	adequate
Oxidant Barrier	adequate	adequate		
Phase Stability	adequate	poor	good	good

1.1.1 RE_2O_3 - SiO_2 Systems Overview

The Y_2O_3 - SiO_2 system has the largest amount of physical and thermodynamic data available and, along with the Yb_2O_3 - SiO_2 system, is the focus of this proposal [7] [8] [9]. The phase diagram of the Y_2O_3 - SiO_2 system is shown below in Figure 1.1. The two line compounds, Y_2SiO_5 and $Y_2Si_2O_7$ are considered as candidate EBC materials and their ability to meet the EBC criteria is summarized in Table 1.1. Each of the criteria is introduced here and discussed fully in the following sections. Y_2SiO_5 can react with thermally grown SiO_2 from the substrate to form $Y_2Si_2O_7$, while $Y_2Si_2O_7$ has already been saturated with SiO_2 and so is more chemically compatible with the substrate. The CTE of $Y_2Si_2O_7$ is approximately 4-5 ppm/K, while the CTE of Y_2SiO_5 is 7-8 ppm/K, demonstrating that $Y_2Si_2O_7$ is a better CTE match with SiC, which has a CTE of 4.5-5.0 ppm/K. The activity of SiO_2 in the Y_2SiO_5 - $Y_2Si_2O_7$ two-phase region was determined to be 0.00089 while the activity of SiO_2 in the $Y_2Si_2O_7$ - SiO_2 two-phase region was determined to be 0.32 at 1400°C[8]. The enthalpy of formation and fusion, as well as the standard entropy of both Y_2SiO_5 and $Y_2Si_2O_7$ were assessed by Fabrichnaya and Mao [10] [11]. These data allow for determination of the ΔG° for a reaction between $Y_2Si_2O_7$ and $H_2O(g)$ to form Y_2SiO_5 . Finally, both phases have similar oxygen diffusivity [12], which are adequate for oxidant barrier. However, the air plasma spray (APS) process used to deposit these materials as coatings causes variations in all desired properties and so these effects must be explored and understood for accurate life prediction.

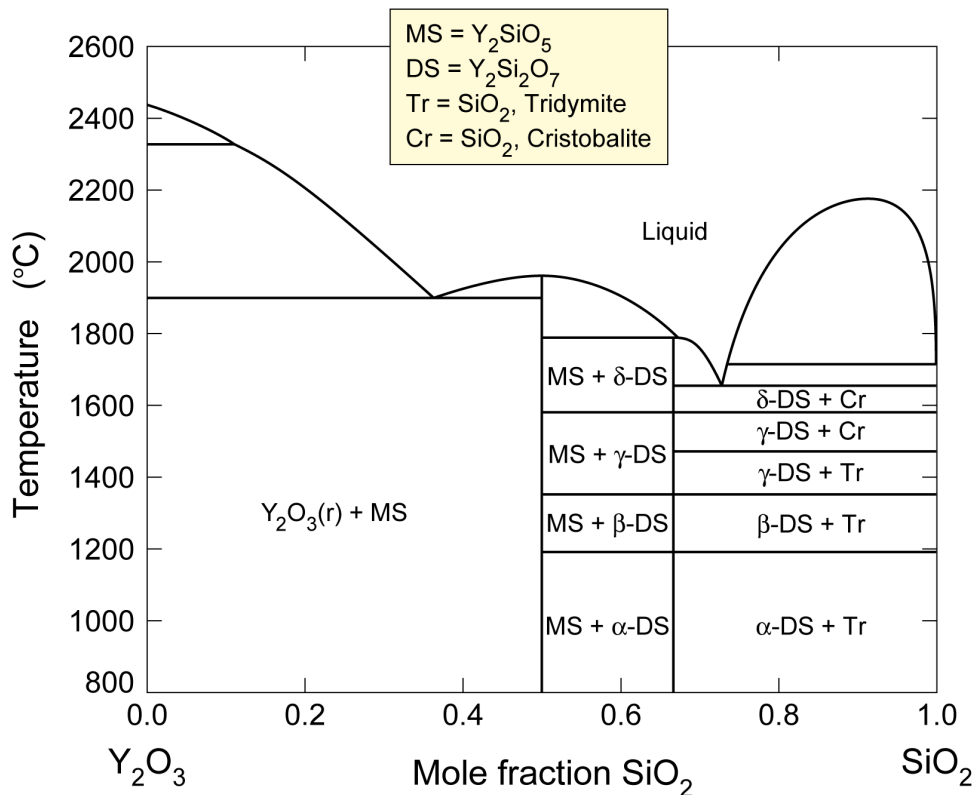


Figure 1.1: Phase diagram of the Y_2O_3 - SiO_2 system for temperatures between 800 and 2600°C [8].

The Yb_2O_3 - SiO_2 system has less fundamental data available, but the phase diagram, shown in Figure 1.2 [13], is similar to that of the yttrium counterpart. It is important to note that while $\text{Y}_2\text{Si}_2\text{O}_7$ has several polymorphs, shown in Figure 1.1 and discussed later, $\text{Yb}_2\text{Si}_2\text{O}_7$ does not have polymorphs, only exhibiting the β structure found by Felsche [14]. Figure 1.3 gives the stability regions of different $\text{RE}_2\text{Si}_2\text{O}_7$ polymorphs corresponding to the ionic radius of the RE elements [15]. $\text{Y}_2\text{Si}_2\text{O}_7$ exhibits four equilibrium polymorphs due to its larger ionic radius than Yb. A non-equilibrium phase of $\text{Y}_2\text{Si}_2\text{O}_7$, ζ , has been described and measured in the literature as well [16]. Yb_2SiO_5 also only exhibits one polymorph, X2, as opposed to Y_2SiO_5 which can be observed in the X1 and X2 structures. Figure 1.4 displays the crystal structure of α , β , γ , and δ $\text{RE}_2\text{Si}_2\text{O}_7$ as well as X1 and X2 RE_2SiO_5 [17]. All of these structures, except δ which is orthorhombic, are monoclinic. Costa and Jacobson determined the activity of SiO_2 in the Yb_2O_3 - Yb_2SiO_5 phase field to be 0.0027 at 1300°C and the activity of SiO_2 in the Yb_2SiO_5 - $\text{Yb}_2\text{Si}_2\text{O}_7$ phase field to be 0.36 at 1500°C. The activity of SiO_2 in the Yb_2SiO_5 - $\text{Yb}_2\text{Si}_2\text{O}_7$ field is similar to that of SiO_2 in the Y_2SiO_5 - $\text{Y}_2\text{Si}_2\text{O}_7$ field (0.32), however, the activity of SiO_2 in the Yb_2SiO_5 - $\text{Yb}_2\text{Si}_2\text{O}_7$ field is approximately 3 times larger than in the Y_2SiO_5 - $\text{Y}_2\text{Si}_2\text{O}_7$ field (0.00089). This suggests that Yb_2SiO_5 will more readily react with $\text{H}_2\text{O}(\text{g})$ than Y_2SiO_5 at high-temperatures.

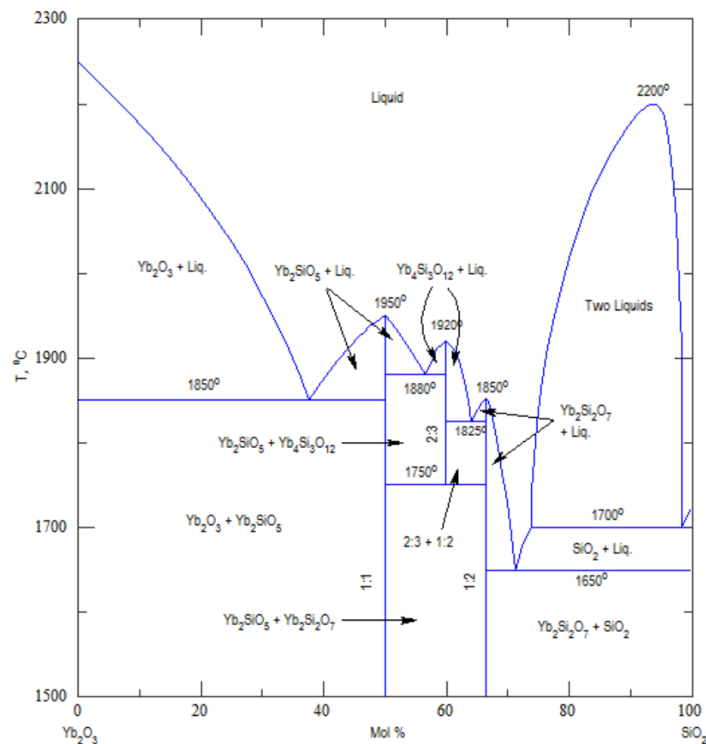


Figure 1.2: Phase diagram of the Yb₂O₃-SiO₂ system for temperatures between 1500 and 2300°C [13].

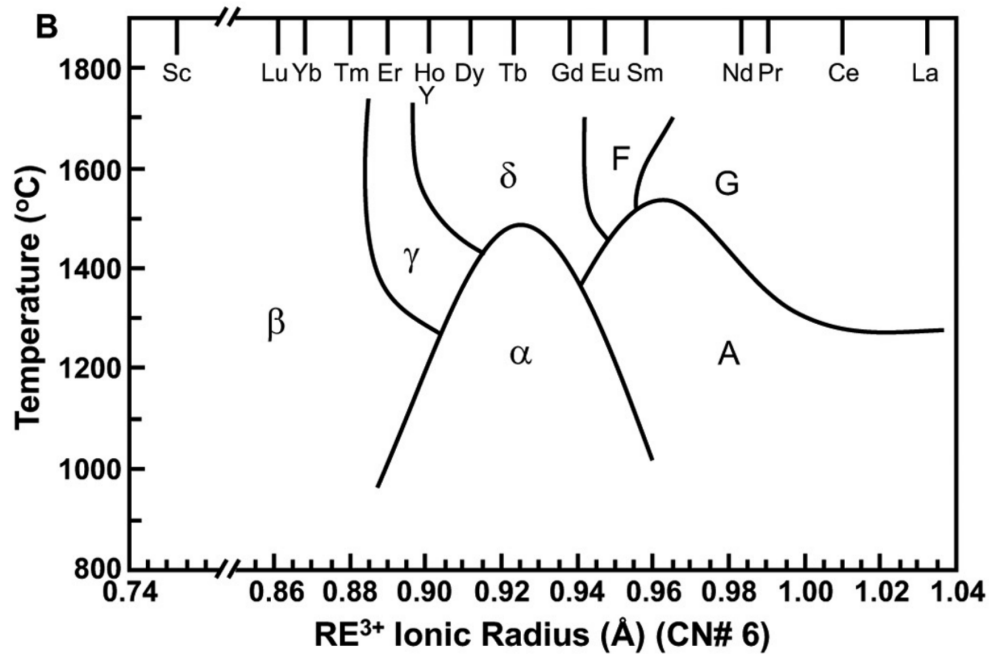


Figure 1.3: Stability diagram of polymorphs of RE₂Si₂O₇ compared to the ionic radius of the rare earth cation from 800 to 1800°C. Reproduced from Turcer, using data from Felsche [15] [14].

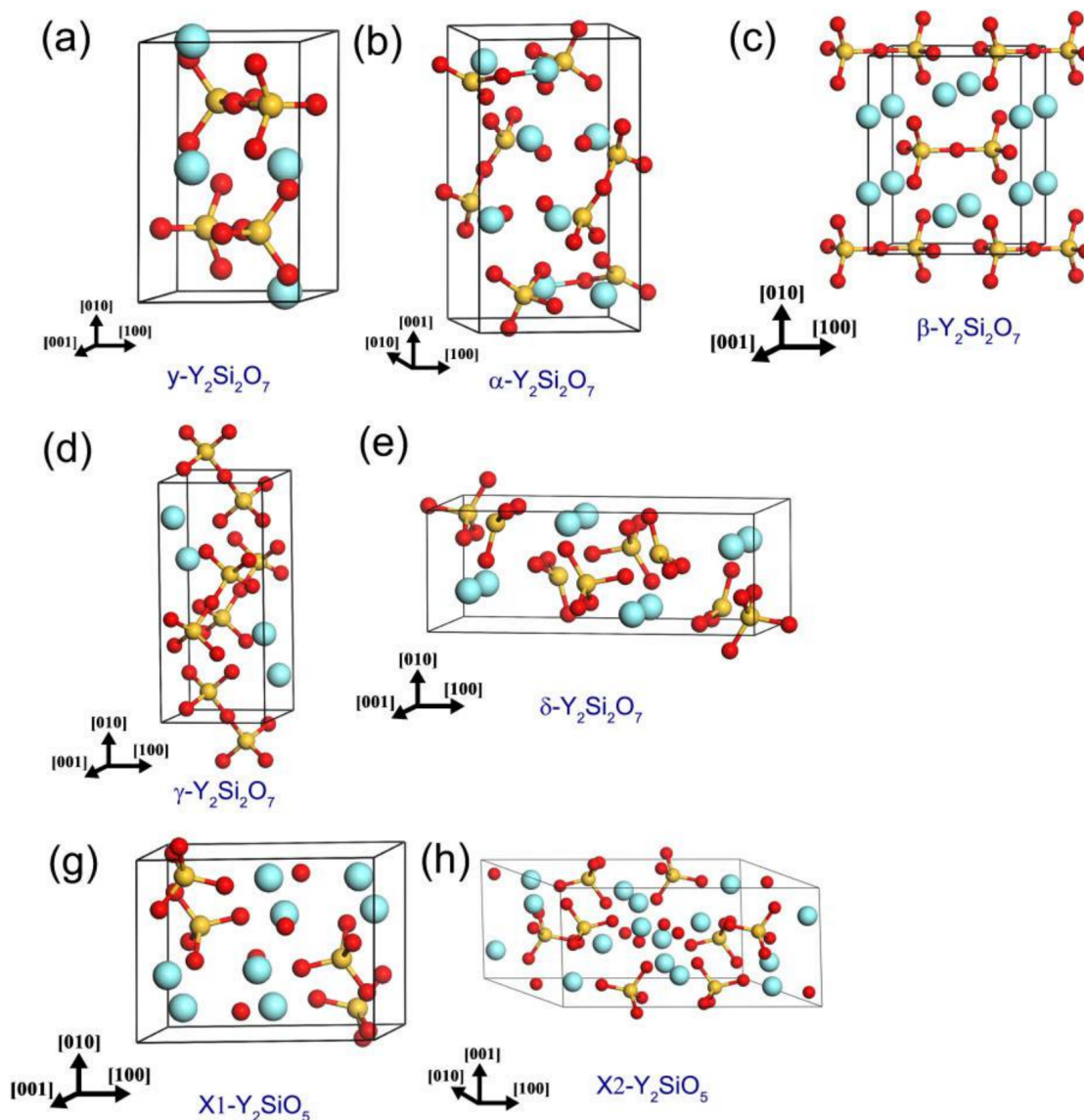


Figure 1.4: Crystal structures of the polymorphs in the $\text{RE}_2\text{Si}_2\text{O}_7$ and RE_2SiO_5 systems. $\text{Y}_2\text{Si}_2\text{O}_7$ exhibits all of the shown polymorphs, while $\text{Yb}_2\text{Si}_2\text{O}_7$ only exhibits β . Y_2SiO_5 shows both the X1 and X2 polymorphs, but only X2 exists for Yb_2SiO_5 [17].

Air Plasma Spray

Air plasma spray (APS) is a non-equilibrium line of sight thermal spray process used to quickly deposit material. A plasma is created using a high amperage anode and either hydrogen or helium. An illustration of the APS torch and parameters is shown in Figure 1.5. This plasma has a core temperature of $\sim 20000\text{K}$ with a steep temperature gradient. Powder is fed into this torch and then ejected into the plasma using high flow rates, on the order of hundreds of cubic feet per hour, of an inert gas such as argon. The inhomogeneous heating of the powders and variation in powder size results in a heterogeneous mixture of non-equilibrium

phases in the coating. Richards et al. characterized the spraying behavior of RE silicates with a focus on ytterbium silicates [18] [19] [20]. Richards described in detail the complex microstructure that results from a plasma spray process. Figure 1.6 below shows an example of a Yb_2SiO_5 APS microstructure with mud cracking, pores, and multiple phases present. Mud cracking was attributed to differences in CTE between the substrate and the coating. Mud cracks were also observed between phases in the coating layer as well. Thus it is expected that the thermal expansion, stability with water vapor, and ability to act as a diffusion barrier will all be substantially different than dense, phase-pure materials.

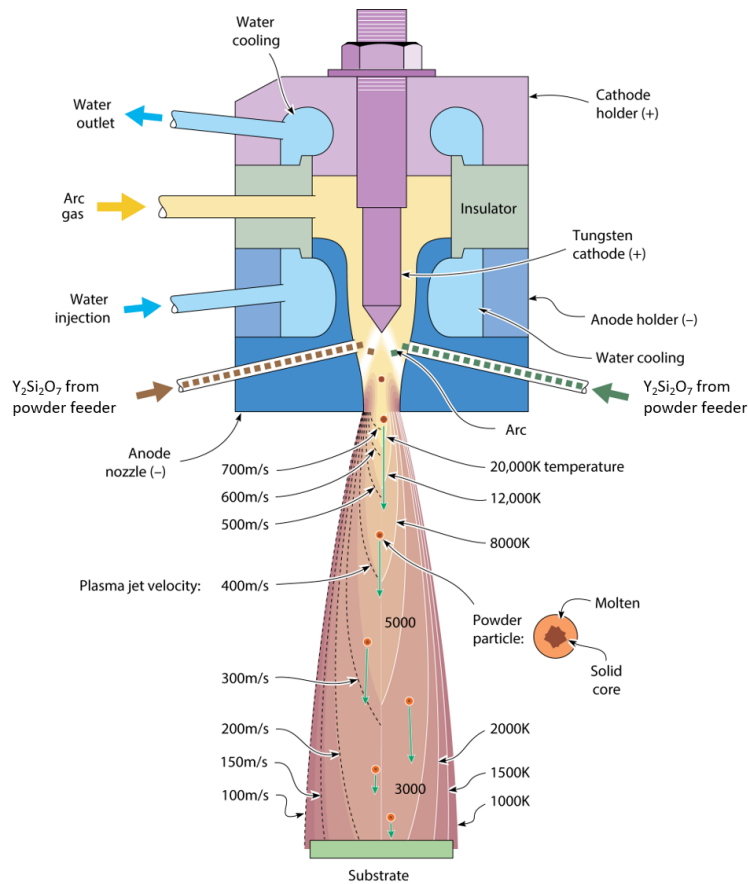


Figure 1.5: Schematic of an APS torch with temperatures and velocities of the torch flame. Figure courtesy of Deijkers, Wadley.

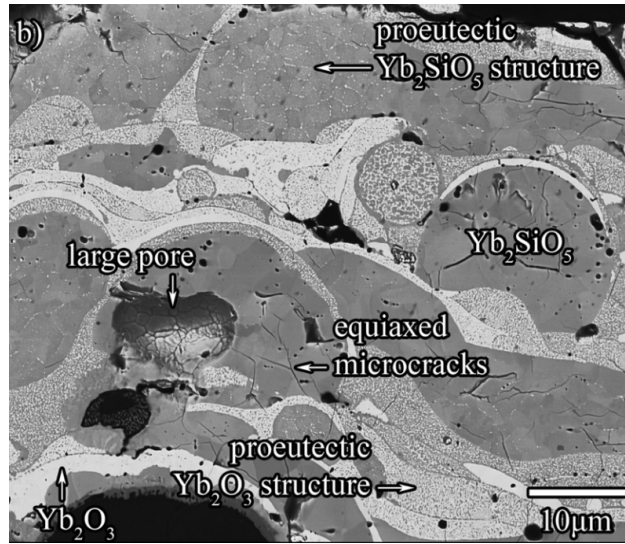


Figure 1.6: BSE cross-sectional micrograph of annealed Y_2SiO_5 APS coating as-fabricated. Note the large amount of cracks, splat boundaries, and mixture of phases. [18]

1.2 Thermal Expansion of Rare Earth Silicates

The CTE of Y_2SiO_5 is $8.36 \cdot 10^{-6}/K$ with little difference between the X1 and X2 polymorphs [17] [21]. $Y_2Si_2O_7$ has six polymorphs ($\alpha, \beta, \gamma, \delta, \eta$, and ζ), with the most commonly found being β and γ which have CTEs of 4.1 and $3.9 \cdot 10^{-6}/K$, respectively [22] [17] [23]. The measured CTE of α and δ are $8.0 \cdot 10^{-6}$ and $8.1 \cdot 10^{-6}/K$ respectively [24]. The reported CTE of SiC varies between $\sim 4.5 - 5.5 \cdot 10^{-6}/K$ [25]. With these values in mind, β and γ $Y_2Si_2O_7$ are the best CTE match for SiC, making it more thermomechanically compatible on temperature cycling than Y_2SiO_5 . However, it should be noted that the CTE values reported here are for phase pure materials, whether powders or bulk polycrystalline samples. X2- Yb_2SiO_5 ($7.2 \cdot 10^{-6}/K$) [26] and β - $Yb_2Si_2O_7$ ($\sim 4 \cdot 10^{-6}/K$) [15] have similar CTE values to their yttrium counterparts, however, the ytterbium silicates do not have polymorphs. The CTE of $Yb_2Si_2O_7$ is most similar to the β and γ polymorphs of $Y_2Si_2O_7$.

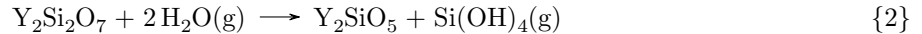
Sun et al. tabulated CTE values for $\alpha-, \beta-, \gamma,$ and δ - $Y_2Si_2O_7$ along with Y_2SiO_5 powders and polycrystalline samples. The CTE values for powder γ - $Y_2Si_2O_7$ vary from $2.2 - 3.9 \cdot 10^{-6}/K$ and polycrystalline Y_2SiO_5 ranges from $3.05 - 8.7 \cdot 10^{-6}/K$. Powder and bulk measurements reported in the literature often have differing CTE values and those obtained using high temperature XRD are not distinguished from those that are obtained using dilatometry. As such, variation of results due to polymorphs, processing, and measurement make the trustworthiness of CTE results uncertain. al Nasiri et al. found differences in literature values and their own measured CTE values for several monosilicates as well [26]. al Nasiri measured the

CTE of Y_2SiO_5 to be $6.9 \pm 0.2 \cdot 10^{-6}/K$, while in their own literature review measurements ranged from 6.0 to $8.7 \cdot 10^{-6}/K$.

It is important to note that, except for the δ -phase of $\text{Y}_2\text{Si}_2\text{O}_7$ which has an orthorhombic structure, all of these silicates have a monoclinic crystal structure. This means that a CTE anisotropy is expected for these structures. In fact, anisotropy of the thermal expansion of Y_2SiO_5 was measured by O'Bryan et al. over the range of 25 - 200°C and found thermal expansion of $0.6 \cdot 10^{-6}/K$ for [100] and $11.4 \cdot 10^{-6}/K$ for [001] [27]. Fukuda et al. have also studied the anisotropy of the Y_2SiO_5 crystal and found CTE values at 1000°C for the a, b, and c directions to be 8.1, 1.7, and $12.2 \cdot 10^{-6}/K$ respectively [28]. The thermal expansion and anisotropy of the four equilibrium polymorphs of $\text{Y}_2\text{Si}_2\text{O}_7$ were studied by Dolan et al. up to 1400°C, finding low expansion directions corresponding to the long axis of SiO_2 tetrahedra [24].

1.3 Thermochemical Stability of Rare Earth Silicates in Water Vapor

The reactions of the yttrium silicates with $\text{H}_2\text{O}(\text{g})$ are as follows:



$\text{Y}_2\text{Si}_2\text{O}_7$ reacts with $\text{H}_2\text{O}(\text{g})$ to form Y_2SiO_5 , accompanied by a 25% decrease in volume between $\text{Y}_2\text{Si}_2\text{O}_7$ and Y_2SiO_5 . As such, when $\text{Y}_2\text{Si}_2\text{O}_7$ reacts with $\text{H}_2\text{O}(\text{g})$ it forms a porous layer of Y_2SiO_5 that grows in thickness upon further exposure to $\text{H}_2\text{O}(\text{g})$ [29]. Similarly, Y_2SiO_5 reacts with $\text{H}_2\text{O}(\text{g})$ to form Y_2O_3 with an accompanying density change of 33%. The reaction between $\text{Y}_2\text{Si}_2\text{O}_7$ and $\text{H}_2\text{O}(\text{g})$ requires transport of $\text{H}_2\text{O}(\text{g})$ through the porous Y_2SiO_5 to the $\text{Y}_2\text{Si}_2\text{O}_7$. The current hypothesis for the rate controlling step of the reaction mechanism is the diffusion of $\text{Si}(\text{OH})_4(\text{g})$ away from the Y_2SiO_5 - $\text{Y}_2\text{Si}_2\text{O}_7$ interface [12]. Transport of $\text{H}_2\text{O}(\text{g})$ inward is not expected to be the rate limiting step because of the high $\text{H}_2\text{O}(\text{g})$ partial pressure available in the combustion stream in the turbine. The surface reaction is also not expected to limit the reaction at the high temperatures present in the turbine environment as parabolic kinetics have been observed previously in $\text{Y}_2\text{Si}_2\text{O}_7$ testing by Golden [12].

The water vapor stability of RE silicates as well as previous generation EBC materials such as mullite and BSAS has been studied. Fritsch tested dense phase pure material with $\text{H}_2\text{O}(\text{g})$ with gas velocities around

100 m/s. Testing was done in a burner rig setting with 0.27 atm $\text{H}_2\text{O}(\text{g})$ at atmospheric pressure. Both interrupted weight loss and final depletion measurements were made for the materials tested. Weight loss for $\text{Y}_2\text{Si}_2\text{O}_7$ was low, about 2.3×10^{-3} mg/cm²h with a recession rate of 6.6×10^{-3} $\mu\text{m}/\text{h}$ assuming linear kinetics at 1450°C. SEM analysis showed a porous structure of Y_2SiO_5 formed on top of dense $\text{Y}_2\text{Si}_2\text{O}_7$ [30] [31]. Previous generation coatings such as mullite showed weight loss and recession rates much higher, 3.79×10^{-2} mg/cm²h and 0.118 $\mu\text{m}/\text{h}$ in the Fritsch burner rig described previously [32].

Ueno carried out experiments on dense phase pure Yb and Lu silicate materials at moderate $\text{H}_2\text{O}(\text{g})$ velocities of 50 m/s with 1 atm partial pressure. $\text{Yb}_2\text{Si}_2\text{O}_7$ reacted with $\text{H}_2\text{O}(\text{g})$ to form Yb_2SiO_5 at 1300 - 1500°C, confirmed through XRD analysis of the samples after testing. No measurement of weight loss or recession depth was made for $\text{Yb}_2\text{Si}_2\text{O}_7$. $\text{Lu}_2\text{Si}_2\text{O}_7$ showed very similar results to $\text{Yb}_2\text{Si}_2\text{O}_7$ with a porous Lu_2SiO_5 microstructure forming on the surface of the sample. Grain sizes also decreased in this Lu_2SiO_5 area compared to the $\text{Lu}_2\text{Si}_2\text{O}_7$ that was unexposed [33] [34] [35].

Low velocity thermogravimetric analysis (TGA) was also completed by Lee et al. on BSAS as well as $\text{Yb}_2\text{Si}_2\text{O}_7$ and Yb_2SiO_5 [36] [37] [25]. These results showed a small amount of weight loss in the RE silicates and BSAS materials as the velocity of the $\text{H}_2\text{O}(\text{g})$ was ~ 4.4 cm/s. Cracking and oxidation of the Si bond coat was the major concern found with the silicate materials tested in these studies. Pore and glass formation was noted in the BSAS material along with reaction with bond layers between the BSAS top coat and the CMC substrate.

The literature discussed above provides information on the SiO_2 depletion behavior of mostly dense phase pure materials at velocities at or below 100 m/s. These conditions lack the combination of velocity and partial pressure of $\text{H}_2\text{O}(\text{g})$ found in a turbine.

1.3.1 Dense Phase Pure $\text{Y}_2\text{Si}_2\text{O}_7$ Thermochemical Stability in High Temperature, High Velocity Water Vapor

Dense phase pure $\text{Y}_2\text{Si}_2\text{O}_7$ stability in high temperature, high velocity steam was evaluated in a steam-jet furnace in prior work in this lab [12]. The initial condition of these materials can be seen in Figure 1.7. These results provide the baseline for comparison of heterogeneous APS material and are therefore summarized here.

Plan view micrographs of spark plasma sintered (SPS) phase pure $\text{Y}_2\text{Si}_2\text{O}_7$ samples after steam-jet exposure at 1200°C and times of 60-250 hours can be seen in Figure 1.8 below. Surface cracking as well as coarsening of both the resultant Y_2SiO_5 submicron sized grains and the pore structure of the sample are observed.

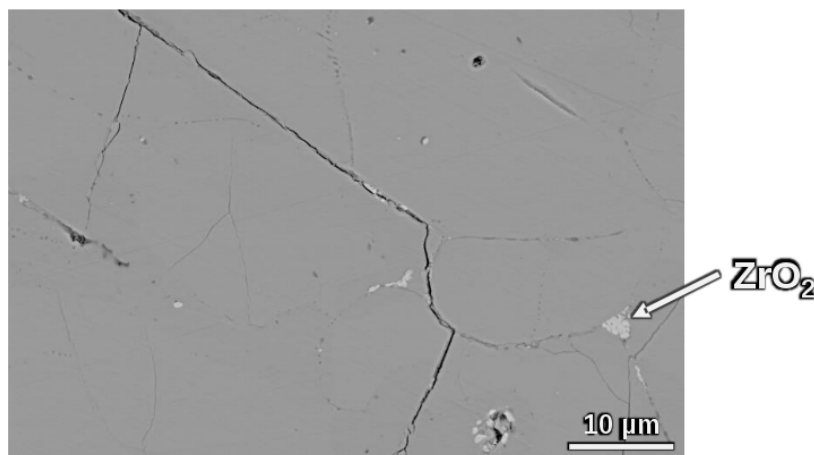


Figure 1.7: Backscatter secondary electron (BSE) image of the initial surface of a $\text{Y}_2\text{Si}_2\text{O}_7$ sample after spark plasma sintering (SPS) processing. The light triangle is a piece of ZrO_2 left over from the ball milling process. Initial grain size is $\sim 12\mu\text{m}$. [12]

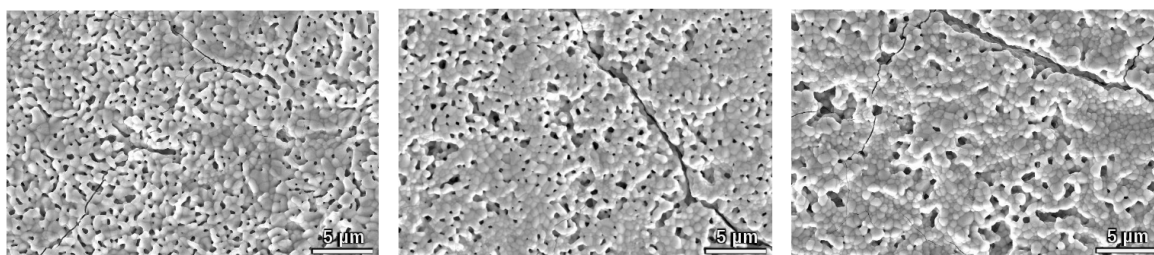


Figure 1.8: BSE images in plan view of SPS phase pure $\text{Y}_2\text{Si}_2\text{O}_7$ samples after 60, 125, and 250 hours at 1200°C in 1 atm of $\text{H}_2\text{O}(\text{g})$ with gas velocity of 158 - 174 m/s from left to right. All samples show complete transformation of the surface to Y_2SiO_5 . Note the coarsening of the Y_2SiO_5 grains and the pore structure.

Cross-sectional micrographs seen in Figure 1.9 show a clear reaction interface between Y_2SiO_5 and $\text{Y}_2\text{Si}_2\text{O}_7$. As samples are exposed for longer periods of time in high temperature high velocity steam the reaction layer of Y_2SiO_5 grows thicker. The porosity of the Y_2SiO_5 layer is also apparent in cross section.

Measurements of weight loss during an intermittent removal experiment on SPS $\text{Y}_2\text{Si}_2\text{O}_7$ show parabolic reaction kinetics for the reaction between $\text{Y}_2\text{Si}_2\text{O}_7$ and $\text{H}_2\text{O}(\text{g})$ as seen in Figure 1.10. Intermittent removal experiments show ~ 300 nm pores of rectangular cross-section are formed between grains. Over time these pores coalesce and coarsen into round structures. Y_2SiO_5 grains also coarsen to grain sizes on average of about 600nm after 250h of $\text{H}_2\text{O}(\text{g})$ exposure [12].

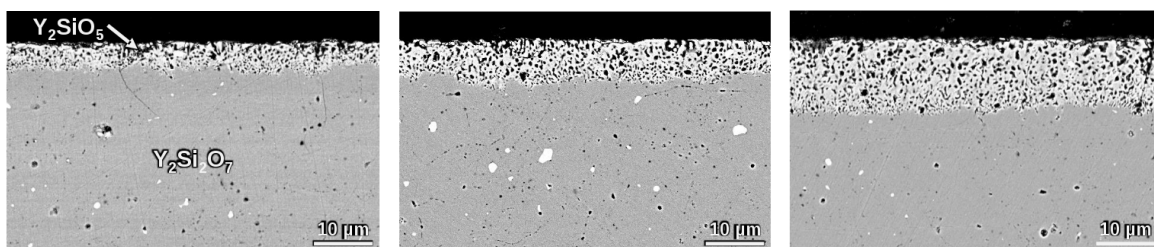


Figure 1.9: BSE images in cross-section of phase pure $\text{Y}_2\text{Si}_2\text{O}_7$ samples after 60, 125, and 250 hours at 1200°C in 1 atm of $\text{H}_2\text{O}(\text{g})$ with gas velocity of 158 - 174 m/s from left to right. Uniform SiO_2 depletion to form Y_2SiO_5 is observed. The layer thickness increases with time [12].

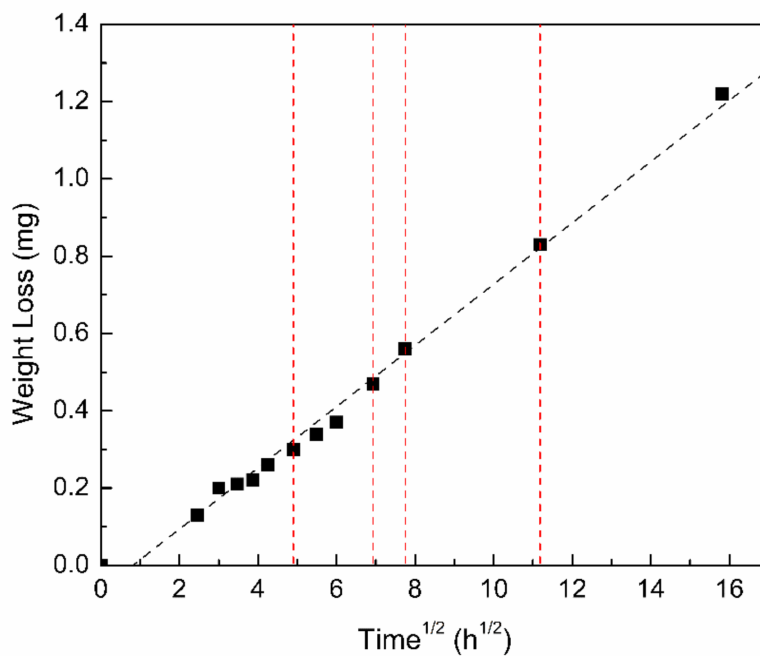


Figure 1.10: Weight loss vs. \sqrt{t} for a dense phase pure $\text{Y}_2\text{Si}_2\text{O}_7$ sample exposed over 250 hours with intermittent removal at 1200°C in 1 atm of $\text{H}_2\text{O}(\text{g})$ with gas velocity of 168 m/s shows excellent agreement with the parabolic rate law. The red lines represent when a new fused quartz capillary was inserted. Reproduced from Golden [12].

Courcot et al. have shown results that suggest the volatility of Y_2O_3 is greater than that of SiO_2 [38] [39]. This would be contradictory to the activity measurements made by Jacobson in the Y_2O_3 - SiO_2 system, which show a lower activity of Y_2O_3 compared to SiO_2 in the Y_2SiO_5 - $Y_2Si_2O_7$ phase field. This also contradicts the results explained above from Golden, show SiO_2 loss as the primary driver of chemical and microstructural change in this system under high-temperature, high-velocity water vapor.

1.4 Thermochemical Model of Phase and Microstructural Evolution

No prior model of reaction kinetics exists for the $RE_2Si_2O_7$ reaction in steam. One objective of this work is to develop such a model for lifetime prediction purposes. As was seen in the previous section, capturing the microstructural evolution is key to understanding and modeling the kinetics of the $RE_2Si_2O_7$ - $H_2O(g)$ system. The model developed in this work is based on that of Potts, incorporating solutions of Fick's Second law to capture vapor transport as described below. [40]

The Potts model was developed by Renfrey Potts as a variation on the Ising model of magnetization [41]. The model consists of "spins" on a regular lattice. These spins are arbitrary and can represent a multitude of things from phase to grain orientation. In this document "state" will be used rather than spin. The Potts model was initially developed to understand phase transitions but has been applied to Ostwald ripening, pore migration in metals, and sintering behavior [42]. The model is driven typically by Monte Carlo statistics to generate a random order of events. Potts modelling uses deterministic rules to drive behavior to simulate a sufficiently large number of outcomes that can be used for interpretation. The Potts model, along with the Monte Carlo event selection, are intended to model the microstructure and pore evolution specifically.

Previous Potts models have been combined with phase field modelling to accurately represent microstructure and composition evolution on the mesoscale [42]. However, it is also possible to accurately model the transport of $H_2O(g)$ and $Si(OH)_4(g)$ in the system using Fick's Second Law.

1.5 Overview of Dissertation Research Objectives and Results

The gaps in the current literature addressed with this research include: 1) How does the APS process changes the CTE behavior of phase pure materials; 2) Measurements of the anisotropy of $Y_2Si_2O_7$, Y_2SiO_5 , $Yb_2Si_2O_7$, and Yb_2SiO_5 at temperatures above 200°C; 3) The behavior of the Y_2O_3 and Y_2SiO_5 line compounds in high-temperature, high-velocity water vapor; 4) How, if at all, does the APS process change the thermochemical response of rare-earth silicates to high-temperature, high-velocity water vapor; 5) No model

currently exists for simulating the microstructural change over time experienced by rare-earth silicates in high-temperature, high-velocity water vapor.

Objective 1 addresses gaps 1 and 2. The differences in CTE between phase pure and APS materials is explored, showing an overall increase in CTE compared to phase pure materials due to the inclusion of higher CTE phases. The anisotropy of the crystal structures is also explored through high-temperature XRD, showing up to a five fold increase in CTE along certain directions of monoclinic structures when compared to others. This behavior corresponds to an increased density of RE cations along the directions of highest expansion. Coefficient of Thermal Expansion Analysis Suite (CTEAS) software [43] is used to help visualize the anisotropy of these crystals, and low expansion directions are found. These low expansion directions could be utilized in more controlled processing techniques to allow for thermal cycling without mechanical stresses being created between layers.

Objective 2 addresses gaps 3 and 4. The thermochemical stability of APS coatings in high-temperature, high-velocity steam probes the effect of low-SiO₂ content phases on the evolution of the porous RE₂SiO₅ layer that forms when RE₂Si₂O₇ reacts with H₂O(g). This work also confirms for the first time the reaction of Y₂SiO₅ with H₂O(g) to form Y₂O₃ at high gas velocities. The formation of Y₂O₃ from Y₂SiO₅ is accompanied by a densification of underlying Y₂SiO₅ which blocks Si(OH)₄(g) diffusion out of the system locally. The mechanism for this densification is not understood, but some hypotheses are given. The stability of Y₂O₃ in steam-jet conditions is also confirmed. Thermochemical stability of APS Yb₂Si₂O₇ coatings are tested in steam and show good agreement with phase-pure SPS Y₂Si₂O₇ samples. Increased crack and pore density causes local SiO₂ depletion to increase due to further infiltration of H₂O(g). Splat boundaries present from the APS process are shown to provide barriers to further SiO₂ depletion, increasing the diffusion distance for the reaction front to continue.

Objective 3 addresses gap 5. For the first time a computational model has been developed to accurately describe and predict the microstructural evolution of the RE₂Si₂O₇ system in the presence of high-temperature, high-velocity water vapor, including the moving reaction interface, porosity development, and product phase coarsening. A Potts model used to control the microstructural evolution of the system is combined with Fick's Second Law to control diffusion of Si(OH)₄(g) out of the system. This model was tied to physical length- and timescales through comparison with experimental results from steam-jet testing done at 1200°C for 60h. After 500 Monte Carlo steps the model matches well with observations with the sample exposed for 60h. The model can represent 120 hours of experimental testing in just over 9 hours using 128 processes. This means 10,000 hours of experimental exposure can be simulated in one month's worth of computational time using 128 processes.

Chapter 2

Thermal Expansion of Rare Earth Silicates

2.1 Objectives

There are three goals for this objective: measure CTE variations in APS processed RE silicates relative to phase pure material, measure the anisotropic thermal expansion of the monoclinic structures of the rare earth silicates, and to assess the accuracy of these measurements reported in the literature.

2.2 Experimental

2.2.1 Materials

Fused crushed powders of $Y_2Si_2O_7$, Y_2SiO_5 , $Yb_2Si_2O_7$, and Yb_2SiO_5 were obtained from Praxair (Praxair Surface Technologies, Indianapolis, IN) to create the samples for this objective. These powders were intended for air plasma spray (APS) and had sizes of 25 μm . These powders were prepared for dilatometry of APS $Y_2Si_2O_7$, SPS $Y_2Si_2O_7$ and Y_2SiO_5 , and lattice parameter measurement on $Y_2Si_2O_7$, Y_2SiO_5 , $Yb_2Si_2O_7$, and Yb_2SiO_5 as described below.

$Y_2Si_2O_7$ material was prepared using a Praxair SG-100 plasma spray gun (Praxair Surface Technologies, Indianapolis, IN) at the University of Virginia using the fused crushed powder described above. Samples were sprayed using 300 A torch current with 180 scfh Ar and 3 scfh H_2 flowing into the torch. Powder was sprayed on an aluminum substrate at room temperature with no additional cooling. Final thickness of the APS slabs was ~ 5 mm. Dilatometry bars were cut from the slabs with dimensions of 10mm x 5mm x 5mm. These

bars were then polished on all faces to 1200 grit SiC grinding paper to remove any contaminants from the aluminum spraying substrate and provide a smooth surface for contact in the dilatometer, described below.

$Y_2Si_2O_7$ and Y_2SiO_5 powders were processed using spark plasma sintering (SPS) to create dense phase pure testing materials to compare with the air plasma sprayed samples. The powders were ball milled for 24 hours using ZrO_2 milling media to reduce powders to submicron size before processing. Processed pucks had >95% theoretical densities and were cut into slabs with dimensions of 100mm x 5mm x 5mm like the APS material above and polished in the same way.

Powders of $Y_2Si_2O_7$, Y_2SiO_5 , $Yb_2Si_2O_7$, and Yb_2SiO_5 were laser melted in Evanston, IL at Materials Development, Inc. (MDI) in a water cooled copper hearth into beads of diameter ~ 2 mm for high temperature X-ray diffraction experiments at the Advanced Photon Source (here referred to as beamline) Beamline 6ID-D at Argonne National Laboratory as described below.

2.2.2 Characterization

A PANalytical X'Pert Pro diffractometer was used to perform XRD analysis on all SPS and APS Y_2SiO_5 and $Y_2Si_2O_7$ test bars used in the dilatometer, unannealed as well as annealed, before and after any physical measurements.

Change in specimen length was determined using a dilatometer (Netzsch DIL 402C) at temperatures of 20 – 1400°C heating and cooling at 3°C/min with 300ccm Ar flowing through the chamber and 25cN of force applied without any prior annealing. Two as-deposited APS $Y_2Si_2O_7$ bars, two APS $Y_2Si_2O_7$ bars annealed at 1200°C for 20 h, and a bar of SPS $Y_2Si_2O_7$ and Y_2SiO_5 were tested. The annealed samples were measured three times in succession.

A small block of unannealed APS $Y_2Si_2O_7$ material measuring ~ 5 mm on each side was characterized in a Netzsch STA 449 F1 Jupiter Thermogravimetric Analyzer (TGA)/Differential Scanning Calorimeter (DSC)/Differential Thermal Analyzer (DTA) at temperatures of 20 – 1200°C with heating and cooling rates of 10°C/min and a hold time at 1200°C of 20h with 60 mL/min Ar flowing through the chamber. The crystallization temperature was determined from DSC results.

ImageJ was used for analysis of micrographs of as-sprayed APS $Y_2Si_2O_7$ samples to give an estimate of phase content and microstructural features [44]. This was done using image contrast thresholding as each set of features corresponds to a different brightness in the micrographs.

High temperature XRD was performed on 2mm beads of Y_2SiO_5 , $Y_2Si_2O_7$, Yb_2SiO_5 , and $Yb_2Si_2O_7$ at the beamline. These beads were levitated by Ar using varying flow rates from 0 to 100 ccm and heated by a laser, with temperature control through a pyrometer software interface made in LabView provided

by MDI [45]. A schematic of this levitation apparatus is shown in Figure 2.1, with a photograph of the beamline system shown in Figure 2.2. XRD was performed using 100kV energy X-rays with a wavelength of 0.123984\AA . The detector was a 2D amorphous silica area detector (Perkin-Elmer XRD1621) [45]. XRD spectra were obtained every 100°C between 800 and 2000°C for all samples.

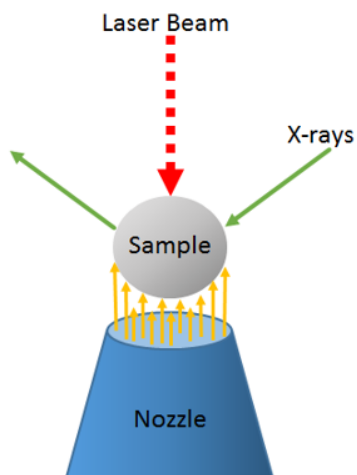


Figure 2.1: A schematic of the experimental setup for high temperature XRD of RE silicates on the beamline. Figure courtesy of Rachel Guarriello.

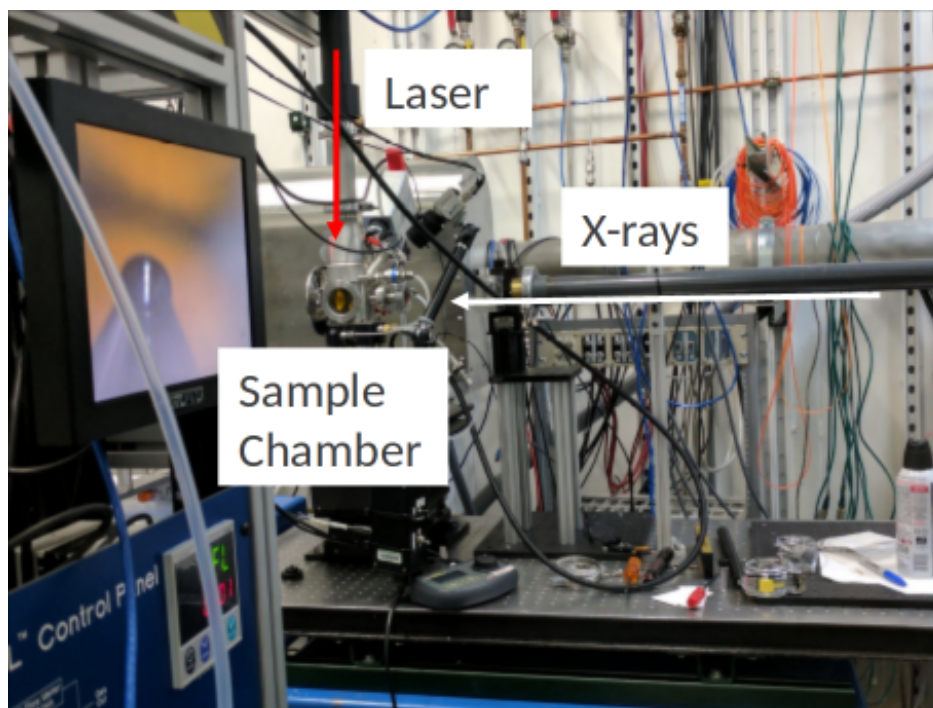


Figure 2.2: A photograph of beamline hutch 6ID-D at the Advanced Photon Source of Argonne National Laboratory.

Powder data was integrated and converted from raw images using Fit 2D, which allowed for polarization and geometric corrections [46]. Lattice parameters for a, b and c were determined, along with the angle β between directions a and b if the structure was monoclinic, at each temperature, including room temperature using GSAS-II [47]. Change in length of each parameter was calculated based on comparison to room temperature measurements. A program called Coefficient of Thermal Expansion Analysis Suite (CTEAS), developed by the Kriven group at the University of Illinois Urbana-Champaign [43], was used to visualize the thermal expansion of the crystals in 3D space and allow for determination of low expansion directions. CTEAS takes inputs at all measured temperatures of the crystal structure, lattice parameters measured at this temperature, and the d-spacing of approximately 10 planes for these materials. It then determines the crystal expansion or contraction in 3D space with changing temperature.

2.3 Results

2.3.1 XRD of APS $Y_2Si_2O_7$

As-received $Y_2Si_2O_7$ powder was completely β -phase (PDF 04-012-4410). The XRD analysis of the unannealed APS material showed some crystalline phases plus an amorphous structure. Samples analyzed after annealing at 1200°C for 20h showed the return of crystallinity. Y_2SiO_5 (PDF 00-036-1476), α (PDF 04-016-5897), and ζ (PDF 04-013-8417) polymorphs of $Y_2Si_2O_7$ appeared along with β - $Y_2Si_2O_7$. Figure 2.3 below shows the results of the XRD analysis normalized to the highest arbitrary intensity of each scan and stacked for as-received, as-sprayed, and post-anneal $Y_2Si_2O_7$ material.

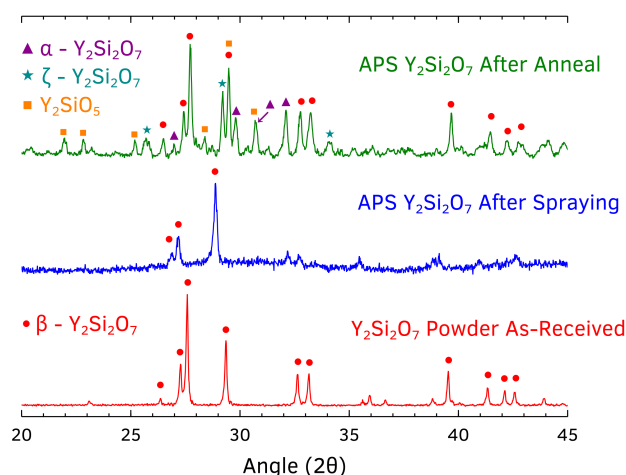


Figure 2.3: XRD patterns of as-received, as-sprayed, and post-anneal $Y_2Si_2O_7$ material. Note that the patterns for as-received and post-anneal are different. Y_2SiO_5 , α , and ζ $Y_2Si_2O_7$ appear after annealing at 1200°C for 20h.

2.3.2 SEM Phase Contrast Analysis of APS $Y_2Si_2O_7$

APS microstructures vary from sample to sample due to the APS process. Figure 2.4 shows a typical polished plan view SEM BSE image of an as-processed APS $Y_2Si_2O_7$ coating. There are at least four contrasting phases that can be observed in the image: 1. SiO_2 -poor regions 2. $RE_2Si_2O_7$ 3. phases with middling SiO_2 content 4. porosity. The SiO_2 content was explored using EDS. Other than $Y_2Si_2O_7$ no other EDS signals were consistent with the stoichiometry of any Y-Si-O phases. XRD showed the presence of Y_2SiO_5 as well as α , β , and ζ polymorphs of $Y_2Si_2O_7$.

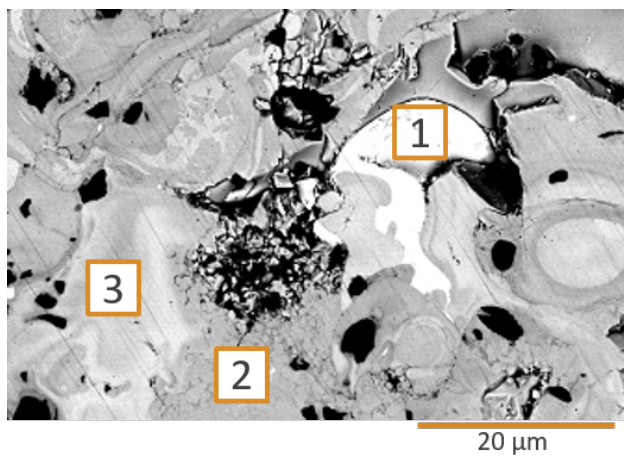


Figure 2.4: BSE plan view image of a typical as-processed $Y_2Si_2O_7$ APS microstructure with surface polish. Note the four phase features present: 1. SiO_2 -poor regions 2. $RE_2Si_2O_7$ 3. phases with middling SiO_2 content 4. porosity.

In addition to phase inhomogeneity, the microstructure of APS materials, has more defects than fully dense material prepared using spark plasma sintering (SPS). Figure 2.5 shows an SEM image of the cross section of an as-processed APS $Y_2Si_2O_7$ sample fabricated at UVA. Approximately 7% of the area of the image is cracks and pores in the sample as determined by ImageJ areal analysis. Figure 2.6 shows the contrast thresholding evaluation that was done on Figure 2.5 to estimate phase content including cracks and pores.

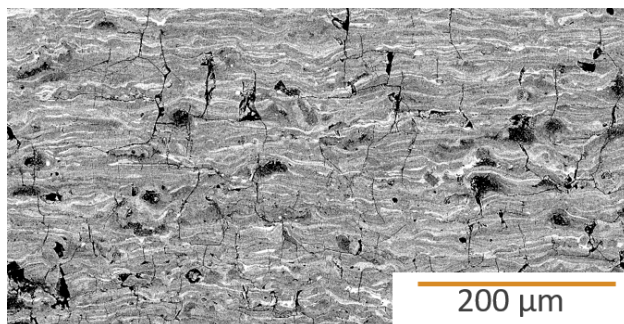


Figure 2.5: A BSE cross-sectional image of an as-processed APS $Y_2Si_2O_7$ sample. Large amounts of cracking and porosity, along with a variety of phases, are present.

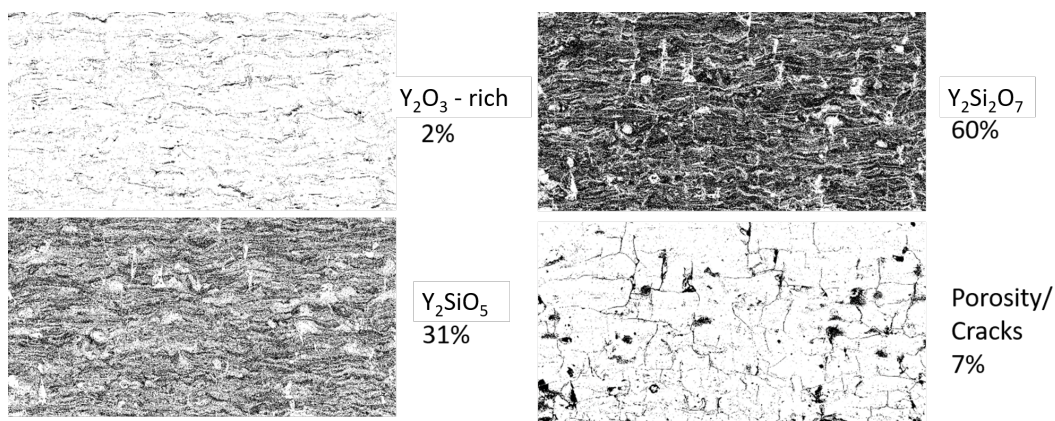


Figure 2.6: Contrast thresholding analysis of Figure 2.5 to estimate phase and defect content. Black in each figure represents the constituent being identified.

2.3.3 DSC and Dilatometry of APS $Y_2Si_2O_7$

DSC measurement of the unannealed $Y_2Si_2O_7$ coating material showed a large exothermic peak at 1050°C as seen in Figure 2.7. This peak was attributed to crystallization of the amorphous APS material. The unannealed $Y_2Si_2O_7$ sample dilatometry results showed a large dimensional change at $\sim 1050^\circ C$ as shown in Figure 2.8. This result was not observed on a second heating cycle and is associated with crystallization observed in the DSC presented in Figure 2.7.

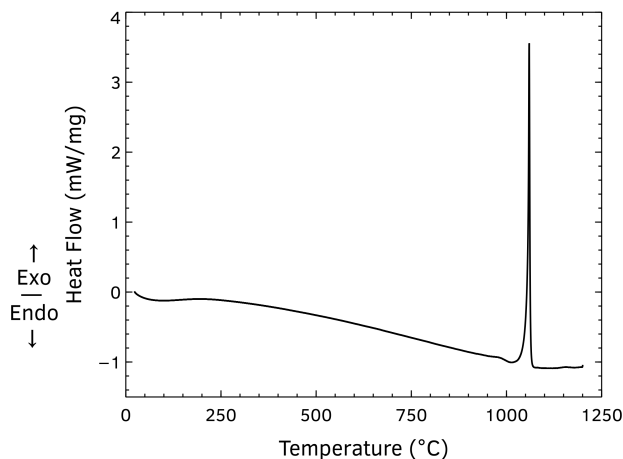


Figure 2.7: Heat flow vs. temperature for unannealed APS $Y_2Si_2O_7$ obtained by DSC. A crystallization peak was observed at $1050^\circ C$.

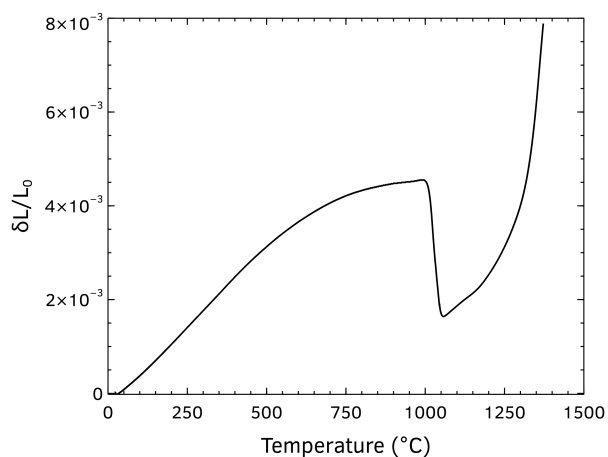


Figure 2.8: $\delta l/L_0$ vs. temperature for unannealed APS $Y_2Si_2O_7$. The sample reduces in length during crystallization at $1050^\circ C$.

The CTE measurements of the annealed APS $Y_2Si_2O_7$ material are shown below in Figure 2.9. The figure shows one APS sample dataset compared to phase pure $Y_2Si_2O_7$ and Y_2SiO_5 material prepared using SPS. The measured CTE of the phase pure SPS $Y_2Si_2O_7$ ($5.0 \cdot 10^{-6}$) and Y_2SiO_5 ($6.9 \cdot 10^{-6}$) at $1000^\circ C$ have reasonable agreement with the CTE values found in literature for these materials [23]. The measured CTE of the as-sprayed APS $Y_2Si_2O_7$ starts at $\sim 9 \cdot 10^{-6}$ 1/K at $1000^\circ C$ in its first heating cycle, then decreases to $\sim 5.5 \cdot 10^{-6}$ 1/K for the second and third cycles, again measured at $1000^\circ C$. However, the CTE is higher than the phase pure $Y_2Si_2O_7$, even after three cycles. The drop in CTE between first and subsequent dilatometry measurements was consistent across samples and independent of the annealing time applied to the samples. XRD patterns of the $Y_2Si_2O_7$ APS material after each processing or testing cycle are shown in Figure 2.10 with the relative intensity of peaks changing between annealing and dilatometry. Samples labelled as being

annealed twice were annealed once, removed from the furnace, then annealed again before any dilatometry or XRD. This XRD pattern is included here simply as a comparison to the XRD pattern for the original sample that had undergone dilatometry twice. No difference in the XRD pattern was found between the second and third dilatometry runs.

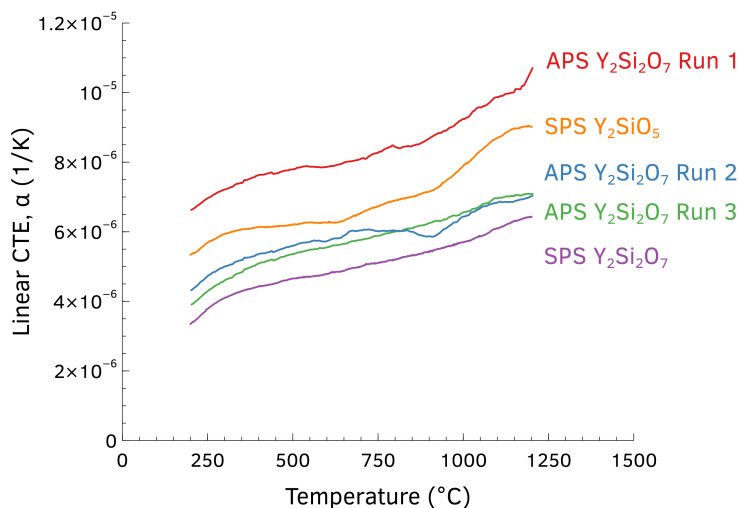


Figure 2.9: Dilatometry results of linear CTE vs. temperature for phase pure SPS $Y_2Si_2O_7$ and Y_2SiO_5 as well as three successive runs of one sample of APS $Y_2Si_2O_7$ that had been annealed at $1200^{\circ}C$ for 20h.

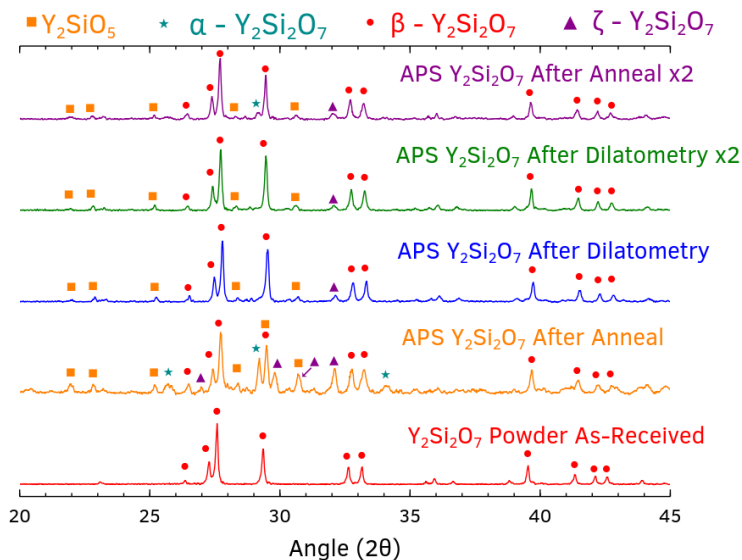


Figure 2.10: A comparison of the XRD results for $Y_2Si_2O_7$ APS material after each processing and testing step. The relative intensity of the two highest intensity peaks for $\beta - Y_2Si_2O_7$ change between annealing and the first dilatometry measurement. Polymorphs of $Y_2Si_2O_7$ such as α and δ are no longer measurable after a second annealing. Phase identification was done on peaks with an intensity $\geq 10\%$ of the maximum intensity.

2.3.4 High Temperature XRD of Y and Yb mono- and disilicates

The XRD results over the temperature range from 800-2000°C for each of the materials measured are shown in Figures 2.11 through 2.14. Figures 2.11, 2.12, and 2.14 show the same pattern through all temperatures with small shifts in peak position. The pattern for $Y_2Si_2O_7$, shown in Figure 2.13 shows two additional phase present from 1200°C to 1800°C. δ $Y_2Si_2O_7$ is present throughout the temperature range, but becomes less prominent at higher temperatures as the γ polymorph appears.

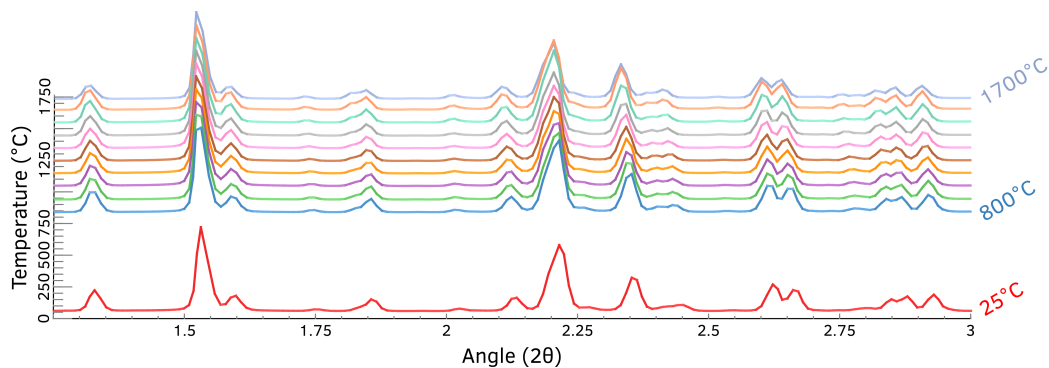


Figure 2.11: X-ray diffraction pattern of $Yb_2Si_2O_7$ measured at Argonne National Laboratory from room temperature to 1700°C.

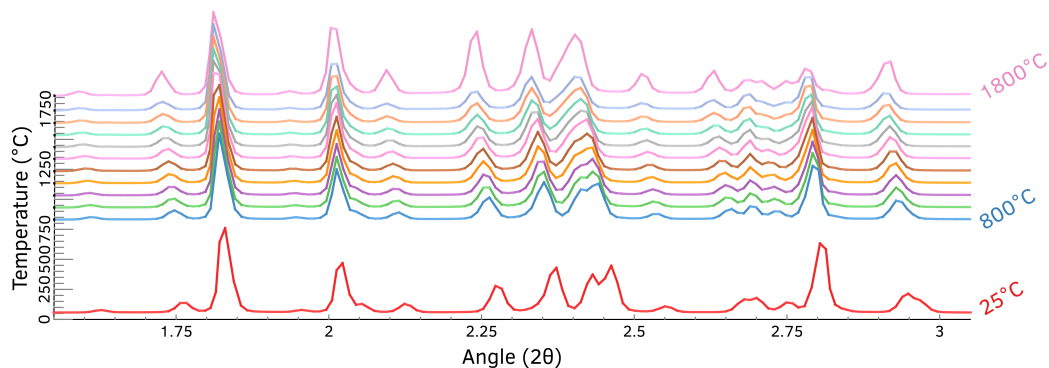


Figure 2.12: X-ray diffraction pattern of Yb_2SiO_5 measured at Argonne National Laboratory from room temperature to 1800°C.

The crystal structure of each of the phases measured for CTE change are shown in Figures 2.15 through 2.18. It should be noted that while $Yb_2Si_2O_7$, Yb_2SiO_5 , and Y_2SiO_5 showed monoclinic structures throughout the high-temperature measurements, $Y_2Si_2O_7$ showed the δ polymorph which is an orthorhombic structure throughout the temperature range, and monoclinic γ at higher temperatures.

Plots of the change in lattice parameter length, in addition to the β angle in monoclinic structures, vs temperature are shown in Figures 2.19 through 2.22. The CTE of each parameter is given in Table 2.1,

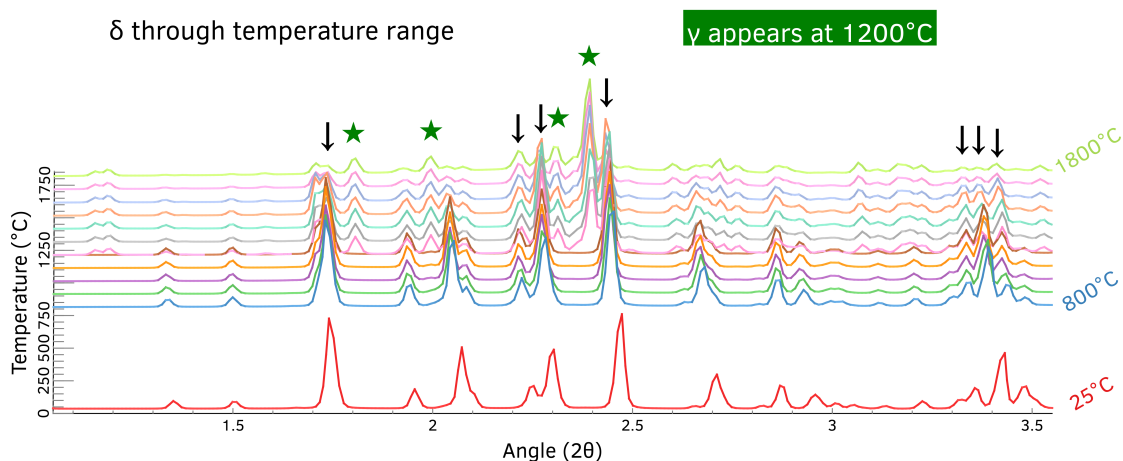


Figure 2.13: X-ray diffraction pattern of $Y_2Si_2O_7$ measured at Argonne National Laboratory from room temperature to 1800°C.

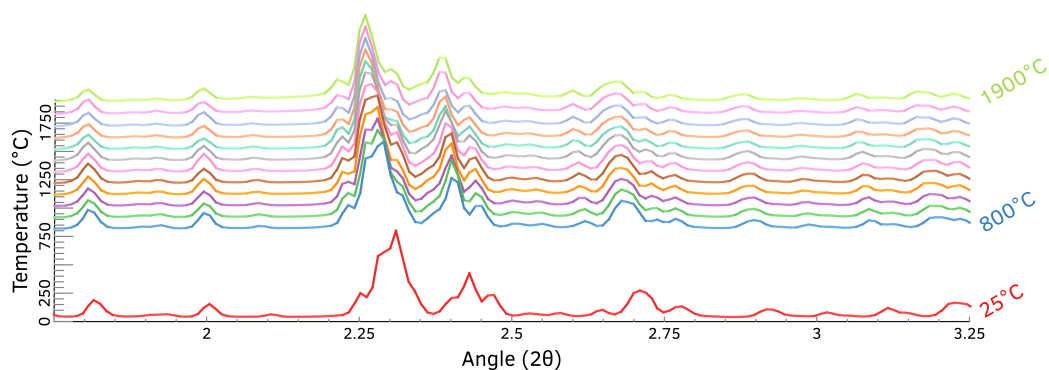


Figure 2.14: X-ray diffraction pattern of Y_2SiO_5 measured at Argonne National Laboratory from room temperature to 1900°C.

calculated from the slope of the linear best fit of the measured values presented in Figures 2.19 through 2.22.

Sources of scatter in the measurements will be discussed in Section 2.4.2.

Table 2.1: The CTE values calculated from the linear fit of the lattice parameter change values from 800-2000°C for each material.

Parameter	$Yb_2Si_2O_7$ CTE ($1/K \cdot 10^{-6}$)	Yb_2SiO_5 CTE ($1/K \cdot 10^{-6}$)	δ - $Y_2Si_2O_7$ CTE ($1/K \cdot 10^{-6}$)	X2- Y_2SiO_5 CTE ($1/K \cdot 10^{-6}$)
Volume	15.4	32.1	19.2	16.9
a	7.80	3.89	5.31	7.25
b	5.04	12.4	8.26	1.72
c	2.88	10.8	5.30	11.5
β	1.15	-3.66	-	5.60

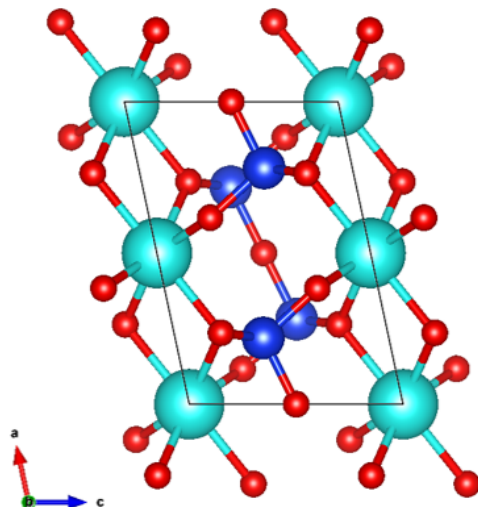


Figure 2.15: The monoclinic crystal structure of $\text{Yb}_2\text{Si}_2\text{O}_7$, matched to high-temperature XRD patterns. The teal atoms are Yb, blue atoms are Si, and the red atoms are O.

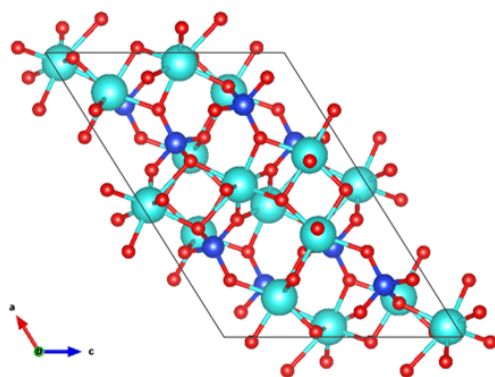


Figure 2.16: The monoclinic crystal structure of Yb_2SiO_5 , matched to high-temperature XRD patterns. The teal atoms are Yb, blue atoms are Si, and the red atoms are O.

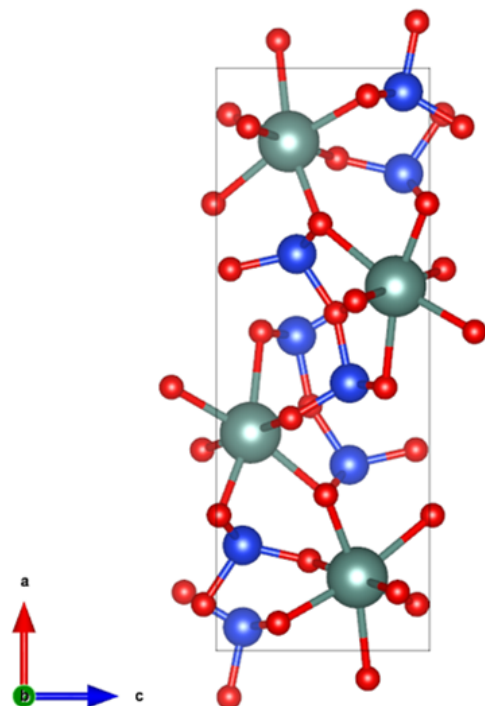


Figure 2.17: The orthorhombic δ polymorph of $Y_2Si_2O_7$, matched to high-temperature XRD patterns. The green atoms are Y, the blue atoms are Si, and the red atoms are O.

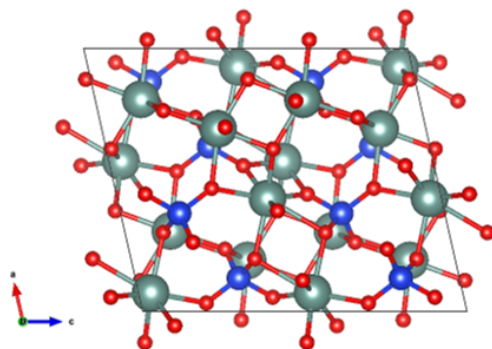


Figure 2.18: The monoclinic X2 polymorph of Y_2SiO_5 , matched to high-temperature XRD patterns. The green atoms are Y, the blue atoms are Si, and the red atoms are O.

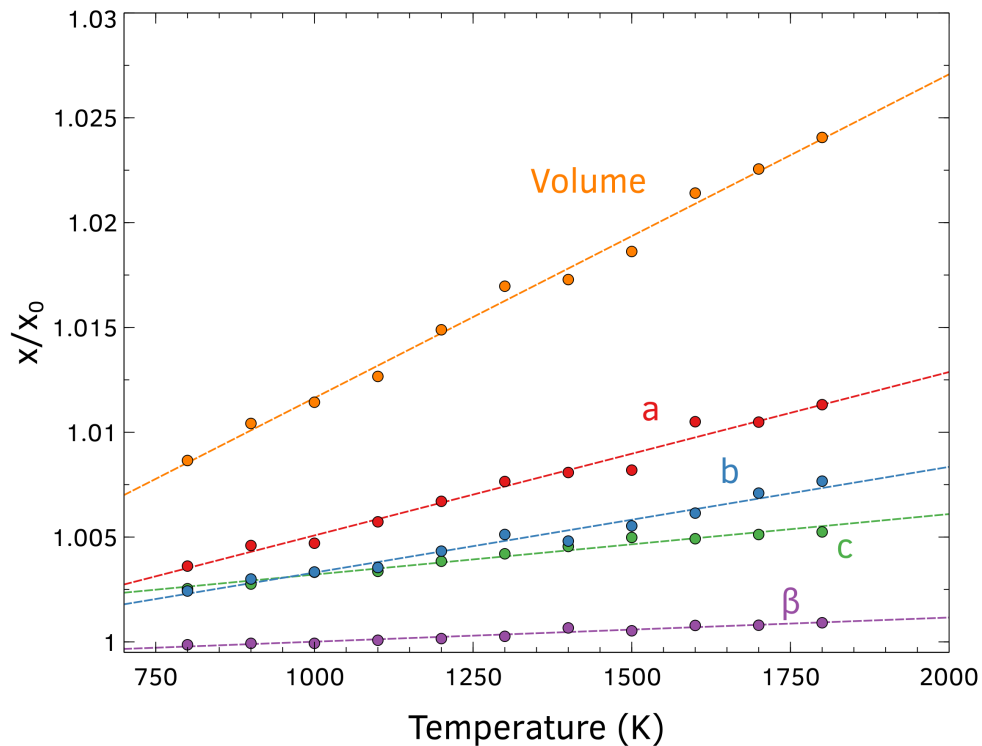


Figure 2.19: The x_T/x_0 values of a, b, c, β , and volume parameters of the $\text{Yb}_2\text{Si}_2\text{O}_7$ crystal measured vs temperature. Each parameter value is normalized with respect to that parameter value at room temperature.

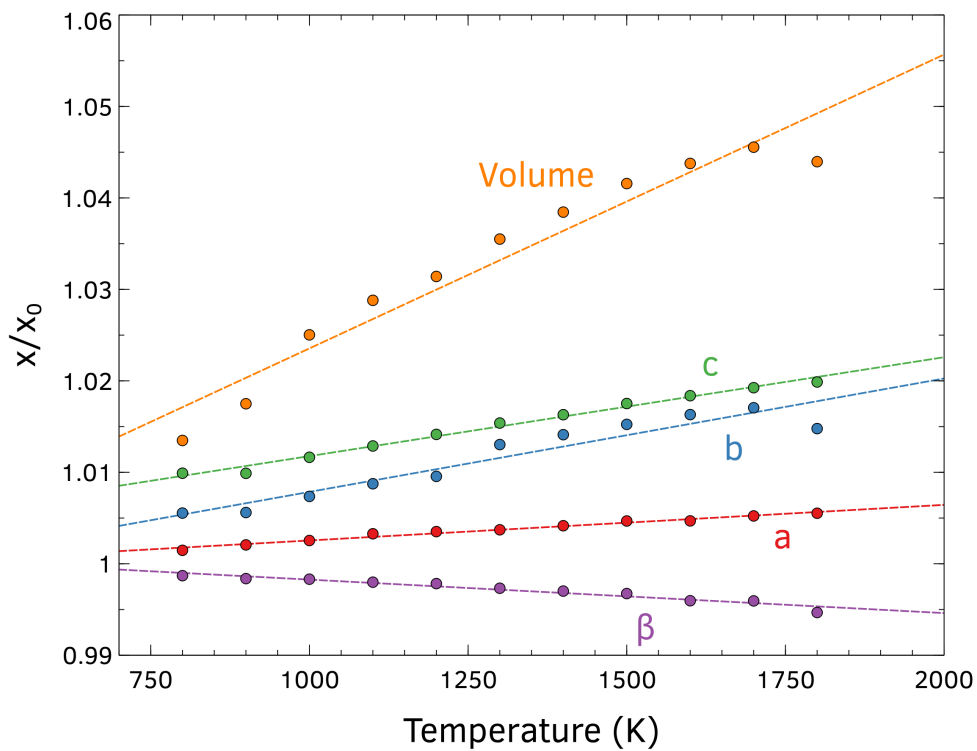


Figure 2.20: The x_T/x_0 values of a, b, c, β , and volume parameters of the Yb_2SiO_5 crystal measured vs temperature. Each parameter value is normalized with respect to that parameter value at room temperature.

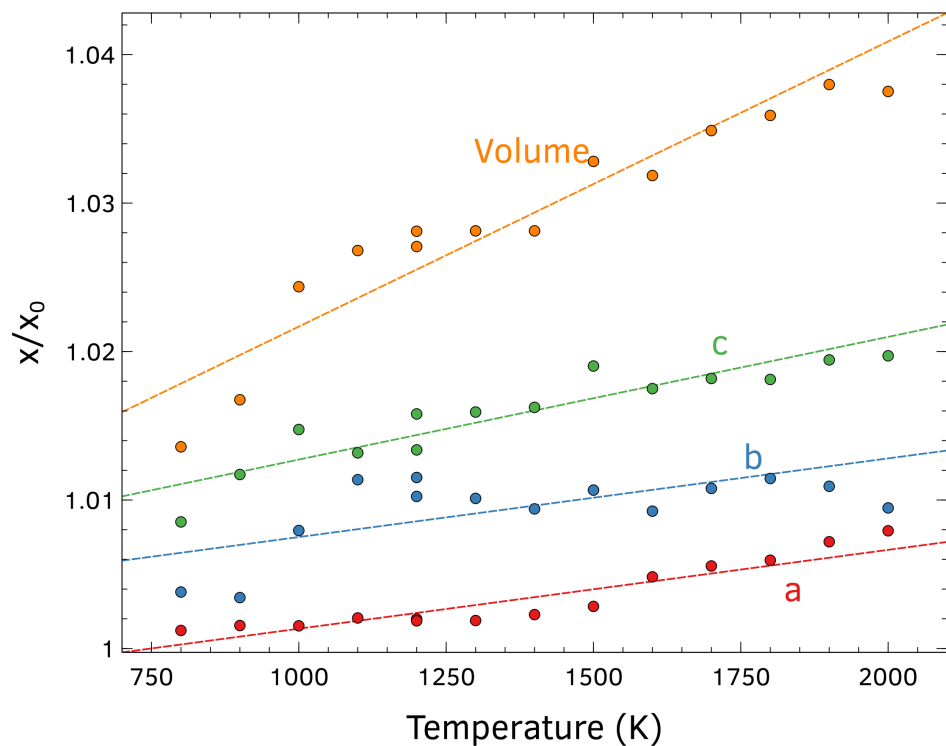


Figure 2.21: The x_T/x_0 values of a, b, c, and volume parameters of the δ $Y_2Si_2O_7$ crystal measured vs temperature. Each parameter value is normalized with respect to that parameter value at room temperature.

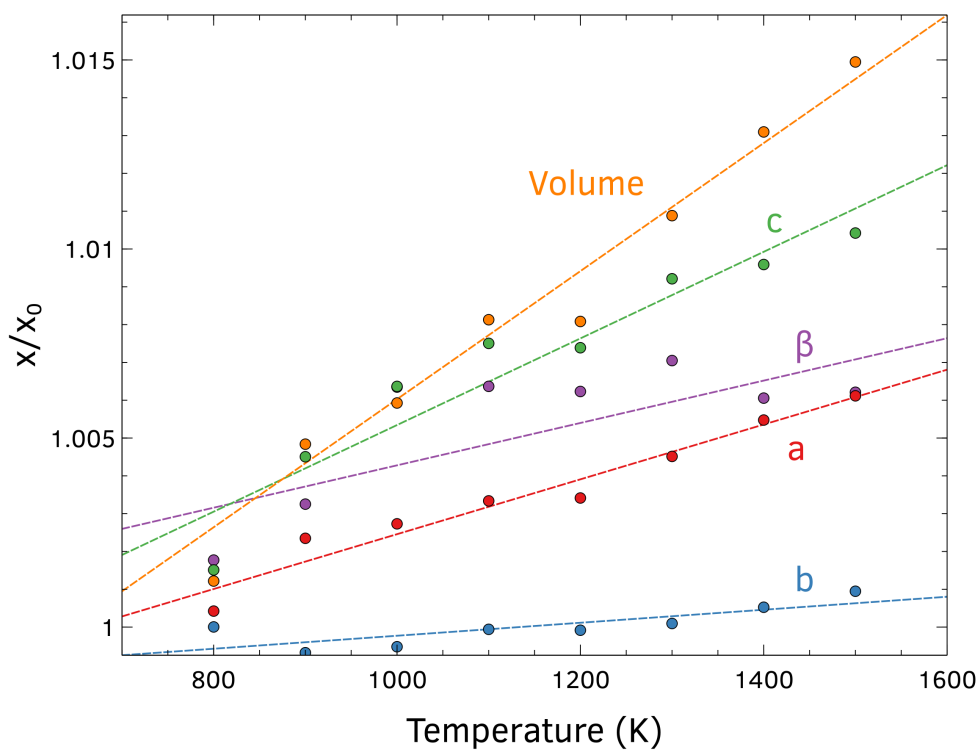


Figure 2.22: The x_T/x_0 values of a, b, c, β , and volume parameters of the $X_2 Y_2SiO_5$ crystal measured vs temperature. Each parameter value is normalized with respect to that parameter value at room temperature.

The lattice parameter change with temperature, along with the change in d-spacings for 13-23 crystal planes, depending on the sample and quality of the scans, were used for inputs to calculate thermal expansion in three dimensions. 3D plots of thermal expansion at 1500°C are presented below for each of $\text{Yb}_2\text{Si}_2\text{O}_7$, Yb_2SiO_5 , $\text{Y}_2\text{Si}_2\text{O}_7$, and Y_2SiO_5 in Figures 2.23 through 2.26. It is important to note that because monoclinic structures do not have all three axes orthogonal to one another, the Z axes in these representations are not parallel to the c direction of the crystal. CTE values of below 2 can be seen in the Y_2SiO_5 plots, with less pronounced differences in expansion with respect to direction occurring with the other structures.

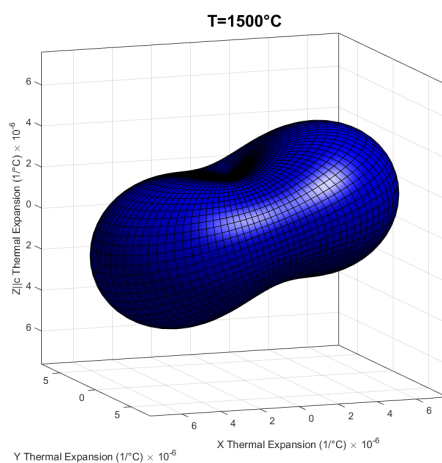


Figure 2.23: CTE ellipsoid output from CTEAS software for $\beta\text{-Yb}_2\text{Si}_2\text{O}_7$ at 1500°C. As this is a monoclinic structure the Z axis is parallel to the c crystallographic direction in the structure, while the X and Y axes are not parallel to the a and b directions.

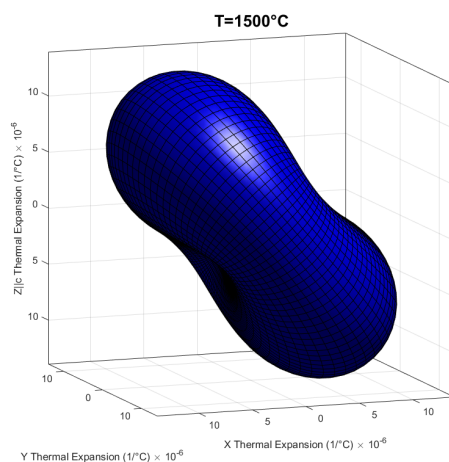


Figure 2.24: CTE ellipsoid output from CTEAS software for $\text{X}_2\text{-Yb}_2\text{SiO}_5$ at 1500°C. As this is a monoclinic structure the Z axis is parallel to the c crystallographic direction in the structure, while the X and Y axes are not parallel to the a and b directions.

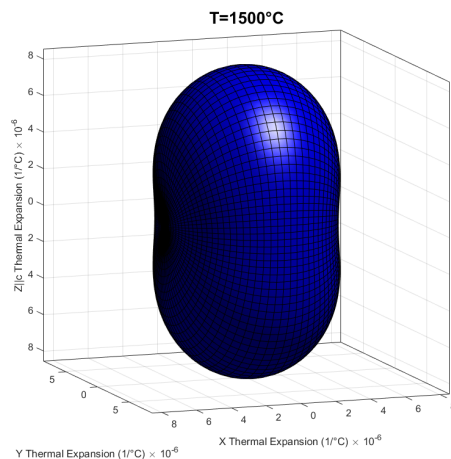


Figure 2.25: CTE ellipsoid output from CTEAS software for δ - $\text{Y}_2\text{Si}_2\text{O}_7$ at 1500°C . The δ polymorph is orthorhombic, and so all three axes are parallel to the three crystallographic directions.

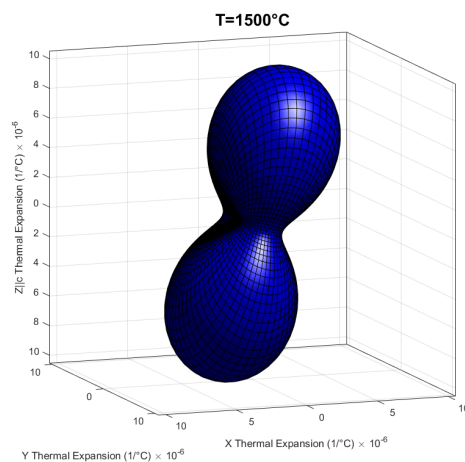


Figure 2.26: CTE ellipsoid output from CTEAS software for $\text{X}_2\text{-Y}_2\text{SiO}_5$ at 1500°C . As this is a monoclinic structure the Z axis is parallel to the c crystallographic direction in the structure, while the X and Y axes are not parallel to the a and b directions.

2.4 Discussion

2.4.1 APS $\text{Y}_2\text{Si}_2\text{O}_7$

XRD results from Figure 2.3 show that after annealing for 20 h at 1200°C the APS material presented a pattern different from the as-received $\text{Y}_2\text{Si}_2\text{O}_7$ powder. Annealing restored crystallinity to the material, but new polymorphs of $\text{Y}_2\text{Si}_2\text{O}_7$ α and ζ , and Y_2SiO_5 appeared due to the APS process.

This XRD analysis is consistent with the image analysis in Figure 2.6 that shows a range of phase contrasts in a BSE SEM image. This phase contrast shows phases that are brighter than the original $\text{Y}_2\text{Si}_2\text{O}_7$ powder. This means that the Z-number of the phases is higher, suggesting that SiO_2 has been lost during the spray

process, which occurs at temperatures up to 20000 K in the argon plasma. The loss of SiO_2 is more likely than the loss of Y_2O_3 due to the lower melting temperature of SiO_2 , 1723°C for SiO_2 compared to 2425°C for Y_2O_3 .

The dilatometry results of the APS $\text{Y}_2\text{Si}_2\text{O}_7$ material show that the CTE is consistently higher than the phase pure SPS material. This is attributed to the presence of the Y_2O_3 -rich phases in the microstructure. As seen in Figure 2.9, the measured CTE of phase pure Y_2SiO_5 is $6.9 \cdot 10^{-6}$ 1/K, and the reported CTE of Y_2O_3 is $8.5 \cdot 10^{-6}$ 1/K at 1000°C [48]. While Y_2SiO_5 is the only of these two that is confirmed through XRD to be present in the structure, trace amounts of Y_2O_3 consistent with the phase contrast could be present, driving up the bulk CTE.

The large drop in CTE between the initial cycle and subsequent cycles is a change in the polymorphs of $\text{Y}_2\text{Si}_2\text{O}_7$ present in the sample. Figure 2.10 shows the relative intensity of the XRD peaks in each pattern changing with dilatometry measurements. The reported CTE of several common polymorphs of $\text{Y}_2\text{Si}_2\text{O}_7$ are quite a different ($\alpha = 8.0 \cdot 10^{-6}$, $\beta = 4.1 \cdot 10^{-6}$, $\gamma = 3.9 \cdot 10^{-6}$, $\delta = 8.1 \cdot 10^{-6}$ 1/K, ζ unreported) [23]. The as-received powder is pure β - $\text{Y}_2\text{Si}_2\text{O}_7$, starting with the lower $4.1 \cdot 10^{-6}$ 1/K CTE. After spraying α - and δ - $\text{Y}_2\text{Si}_2\text{O}_7$ appear in the XRD scan along with the X2 polymorph of Y_2SiO_5 . After dilatometry is carried out only α -, β -, and ζ - $\text{Y}_2\text{Si}_2\text{O}_7$ remain along with the X2 Y_2SiO_5 . The relative phase content of the α - and ζ - $\text{Y}_2\text{Si}_2\text{O}_7$ continues to reduce with subsequent anneals or dilatometry measurements. This reduction in high CTE phases relative to the low CTE β polymorph correlates well with the lowering of the measured CTE with successive anneals or dilatometry measurements.

These variations in CTE between annealing and measurement exposures show that thermal cycling affects phases present in APS materials. Because EBCs are often cold sprayed onto SiC/SiC CMCs and then thermally cycled thereafter, the CTE of the complex phase and polymorph assemblage of APS material will change over time and potentially impact coating life. Coatings of $\text{Yb}_2\text{Si}_2\text{O}_7$ sprayed onto monolithic SiC received from Rolls-Royce corporation show a mostly amorphous structure before any testing. While $\text{Yb}_2\text{Si}_2\text{O}_7$ coatings would not experience the equilibration of polymorphs seen in the $\text{Y}_2\text{Si}_2\text{O}_7$ coatings presented here, the crystallization is likely to stress the coating, and the presence of Yb_2O_3 -rich phases will drive up the CTE of the coating compared to expected values.

2.4.2 High Temperature XRD of Y and Yb mono- and disilicates

The levitation laser system used for measurement in this case requires special consideration for interpretation of the results. While the ideal scenario of the levitation system is to have the specimen bead slowly spinning at a constant speed and height, this is not always accomplished. The X-ray beam is calibrated be-

fore heating and measurements begin to ensure that at least 30 μm of the specimen bead is being sampled. However, if the bead sticks to the nozzle then the bead drops in height, reducing the amount of material being sampled by XRD. The bead sticking to the nozzle also prevents smooth rotation of the bead. This causes a limited amount of grains to be sampled during a given scan. While gas velocity and nozzle spin are used to provide uniform rotation during every scan, occasionally ideal measurements are not achieved.

A second consideration for this system, is the possibility of uneven heating of the laser. Temperature is measured by a pyrometer that sights on a specific area through which the X-rays are incident. However, the shape of a bead may not be completely spherical, and so temperature readings jump by several tens of degrees as the bead rotates. This is especially true at lower temperatures when the power of the laser is not enough to heat more than a small area of the bead. The laser power is directly controlled to provide an average temperature of $\pm 10^\circ\text{C}$ during a scan. However, the area being sampled by the X-rays is not necessarily the same as the area read from the pyrometer.

These two factors combined make it difficult to provide an exact temperature for a given scan. The average temperature error is on the order of 50°C . These factors can also explain why some parameter measurements shown in Figures 2.19 through 2.22 are lower at higher stated temperatures. Analysis of a lower temperature area can result in apparent fluctuations in lattice parameter from the assumed linear relationship.

The presence of the δ phase of $\text{Y}_2\text{Si}_2\text{O}_7$ through the entire temperature range is unexpected. The mass of the beads required for these tests is small, on the order of a few grams, resulting in rapid cooling during processing to retain the bead shape. δ is the highest temperature polymorph of $\text{Y}_2\text{Si}_2\text{O}_7$, and so is the most likely to crystallize from the melt upon rapid cooling. It is likely that δ formed upon cooling of these beads during fabrication and the times at temperature were not long enough to form the equilibrium polymorphs at each temperature. The equilibrium polymorphs are α below about 1200°C , β between 1200 and 1400°C , and γ stable up to 1600°C . Each temperature was measured for approximately 5 minutes. The bead therefore was held in the temperature range for α for approximately 20 minutes, β for 10 minutes, γ for 10 minutes, and the δ temperature range for another 20 minutes. These times were not long enough for equilibration [15]. As seen in the results for APS $\text{Y}_2\text{Si}_2\text{O}_7$ annealing at 1200°C , β is the equilibrium polymorph, however the α and δ polymorphs were still observed after 20 hours of annealing. It should be noted that a small amount of β phase did begin to appear in beamline XRD scans above 1200°C , however, not enough XRD peaks were present to make a CTE measurement.

A comparison between the measured CTE of each primary crystallographic direction of the Y_2SiO_5 unit cell from this study and those of O'Bryan and Fukuda is shown in Table 2.2 [27] [28]. The anisotropy of this crystal has been studied multiple times before, with reasonable agreement between the previous studies. The

data from this study for Y_2SiO_5 agree with these previous measurements. This agreement provides confidence to the anisotropy results for all four phases presented in this work. As such, the anisotropy measurements for β - $Yb_2Si_2O_7$ and $X2$ - Yb_2SiO_5 are the first of their kind. The measurements for $X2$ - Y_2SiO_5 and δ - $Y_2Si_2O_7$ are the first to show anisotropy measurements above $1400^\circ C$ [24].

Table 2.2: Comparison of the CTE values for each principal crystallographic direction in the $X2$ - Y_2SiO_5 monoclinic cell between the current study and those done by O’Bryan and Fukuda [27] [28].

Parameter	This Work CTE ($1/K \cdot 10^{-6}$)	O’Bryan (300°C) [27] CTE ($1/K \cdot 10^{-6}$)	Fukuda (1000°C) [28] CTE ($1/K \cdot 10^{-6}$)
a	7.25	7.43	8.10
b	1.72	1.1	1.65
c	11.5	9.5	12.2

The CTE measured for each direction of the structures show varying degrees of anisotropy. The monosilicates had the highest amount of anisotropy. Yb_2SiO_5 exhibited much lower expansion along the a direction ($3.89 \cdot 10^{-6}$ 1/K) than either b ($12.4 \cdot 10^{-6}$ 1/K) or c ($10.8 \cdot 10^{-6}$ 1/K), for a ratio of largest expansion coefficient to smallest of 3.2. $X2$ - Y_2SiO_5 showed much less expansion along the b direction ($1.72 \cdot 10^{-6}$ 1/K) than a ($7.25 \cdot 10^{-6}$ 1/K) or c ($11.5 \cdot 10^{-6}$ 1/K), for a ratio of largest to smallest expansion coefficient of 6.7. In comparison, $Yb_2Si_2O_7$ had an anisotropy ratio of 2.7, and $Y_2Si_2O_7$ of 1.6. The lower anisotropy ratio is expected for $Y_2Si_2O_7$ due to the orthorhombic structure measured in this work. The large differences between expansion coefficients along different directions of each crystal can be directly tied to the density of the rare earth atoms along each lattice parameter, with high expansion directions being related with high density of rare earth atoms. This makes sense, as the SiO_4 tetrahedra are less likely to increase in bond length with increasing temperature relative to rare earth cation-oxygen bonds. The $Yb_2Si_2O_7$ monoclinic structure follows this same pattern, with less overall expansion and anisotropy. The orthorhombic δ structure of $Y_2Si_2O_7$ showed relatively low anisotropy overall. It should be noted that the β angle for the Yb_2SiO_5 structure decreased towards 90° as compared to $Yb_2Si_2O_7$ or $X2$ Y_2SiO_5 , which saw increasing values of β . The β angle is larger in the Yb_2SiO_5 structure to begin with compared to the $Yb_2Si_2O_7$ or Y_2SiO_5 structures.

These anisotropy results show clearly in the 3D representations created in CTEAS. The low expansion direction measured in both Yb_2SiO_5 , and Y_2SiO_5 are visualized in Figures 2.24 and 2.26. The representations here show extremely low CTE directions in the crystal structures. These large differences in expansion in each direction can easily lead to stresses and cracking in APS coatings, especially if a crystallographic texture arises from the spraying. If the orientation of RE silicate crystals can be controlled during processing the thermal expansion could be tailored for specific applications.

2.5 Conclusions

The APS process is widely used for EBC materials because thick ($\sim 150\mu\text{m}$), dense ceramic coatings can be obtained in reasonable times. However, as shown with XRD, SEM, dilatometry, and DSC, the APS process changes material properties, crystallinity, and phase content due to the non-equilibrium nature of the process. The amorphous state of the as-sprayed material can be alleviated with short anneals at temperatures greater than the measured crystallization temperature of 1050°C . However, the chemical phase mixture that results from the SiO_2 loss during spraying cannot be substantially changed. The increased CTE relative to phase pure material results in a CTE mismatch with the underlying substrate and may shorten EBC life during thermal cycling. It is also probable that the variation in CTE between splats will cause cracking and damage that will allow for fast pathways of oxidant diffusion through the coating to the underlying bondcoat or substrate.

The high anisotropy measured in the monosilicates make them especially difficult to process, as texture and cooling are important considerations. Even the $\text{Yb}_2\text{Si}_2\text{O}_7$ structure shows anisotropy that must be accounted for. While the anisotropy of monoclinic polymorphs of $\text{Y}_2\text{Si}_2\text{O}_7$ were not measured with high-temperature XRD, similar anisotropy to $\text{Yb}_2\text{Si}_2\text{O}_7$ is expected. The multiple polymorphs of $\text{Y}_2\text{Si}_2\text{O}_7$ is an important consideration in the coating life of yttrium-bearing coatings. As was shown in the $\text{Y}_2\text{Si}_2\text{O}_7$ coatings sprayed at UVA, the polymorph content can change during high temperature exposure, causing an evolution in the CTE value of the coating.

It is interesting to note, however, that the extremely low CTE directions of the rare earth silicates, the monosilicates in particular, make tailoring the CTE possible. This could be achieved in coating methods that are more controllable than APS, such as thin film processing techniques.

2.6 Recommendations for Future Work

A major question that remains in this research is studying the thermomechanical response of anisotropic rare earth silicates. This could be achieved through thermal cycling studies following crack movement and phase distribution with cycles and time. The effect of splat size and initial crack and pore structure on how new cracks and phase content progresses would also be an interesting study.

Comparing the results of APS processed coatings to those deposited via other synthesis techniques is also important. Direct vapor deposition is being explored as a way to deposit dense, crack free coatings with deposition speeds lower than those of APS. Understanding how the thermal expansion of the phases deposited is affected by this processing technique is valuable for future engineering decisions.

Chapter 3

Thermochemical Stability of Phase Pure and Air Plasma Sprayed Rare Earth Silicates in High-Temperature, High-Velocity Water Vapor

3.1 Objectives

Current understanding on the thermochemical stability of rare earth silicate coatings is limited in a few ways. First, all work on high-temperature, high-velocity pure water vapor interactions with constituents of the $Y_2O_3 - SiO_2$ are at or below $1200^\circ C$ due to previous experimental limitations. Secondly, most testing has been done on phase pure $RE_2Si_2O_7$, rather than on Air Plasma Spray (APS) coatings, limiting the understanding of the APS process on the thermochemical response to water vapor. There is also no understanding of the temperature dependence of the reaction between $RE_2Si_2O_7$ and $H_2O(g)$ at temperatures above $1200^\circ C$. Lastly, there has been controversy over the stability of Y_2O_3 in the presence of high-temperature, high-velocity water vapor.

With these knowledge gaps in mind, the objectives of this chapter are to: 1) settle a controversy in the literature about the stability of Y_2O_3 in high-temperature $H_2O(g)$; 2) determine the behavior of phase pure $Y_2Si_2O_7$ in high-temperature, high-velocity water vapor as a function of increasing temperature; and 3)

compare the stability of air plasma sprayed (APS) rare earth disilicate coatings exposed in high-temperature, high-velocity water vapor to the stability of the phase pure materials tested in objective 2.

3.2 Experimental

3.2.1 Material

Amorphous SiO_2 samples (GE124 Quartz, 99.99% pure, Ted Pella Inc., Redding, CA) were cut to sizes of approximately 12.5 mm x 12.5 mm x 1 mm. SiO_2 coupons were cleaned in a sonicator using ethanol and deionized water for 15 minutes each prior to testing.

$\text{Y}_2\text{Si}_2\text{O}_7$ and Y_2SiO_5 samples were processed using spark plasma sintering (SPS) of powders (Praxair Surface Technologies, Indianapolis, IN) intended for air plasma spray (APS) with average particle size of $25\mu\text{m}$. The particles were ball milled for 24 hours using ZrO_2 milling media to reduce powders to submicron size before SPS processing. Processed pucks of $\text{Y}_2\text{Si}_2\text{O}_7$ and Y_2SiO_5 with $>95\%$ theoretical densities were cut into 10 mm x 10 mm x 1.5 mm samples. All samples prepared by SPS were exposed in a stagnant air box furnace at 1300°C for 48 hours to restore oxygen stoichiometry. Y_2O_3 specimens of 2.54 cm diameter, (99.9% pure, MaTeck, Jülich, Germany), $\text{Y}_2\text{Si}_2\text{O}_7$, and Y_2SiO_5 coupons were polished to 1200 grit SiC paper to provide a flat surface. After polishing, one sample of Y_2O_3 was exposed in a stagnant air box furnace at 1400°C for 24 h to provide microstructural comparison to the specimen tested in high-temperature, high-velocity water vapor.

APS coatings of $\text{Yb}_2\text{Si}_2\text{O}_7$ were supplied by Rolls-Royce Corporation. All coatings (note that these are ytterbium silicates, as opposed to the yttrium silicates described above) were sprayed onto monolithic SiC with no bond coat. Two types of coatings were provided, dense coatings processed with the aim of limited cracks or pores, and a porous coating meant to be abradable. The abradable coating required a bake-out at 500°C for 6h to remove a polymer sprayed with the coating to create the porosity. Neither coating type underwent any further heat treatment before steam-jet testing.

3.2.2 Steam-jet Furnace

All samples were exposed in high-temperature, high-velocity water vapor using the steam-jet furnace shown in Figure 3.1 which is a modified version of the steam-jets described by Lucato, Sudre, and Marshall [49] as well as Golden and Opila [29]. The modified steam-jet consists of a horizontal tube furnace (Model 1730-12HTF, CM Furnaces, Inc., Bloomfield, NJ) with a 3.5 cm inner diameter alumina tube (99.8% pure; McDanel Advance Ceramic Technologies, Beaver Falls, PA) and an inlet stainless steel endcap (MDC Vacuum

Products LLC, Hayward, CA) that accommodates feed through for liquid water and gas. A heater (Fibercraft Heater Model VF-360-2-12-V, Thermcraft Inc., Winston Salem, NC) of total length 34.3 cm and inner diameter of 5.1 cm with an insulating vestibule on the inlet side of the furnace tube of length 3.8 cm and inner diameter of 4.3 cm was added to the steam-jet apparatus [29] to pre-heat the liquid water being pumped into the furnace.

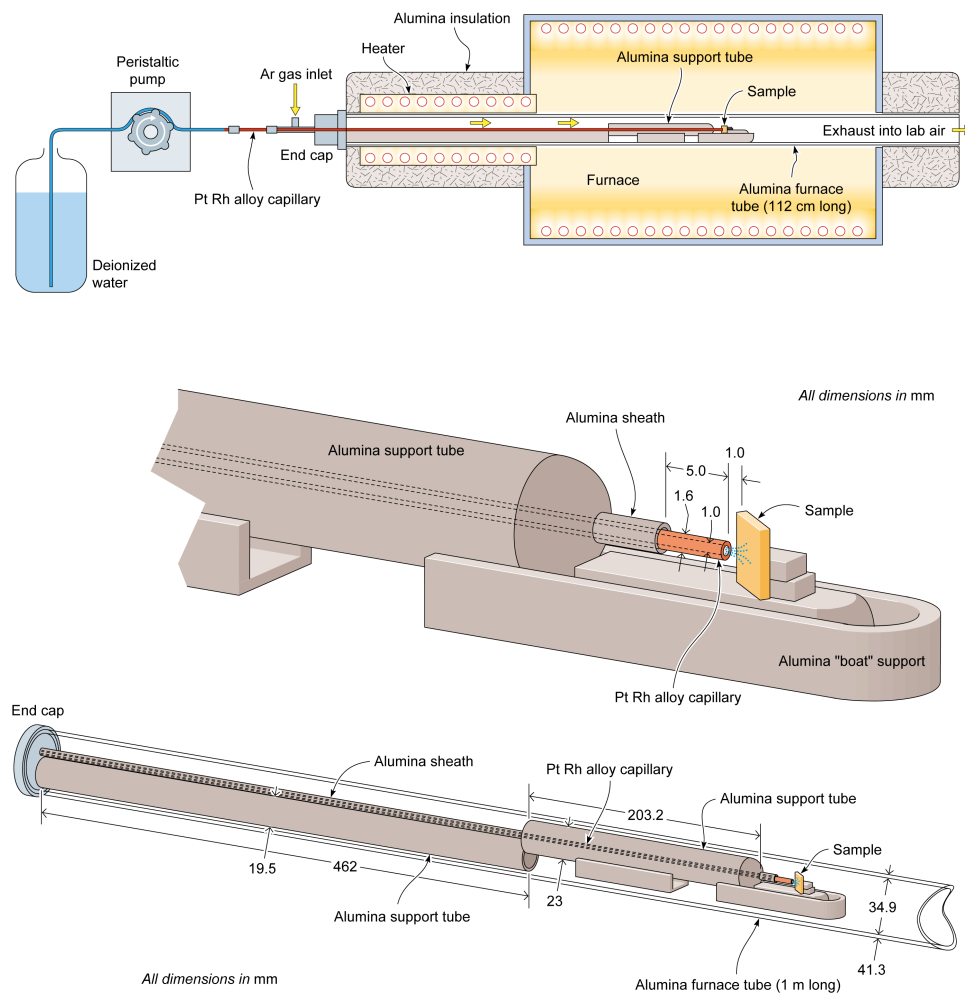


Figure 3.1: A schematic drawing of the steam-jet furnace (top) and details of the sample holder.

A peristaltic pump was used to feed deionized water into a 1.3 mm ID stainless steel tube. This steel tube was connected to a 1 mm ID 90% platinum, 10% rhodium (PtRh) capillary (Goodfellow Corporation, Coraopolis, PA). The PtRh capillary was supported by a sheath of alumina that ended 5 mm short of the

end of the PtRh capillary. Argon gas flowed into the tube furnace from the inlet side endcap at 200 ccm to limit the formation of $\text{PtO}_2(\text{g})$ from the outside of the capillary.

The flow rate of the liquid water was monitored throughout the experiments by measuring mass loss of deionized water from the inlet reservoir. The average flow rate was between 1.9 to 2.1 mL/min. Liquid water evaporated as it entered the preheated portion of the steam-jet capillary resulting in a rapid expansion to high-velocity steam. The velocity of the gas being ejected from the capillary was modeled using Computational Fluid Dynamics (CFD) analysis on ANSYS (ANSYS CFX, ANSYS Inc., Canonsburg, PA). Inputs to the CFD model are the mass flow rate of liquid water into the capillary, the steam-jet temperature, and the geometry of the steam-jet system shown in Figure 3.1. A representative plot of the gas velocity distribution over the sample surface at 1400°C with a liquid flow rate of 2.0 mL/min can be seen in Figure 3.2. The steam temperature was measured prior to the beginning of experiments by inserting a thermocouple (Type R) from the open outlet side of the furnace tube and positioning it approximately 1 mm from the outlet of the capillary (the same location as the sample during testing) with the steam-jet running. The furnace was set to ensure that the average steam temperature was 1200, 1300, or 1400°C before experiments began. Experiments were carried out at 1400°C for 8 and 60h for SiO_2 , phase pure $\text{Y}_2\text{Si}_2\text{O}_7$ and Y_2SiO_5 , and Y_2O_3 . Exposures of 60h were done for $\text{Y}_2\text{Si}_2\text{O}_7$ at 1200, 1300, 1400°C to obtain temperature dependence, and exposures of 125h and 250h were done for phase pure $\text{Y}_2\text{Si}_2\text{O}_7$ at 1400°C to obtain time dependence. Exposures of 60, 125, and 250h at 1200, 1300, and 1400°C were done for all APS materials.

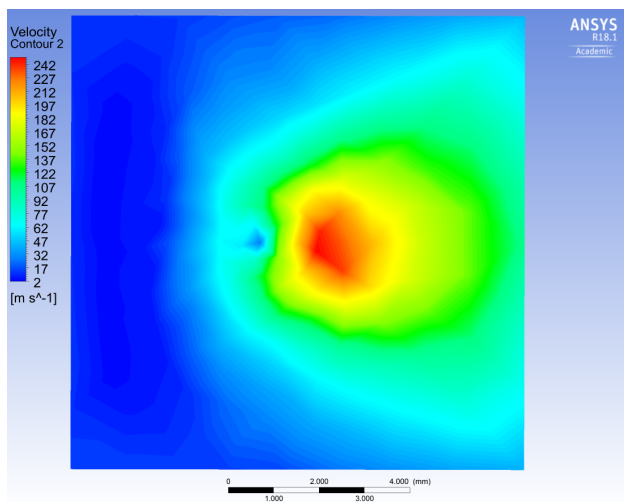


Figure 3.2: A velocity profile on the surface of a sample tested in the steam-jet at 1400°C with an assumed deionized water flow rate of 2.0 mL/min. This velocity distribution was modeled using ANSYS. The high velocity location represents the steam impingement point 1 mm from the capillary outlet.

Experiments were performed at 1 atm of $\text{H}_2\text{O}(\text{g})$ with the velocity distribution on the surface of a sample ranging from 10 to 250 m/s. The test specimens were placed in an alumina sample holder at a 45° angle to

the capillary outlet as seen in Figure 3.1. The alumina sample holder was inserted into the furnace from the outlet side and locked into place.

A PtRh capillary was used in this study instead of fused quartz capillaries used in previous studies [49] [29]. Fused quartz capillaries suppress the reaction between $Y_2Si_2O_7$ and $H_2O(g)$ at temperatures above $1200^\circ C$ due to the presence of $Si(OH)_4(g)$ in the gas stream in excess of the equilibrium partial pressure given by Reactions 2 and 3. The oxygen partial pressure was measured to be less than 1% at the outlet of the capillary using an oxygen sensor.

3.2.3 Characterization

All samples were weighed (XPR Analytical Balance, Mettler Toledo, Columbus, OH) before and after testing in the steam-jet. The phase content of the samples was characterized using XRD (Emperyan XRD). After exposure, SiO_2 samples were coated with Cr using a Precision Etching and Coating System (Gatan 682 PECS, Gatan, Inc., Pleasanton, CA) to create an opaque surface for optical profilometry. Optical profilometry (Zygo NewView 7300, Zygo Corporation, Middlefield, CT) of SiO_2 was used to characterize the impingement site recession that resulted from steam-jet testing. Contact profilometry (Bruker DektakXT Stylus Profilometer, Bruker Corp., Tucson, AZ) was also used to complement the optical data. After exposure, $Y_2Si_2O_7$, Y_2SiO_5 , and Y_2O_3 samples were coated with AuPd for plan view characterization in the SEM. $Y_2Si_2O_7$, Y_2SiO_5 , and Y_2O_3 samples were also characterized in cross-section. Cross-sectioned samples were polished using standard polishing methods from 500 grit SiC paper to $0.25 \mu m$ SiO_2 colloidal silica.

Gas boundary layer theory was used to calculate the material loss for SiO_2 during steam-jet exposures. A flux equation which describes SiO_2 mass loss controlled by gas phase diffusion out of a boundary layer created during laminar flow over a flat plate is given in Equation 3.1 [50] [51] [52]. The flux, in $\frac{g}{cm^2 sec}$, depends on ρ' the gas density of the boundary layer, v the gas velocity, L the characteristic length of the test specimen, η the gas viscosity of the boundary layer, D_{AB} the interdiffusion coefficient of $Si(OH)_4(g)$ in the laminar boundary layer of $H_2O(g)$, and $\rho_{Si(OH)_4(g)}$ the gas density of $Si(OH)_4(g)$. The dimensionless Reynold's number is given by $\frac{\rho'vL}{\eta}$ and the dimensionless Schmidt number is $\frac{\eta}{\rho'D_{AB}}$. Gas densities were calculated using the ideal gas law.

$$J_{SiO_2} = J_{Si(OH)_4(g)} \cdot \frac{MW_{SiO_2}}{MW_{Si(OH)_4(g)}} = \frac{0.664 \left(\frac{\rho'vL}{\eta} \right)^{1/2} \left(\frac{\eta}{\rho'D_{AB}} \right)^{1/3} \rho_{Si(OH)_4(g)}}{L} \cdot \frac{MW_{SiO_2}}{MW_{Si(OH)_4(g)}} \quad (3.1)$$

Recession of SiO_2 is then calculated by dividing the flux of SiO_2 by the density of SiO_2 , resulting in a rate relationship, given in Equation 3.2. Typical inputs for Equations 3.1 and 3.2 are given in Table 3.1.

Equilibrium partial pressures of $\text{Si}(\text{OH})_4(\text{g})$ with members of the Y_2O_3 - SiO_2 system and energies of reaction between $\text{Y}_2\text{Si}_2\text{O}_7$, Y_2SiO_5 , and H_2O were calculated using the Factsage equilibrium and reaction tools respectively and data calculated by Fabrichnaya et al. [53] [10] [54].

$$\text{recessionrate} = \frac{\Delta x}{t} = \frac{J_{\text{SiO}_2}}{\rho_{\text{SiO}_2}} \quad (3.2)$$

Table 3.1: Parameters used in Equations 3.1 and 3.2 for SiO_2 volatility

Symbol	Definition	Units	Typical Value at 1400°C	Comments
Δx	Material recession	μm	350 or 525	Measured from experiment
t	Exposure time	h	60	Experimental variable
ρ'	Boundary layer gas density	$\frac{\text{g}}{\text{cm}^3}$	$1.31 \cdot 10^{-4}$	$\text{H}_2\text{O}(\text{g})$, calculated with ideal gas law
ρ_{SiO_2}	Density of α -Cristobalite	$\frac{\text{g}}{\text{cm}^3}$	2.32	
v	Free stream gas velocity	$\frac{\text{m}}{\text{s}}$	250	Experimental variable, calculated using ANSYS [55]
L	Characteristic length	cm	1.25	Length of coupon
η	Boundary layer gas viscosity	$\frac{\text{g}}{\text{cm} \cdot \text{s}}$	$5.73 \cdot 10^{-4}$	$\text{H}_2\text{O}(\text{g})$ from Ref [56]
D_{AB}	Interdiffusion coefficient of $\text{Si}(\text{OH})_4(\text{g})$ species in laminar boundary layer of $\text{H}_2\text{O}(\text{g})$	$\frac{\text{cm}^2}{\text{s}}$	2.68	From Chapman Enskog equation [57]; collision diameter and integral of SiF_4 (Ref [56]) used as estimate for $\text{Si}(\text{OH})_4(\text{g})$
$P_{\text{H}_2\text{O}(\text{g})}$	Partial pressure of $\text{H}_2\text{O}(\text{g})$	atm	1	Experimental variable
$P_{\text{Si}(\text{OH})_4(\text{g})}$	Partial pressure of $\text{Si}(\text{OH})_4(\text{g})$	atm	$6 \cdot 10^{-6}$	Calculated using FactSage SGPS database [53]
MW_{SiO_2}	Molecular weight of SiO_2	$\frac{\text{g}}{\text{mol}}$	60	
$MW_{\text{Si}(\text{OH})_4(\text{g})}$	Molecular weight of $\text{Si}(\text{OH})_4(\text{g})$	$\frac{\text{g}}{\text{mol}}$	96	
R	Gas constant	$\frac{\text{cm}^3 \cdot \text{atm}}{\text{mol} \cdot \text{K}}$	82.06	
T	Absolute temperature	K	1673	

3.3 Results

The results of steam-jet testing across the SiO_2 - Y_2O_3 system are presented here first, moving across the phase diagram from more to less SiO_2 content. SiO_2 recession measurements are compared to calculations made using Equations 3.1 and 3.2. $\text{Y}_2\text{Si}_2\text{O}_7$ samples exposed in the steam-jet show transformation to Y_2SiO_5 with trace amounts of Y_2O_3 formed on the surface of these Y_2SiO_5 layers. This formation of Y_2O_3 on Y_2SiO_5

is also observed in samples of pure Y_2SiO_5 . Y_2O_3 shows no material loss in the steam-jet through reaction with water vapor or mechanical erosion.

Steam-jet exposures of phase pure $Y_2Si_2O_7$ at $1400^\circ C$ for 60, 125, and 250h are then compared and parabolic kinetics are observed for the reaction between $Y_2Si_2O_7$ and $H_2O(g)$. The data for phase pure $Y_2Si_2O_7$ exposed at $1400^\circ C$ for 60h is then compared to exposures at 1200 and $1300^\circ C$ for 60h to calculate an activation energy of the reaction between $Y_2Si_2O_7$ and $H_2O(g)$.

The results of steam-jet exposures from 1200- $1400^\circ C$ and 60-250h on dense and porous APS $Yb_2Si_2O_7$ coatings provided by Rolls-Royce are then shown.

3.3.1 Stability of Phases in the Y_2O_3 - SiO_2 System at $1400^\circ C$

SiO_2

The SiO_2 samples partially devitrified after $1400^\circ C$ exposures in the steam-jet. XRD analysis showed cristobalite SiO_2 along with evidence of amorphous SiO_2 , shown in Figure 3.3.

The SiO_2 impingement site in the samples showed a smooth recession profile with an additional large pit. Optical profilometry of the SiO_2 sample exposed at $1400^\circ C$ for 60h can be seen in Figure 3.4 with a noticeable dropout of signal in the impingement area. A few points were obtained from the edges of the pit in the impingement zone. A line profile was drawn through these points and a depth profile was interpolated, seen in Figure 3.5. Contact profilometry was done to get more complete data on the depth profile of the impingement site, shown in Figure 3.6. A smooth recession profile, drawn in red in Figure 3.6, with a depth of $\sim 350 \mu m$ was measured with a pit below this measuring $\sim 525 \mu m$. The experimentally observed recession rate is $5.83 \mu m/h$ when considering the smooth recession profile and $8.75 \mu m/h$ when considering the deepest pit, assuming linear kinetics.

A second SiO_2 sample was exposed at $1400^\circ C$ for 8h in the steam-jet to confirm the recession rate observed at 60h. This sample again showed pronounced recession. Optical profilometry of this sample can be seen in Figure 3.7 with less signal dropout observed in this profile. A line scan through the impingement site shows a maximum recession through a smooth profile, bounded in red, of $60 \mu m$ with a pit depth of $\sim 75 \mu m$, shown in Figure 3.8. Contact profilometry complements the optical profilometry results obtained, with a smooth recession profile bounded in red of $\sim 50 \mu m$ and maximum recession in the pit of $\sim 75 \mu m$, shown in Figure 3.9. The observed recession rate is $6.25 \mu m/h$ through the smooth profile and $8.75 \mu m/h$ through the pit, assuming linear kinetics.

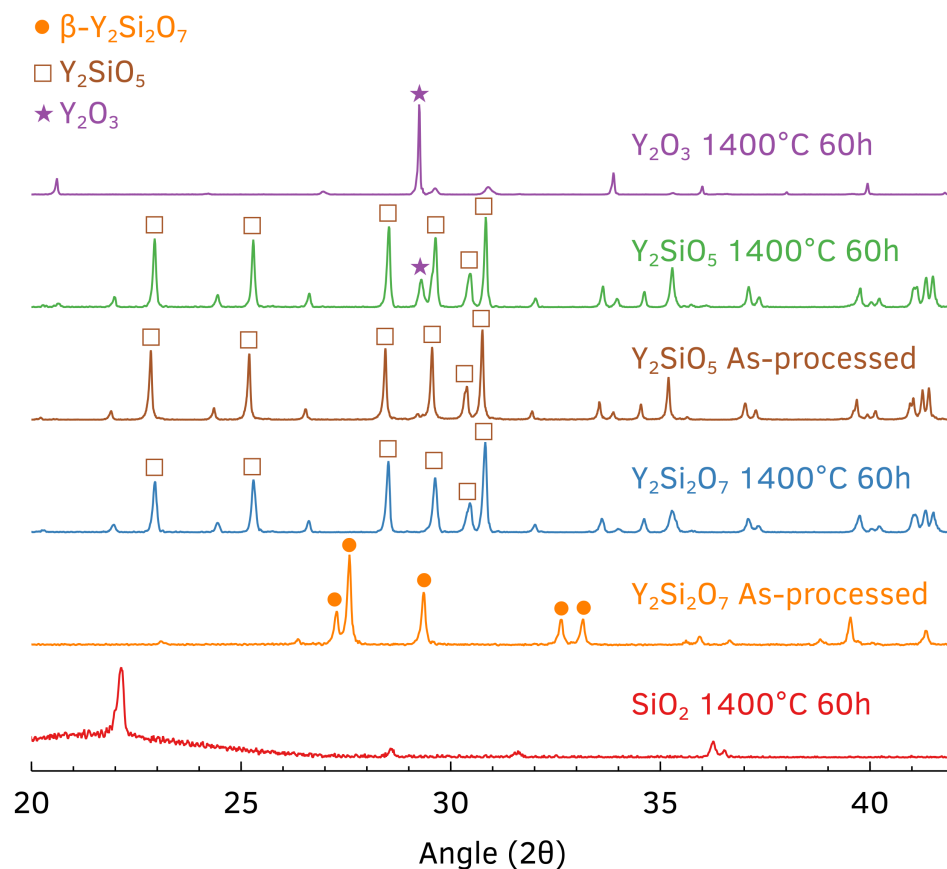


Figure 3.3: XRD results for $\text{Y}_2\text{Si}_2\text{O}_7$ and Y_2SiO_5 before exposure and all samples after exposure at 1400°C for 60h. Note that the $\text{Y}_2\text{Si}_2\text{O}_7$ sample after exposure shows only peaks from the surface layer of Y_2SiO_5 product phase.

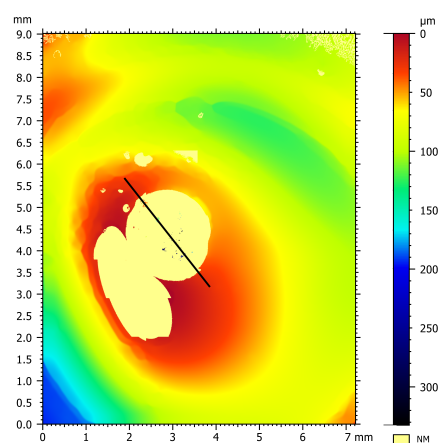


Figure 3.4: A surface profile map of a SiO_2 sample exposed in the steam-jet furnace with 1 atm $\text{H}_2\text{O}(\text{g})$ at 1400°C for 60h. There is a large amount of signal dropout in the impingement site area due to the depth of the impingement site. The few data points collected come from the edges of pits measured at the bottom of the impingement site.

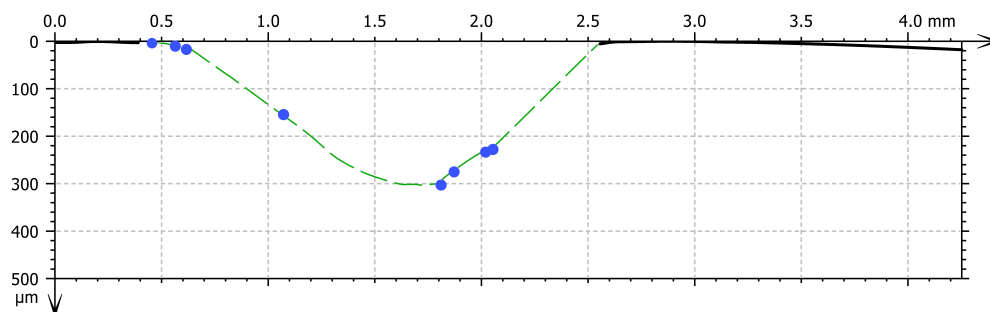


Figure 3.5: A line profile for SiO_2 , exposed in the steam-jet furnace with 1 atm $\text{H}_2\text{O}(\text{g})$ at 1400°C for 60h, created from the surface profile map shown in Figure 3.4. The points show the areas of measured data in the impingement site. The dotted line is an interpolation from these points.

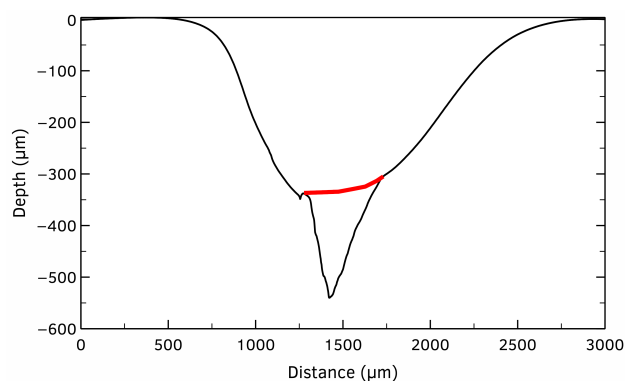


Figure 3.6: A line profile of the depth of recession of SiO_2 exposed in the steam-jet furnace with 1 atm $\text{H}_2\text{O}(\text{g})$ at 1400°C for 60h obtained from contact profilometry.

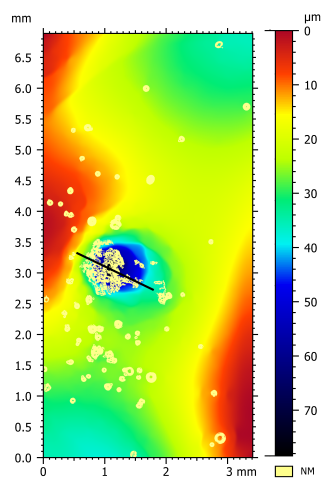


Figure 3.7: A surface profile map of a SiO_2 sample exposed in the steam-jet furnace with 1 atm $\text{H}_2\text{O}(\text{g})$ at 1400°C for 8h. Signal dropout (yellow areas) is observed.

Equations 3.1 and 3.2 were used with inputs from Table 3.1 to determine the expected recession of SiO_2 during exposure at 1400°C for 60 h with a maximum gas velocity of 250 m/s. Results from experiments and

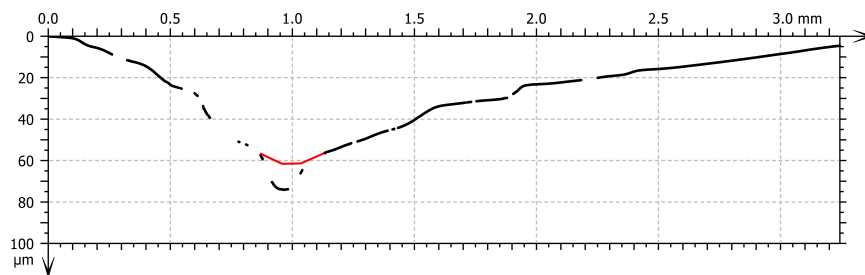


Figure 3.8: A line profile for SiO_2 , exposed in the steam-jet furnace with 1 atm $\text{H}_2\text{O}(\text{g})$ at 1400°C for 8h, created from the surface profile map shown in Figure 3.7. More data were obtained here as compared to Figure 3.5.

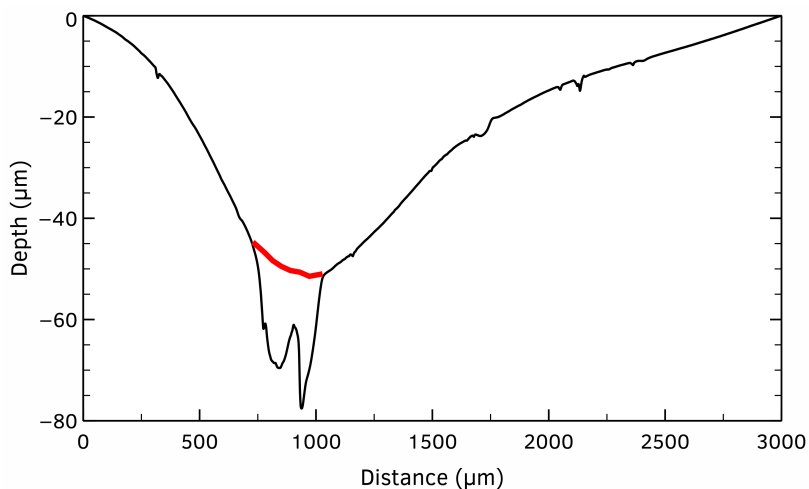


Figure 3.9: A contact profile of the surface of the SiO_2 sample exposed at 1400°C for 8h in the steam-jet furnace.

calculations are summarized in Table 3.2. The calculated recession rate was $6.39 \mu\text{m}/\text{h}$, predicting a total recession of $383.4 \mu\text{m}$ over a 60 h test.

Table 3.2: Bounded experimental recession rate results of SiO_2 exposures to $\text{H}_2\text{O}(\text{g})$ at 1400°C and a maximum gas velocity of 250 m/s compared to calculation.

	Recession (μm)		Recession Rate ($\mu\text{m}/\text{h}$)		Calculated rate from Equations 3.1 and 3.2
	8h	60h	8h	60h	
min	50	350	6.25	5.83	6.39
max	75	525	8.75	9.38	

SPS $Y_2Si_2O_7$

XRD analysis of $Y_2Si_2O_7$ exposed at $1400^\circ C$ for 60h in the steam-jet furnace showed the presence of $Y_2Si_2O_7$, Y_2SiO_5 , and Y_2O_3 , shown in Figure 3.3. Weight loss occurred during testing, consistent with the loss of SiO_2 from reaction of $Y_2Si_2O_7$ with $H_2O(g)$ by Reactions 2 and 3.

Figure 3.10 shows an as-processed SPS $Y_2Si_2O_7$ sample. Some porosity is present, with grain sizes on the order of $\sim 20 \mu m$, as determined from the intercept method using ImageJ on another specimen. The samples were phase pure $Y_2Si_2O_7$ with the exception of the presence of trace ZrO_2 contaminant from ball milling, shown with the blue arrow. After testing, the microstructure 1 mm downstream from the impingement site, with $v_g \sim 195$ m/s shows porous Y_2SiO_5 with grain sizes on the order of ~ 1 micron in diameter as shown in Figure 3.11. The volume change with the formation of Y_2SiO_5 from $Y_2Si_2O_7$ (Reaction 2) results in a decrease in volume of 25%, based on molar volume calculations.

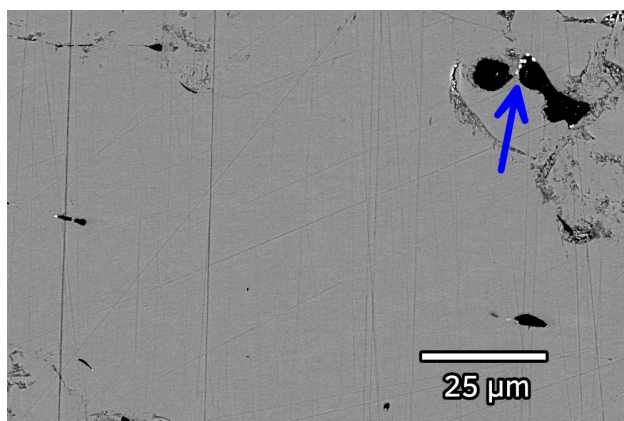


Figure 3.10: A backscattered electron SEM plan view image of the as-processed microstructure of SPS $Y_2Si_2O_7$. ZrO_2 contamination from the milling media can be seen in the pore as the brightest phase, pointed out by the blue arrow.

Cross sectional analysis revealed two distinct microstructural regimes. At velocities of ~ 180 m/s an average Y_2SiO_5 thickness of $38 \pm 2 \mu m$ is observed, seen in Figure 3.12. Cracks and a $\sim 5 \mu m$ thick dense layer near the surface form as well. In contrast to this, Figure 3.13 shows areas exposed to velocities ~ 225 m/s. A thinner layer of Y_2SiO_5 has formed, with dense layers observed closer to the $Y_2Si_2O_7/Y_2SiO_5$ reaction interface than those seen in Figure 3.12. Y_2O_3 , noted by higher contrast, can be seen on the surface of this dense Y_2SiO_5 layer, shown in higher magnification in Figure 3.14.

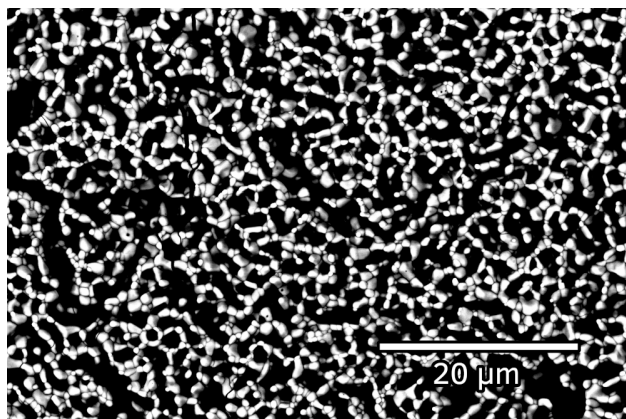


Figure 3.11: A backscattered electron SEM plan view image of SPS $Y_2Si_2O_7$ exposed in the steam-jet furnace at $1400^\circ C$ for 60 h with $P_{H_2O} = 1$ atm and $v_g = 195$ m/s. Y_2SiO_5 is the only phase visible at this location, with pores forming from the volume change that occurred upon reaction of $Y_2Si_2O_7$ with $H_2O(g)$.

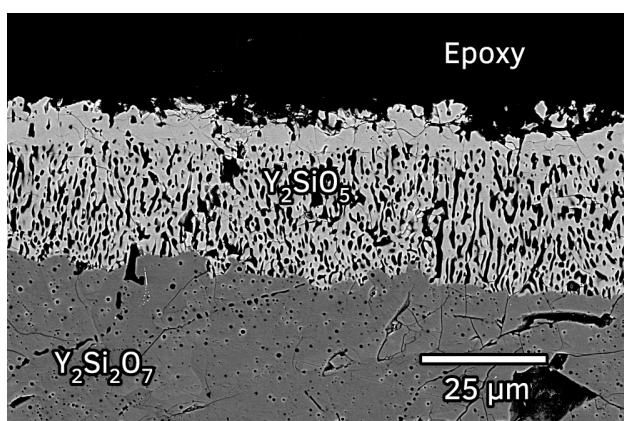


Figure 3.12: A backscattered electron SEM cross-sectional image of SPS $Y_2Si_2O_7$ exposed in the steam-jet furnace at $1400^\circ C$ for 60 h with $P_{H_2O} = 1$ atm and $v_g = 180$ m/s.

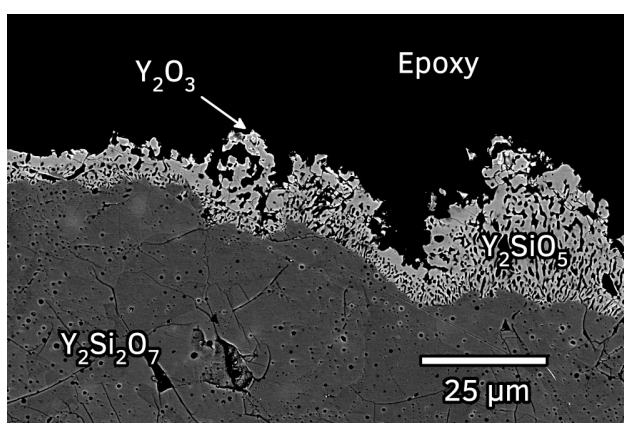


Figure 3.13: A backscattered electron SEM cross-sectional image of SPS $Y_2Si_2O_7$ exposed in the steam-jet furnace at $1400^\circ C$ for 60 h with $P_{H_2O} = 1$ atm and $v_g = 225$ m/s.

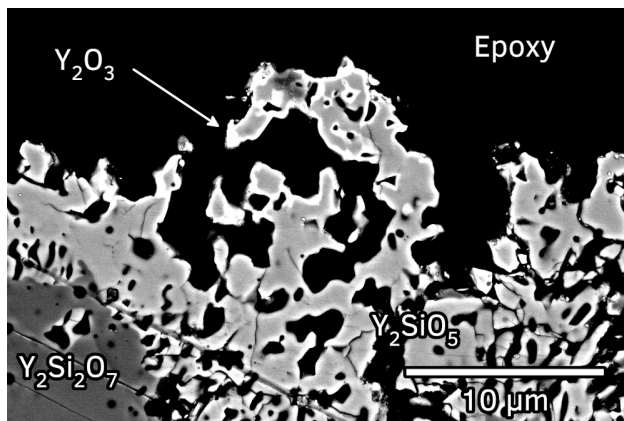


Figure 3.14: A backscattered electron SEM cross-sectional image of SPS $Y_2Si_2O_7$ exposed in the steam-jet furnace at $1400^\circ C$ for 60 h with $P_{H_2O} = 1$ atm and $v_g = 200$ m/s. This higher magnification image shows the Y_2O_3 formation on the surface from Figure 3.13.

SPS Y_2SiO_5

Y_2SiO_5 samples exposed at $1400^\circ C$ for 60h in steam-jet furnace had initial grains sizes of $> 20 \mu m$. Figure 3.15 shows the microstructure of the Y_2SiO_5 after exposure at $v_g = 10$ m/s; no reaction has occurred. Figure 3.16 shows the microstructure on the surface of the sample at $v_g = 195$ m/s, 1 mm downstream from the highest velocity regions on the sample. The backscattered electron image here has higher contrast than seen in Figure 3.15, consistent with the formation of Y_2O_3 . XRD results, seen in Figure 3.3, confirm the presence of Y_2O_3 . The formation of the Y_2O_3 is accompanied by pore formation due to the 30% decrease in volume from Y_2SiO_5 to Y_2O_3 (Reaction 3), as well as ridge formations. A clear boundary exists between the newly formed Y_2O_3 and the unreacted Y_2SiO_5 as shown in Figure 3.17. This boundary is found where the gas velocity is ~ 150 m/s.

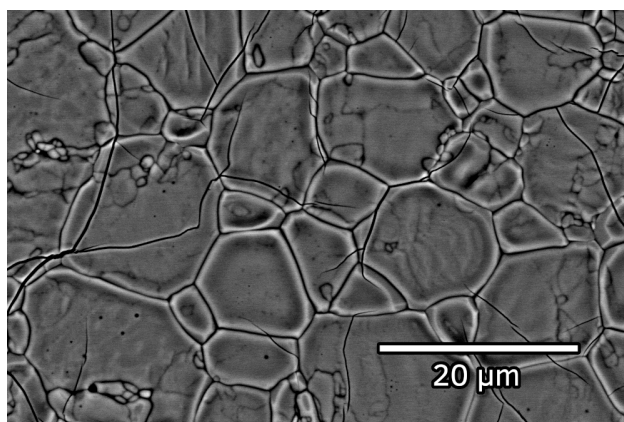


Figure 3.15: A backscattered electron SEM plan view image of SPS Y_2SiO_5 exposed in the steam-jet furnace at $1400^\circ C$ for 60 h with $P_{H_2O} = 1$ atm and $v_g = 10$ m/s.

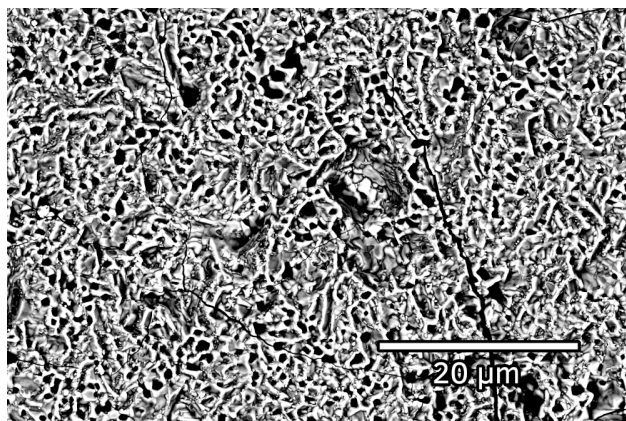


Figure 3.16: A backscattered electron SEM plan view image of SPS Y_2SiO_5 exposed in the steam-jet furnace at 1400°C for 60 h with $\text{P}_{\text{H}_2\text{O}} = 1$ atm and $v_g = 195$ m/s.

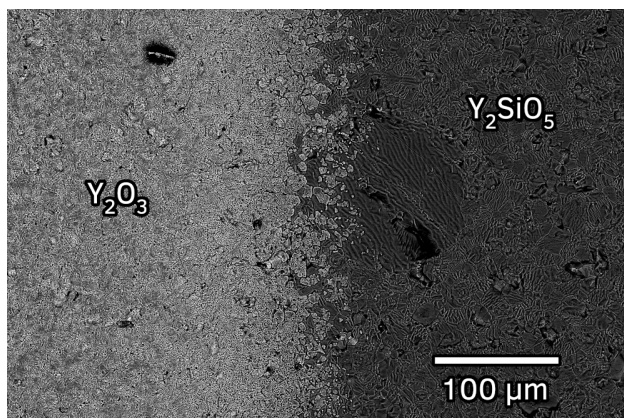


Figure 3.17: A backscattered electron SEM plan view image of SPS Y_2SiO_5 exposed in the steam-jet furnace at 1400°C for 60 h with $\text{P}_{\text{H}_2\text{O}} = 1$ atm and $v_g = 150$ m/s. A clear boundary can be observed between the formation of Y_2O_3 on the left and the original Y_2SiO_5 on the right.

Cross sectional analysis of the Y_2SiO_5 samples exposed at velocities of ~ 195 m/s showed the formation of a thin layer ($\sim 1 \mu\text{m}$) of Y_2O_3 on the exposed surfaces of the Y_2SiO_5 , shown in Figure 3.18. This formation is similar to the Y_2O_3 observed on $\text{Y}_2\text{Si}_2\text{O}_7/\text{Y}_2\text{SiO}_5$ in Figure 3.14.

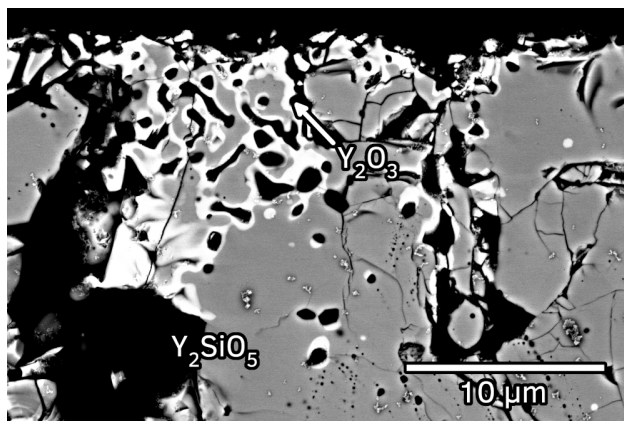


Figure 3.18: A backscattered electron SEM cross-sectional image of SPS Y_2SiO_5 exposed in the steam-jet furnace at $1400^\circ C$ for 60 h with $P_{H_2O} = 1\ atm$ and $v_g = 195\ m/s$.

Y_2O_3

Figure 3.19 shows the microstructure of a Y_2O_3 coupon exposed in a stagnant air box furnace at $1400^\circ C$ for 24 h as a baseline for comparison with steam-jet exposures. Pores are observed in this baseline material. No Y_2O_3 recession was observed after exposure at $1400^\circ C$ 60h in the steam-jet furnace. However, faceting of the Y_2O_3 was observed, as seen in Figure 3.20. Y_2SiO_5 was observed on the surface of the Y_2O_3 in areas with low steam-jet velocities, due to SiO_2 contamination which will be discussed later. XRD results, seen in Figure 3.3, do not show this Y_2SiO_5 formation.

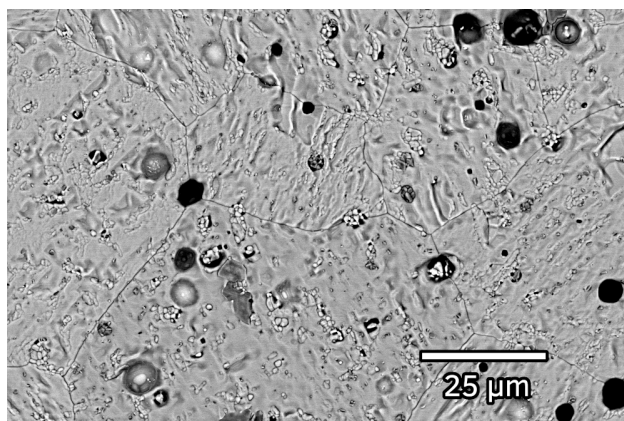


Figure 3.19: A backscattered electron SEM image of Y_2O_3 exposed in a stagnant air box furnace at $1400^\circ C$ for 24 h.

Optical profilometry, seen in Figure 3.21 showed no recession of the Y_2O_3 material, confirmed in a line profile shown in Figure 3.22. The lack of recession suggests no gaseous products formed from a reaction between $H_2O(g)$ and Y_2O_3 .

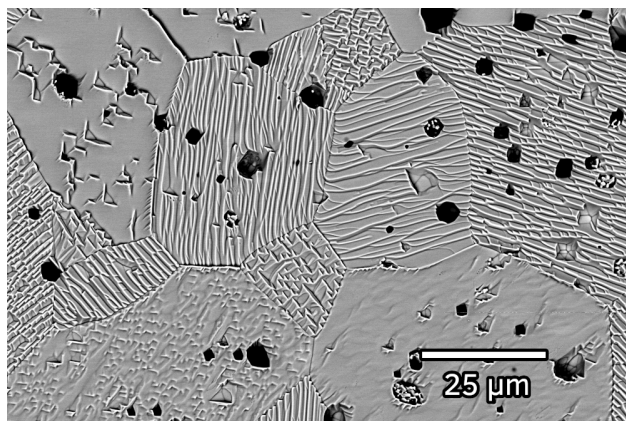


Figure 3.20: A backscattered electron SEM image of Y_2O_3 exposed in the steam-jet furnace at 1400°C for 60 h with $P_{\text{H}_2\text{O}} = 1$ atm and $v_g = 225$ m/s.

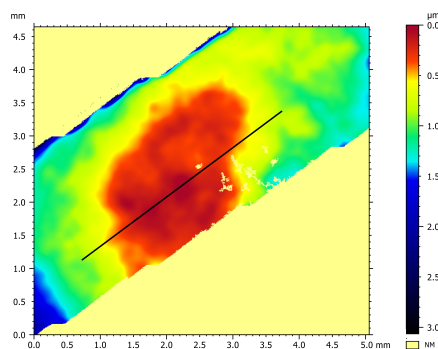


Figure 3.21: A surface map obtained from optical profilometry showing no loss of material in the impingement area of the Y_2O_3 sample.

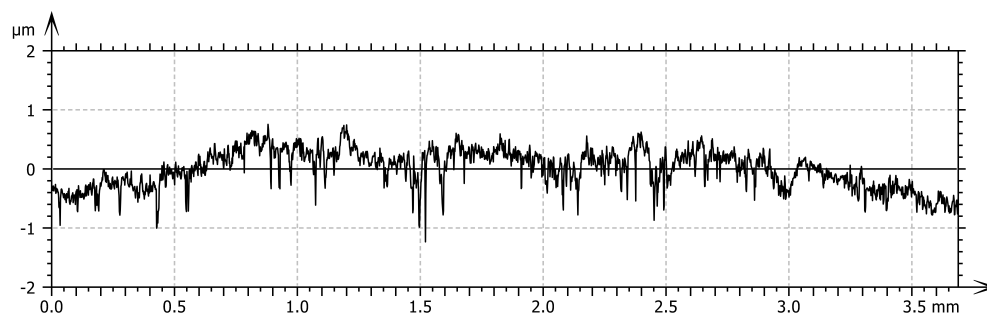


Figure 3.22: A line profile obtained from Figure 3.21 showing a maximum height difference of 2 μm on the surface of the Y_2O_3 sample.

3.3.2 Time Dependence of SiO_2 Depletion in Dense Phase Pure $\text{Y}_2\text{Si}_2\text{O}_7$ at 1400°C

Steam-jet exposures were carried out for 60, 125, and 250h at 1400°C to determine the reaction kinetics of $\text{Y}_2\text{Si}_2\text{O}_7$ reacting with $\text{H}_2\text{O}(\text{g})$. Figure 3.23 below shows a comparison of cross-sectional images at 60,

125, and 250h after these exposures. The SiO_2 depletion depth increases with time, along with the size of the pores through the thickness of the Y_2SiO_5 layer. The results of measurements of the SiO_2 depletion depth in these three samples in areas of $\text{H}_2\text{O}(\text{g})$ velocity of 130-170 m/s are given in Table 3.3. Each depletion depth is the aggregate of 25 measurements across a cross section in areas where only porous Y_2SiO_5 was observed. The uncertainty is the standard deviation of the data collected. These data were plotted as depletion depth vs $t^{1/2}$ and shown in Figure 3.24. The linear fit to these data suggest parabolic kinetics for the reaction between $\text{H}_2\text{O}(\text{g})$ and $\text{Y}_2\text{Si}_2\text{O}_7$. The square of the slope then provides a parabolic rate constant.

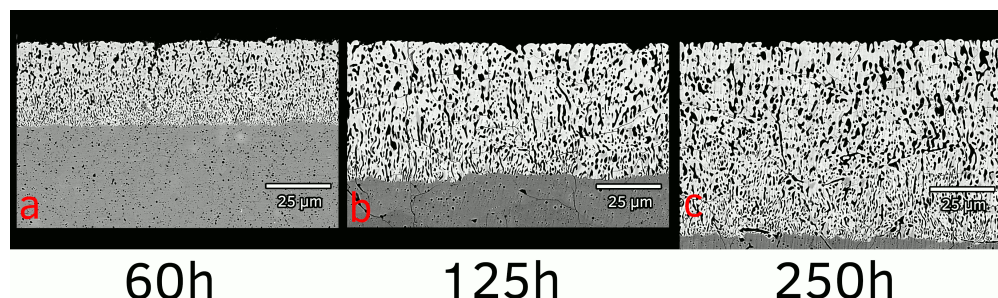


Figure 3.23: A comparison of backscattered electron cross-sectional images showing the SiO_2 depletion depth for dense, phase pure $\text{Y}_2\text{Si}_2\text{O}_7$ samples exposed at 1400°C for 60 (a), 125 (b), and 250h (c). Average gas velocity in these figures is 130-170 m/s.

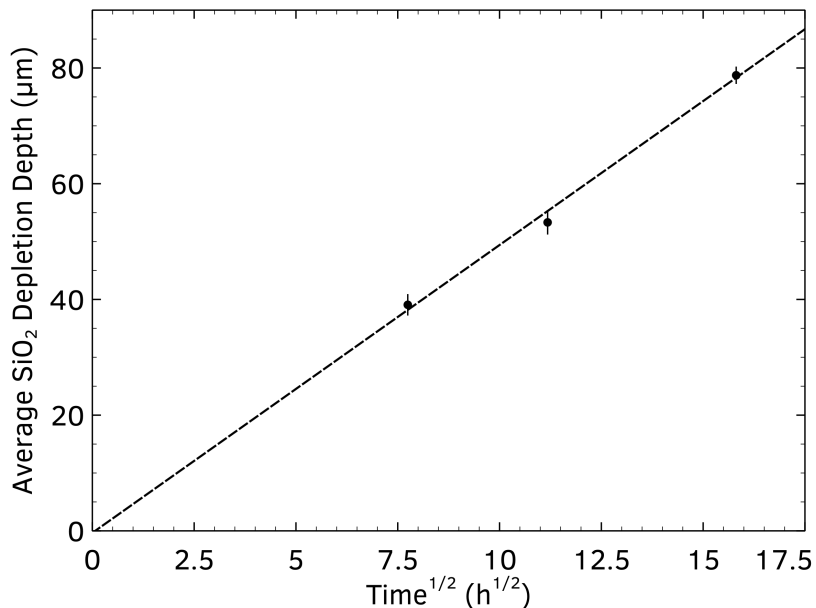


Figure 3.24: Average SiO_2 depletion depth vs $t^{1/2}$ for phase pure $\text{Y}_2\text{Si}_2\text{O}_7$ samples exposed in the steam-jet furnace at 1400°C for 60, 125, and 250h with v_g between 150 and 175 m/s. The dotted line is the linear fit to these data.

Table 3.3: Collected SiO_2 depletion measurements for phase pure $\text{Y}_2\text{Si}_2\text{O}_7$ samples exposed in the steam-jet at 1400°C for 60, 125, and 250h with a gas velocity of 130-170 m/s.

Time (h)	Depletion Depth (μm)
60	39.1 ± 1.9
125	53.3 ± 2.1
250	78.7 ± 1.5

3.3.3 Temperature Dependence of SiO_2 Depletion in Dense Phase Pure $\text{Y}_2\text{Si}_2\text{O}_7$

Steam-jet exposures were carried out at 1200 , 1300 , and 1400°C for 60h on dense phase pure $\text{Y}_2\text{Si}_2\text{O}_7$. A comparison of the plan view microstructure of these samples at 1 mm downstream of the impingement site is given in Figure 3.25. Porosity increased with increasing temperature, as did the coarsening of the pore and grain structure. There are small ZrO_2 impurities left in the microstructure from ball milling, often the brightest phases seen in the images. ZrO_2 reaction with water vapor is negligible and so remains at the surface of the sample. Y_2SiO_5 is visible in these images as the base of the ligament structure. The large geometric brighter phases present in the image for the $\text{Y}_2\text{Si}_2\text{O}_7$ exposed at 1200°C are phases depleted of Si. EDS results showed Y:Si ratios of between 5 and 10. Y_2SiO_5 has a Y:Si ratio of 2, with $\text{Y}_2\text{Si}_2\text{O}_7$ being 1. An EDS spectrum taken at 10 keV on the spot given by the red dot in Figure 3.25 is shown in Figure 3.26 showing a Y:Si ratio of approximately 5. Samples were coated in Au/Pd for SEM analysis, so this signal is expected in small amounts.

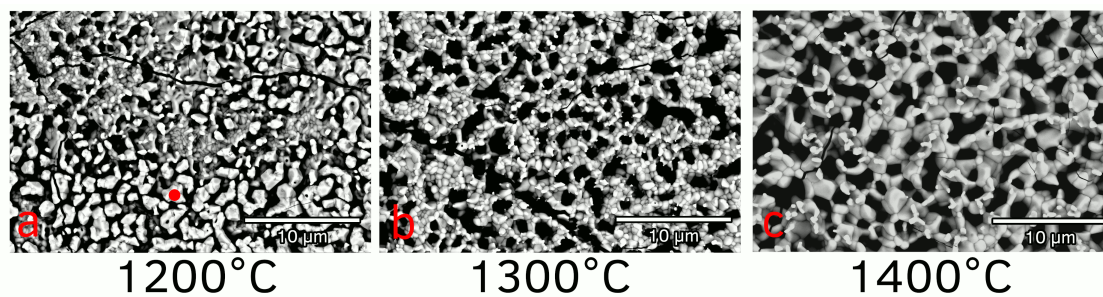


Figure 3.25: A comparison of backscattered electron images taken 1 mm downstream of the impingement site showing the surface morphology change for dense, phase pure $\text{Y}_2\text{Si}_2\text{O}_7$ samples exposed at 1200 ($v_g = 175$ m/s) (a), 1300 ($v_g = 185$ m/s) (b), and 1400°C ($v_g = 195$ m/s) (c) for 60h. The red dot on image a corresponds to the location of the EDS spectrum shown in Figure 3.26.

Cross sectional analysis of these samples shows an increasingly thick layer of Y_2SiO_5 forming as temperature increases, shown in Figure 3.27. Note, these images are shown at a higher magnification relative to prior cross-sectional images due to the small amount of Y_2SiO_5 formed on the surface of the sample exposed at 1200°C . The structure of all samples shows columnar pores and grains at the reaction interface with the coarsening observed toward the surface of the sample. Pore size overall increases greatly with increased tem-

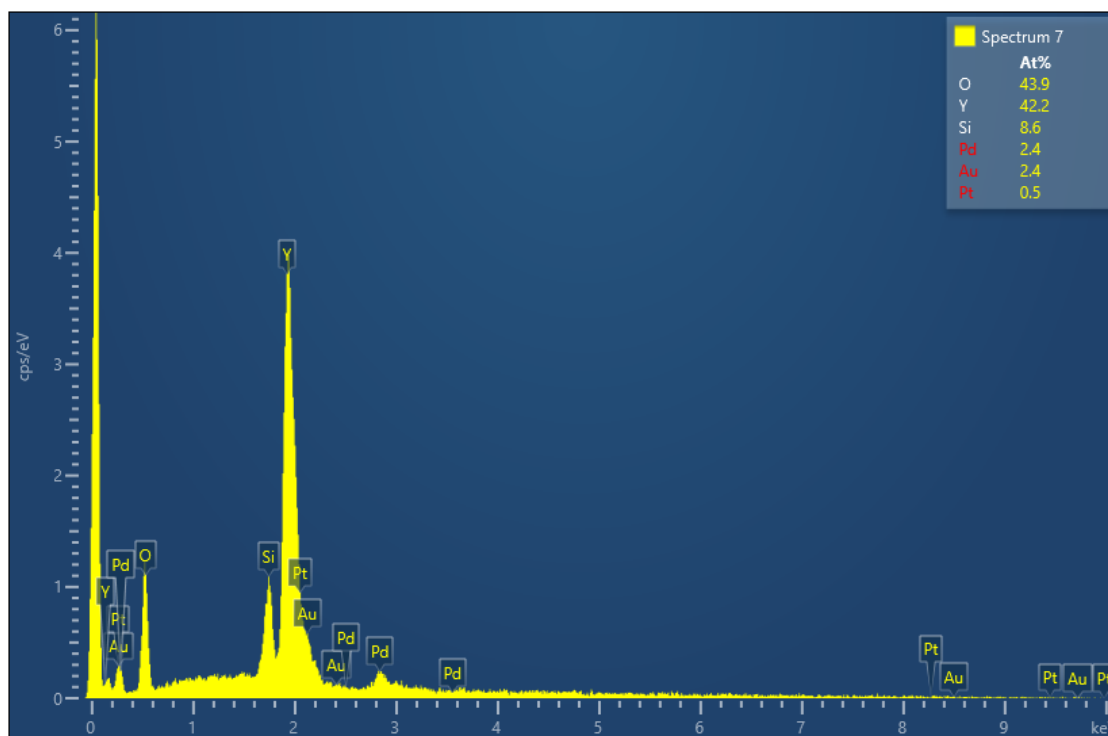


Figure 3.26: EDS spectrum taken at the location designated by the red dot in Figure 3.25. The Y:Si ratio in these microstructural features is approximately 5, which does not match with any equilibrium phase in the $\text{SiO}_2 - \text{Y}_2\text{O}_3$ system. The large peak at 0 keV is a measurement artifact.

Table 3.4: Collected SiO_2 depletion measurements for phase pure $\text{Y}_2\text{Si}_2\text{O}_7$ samples exposed in the steam-jet at 1200, 1300, and 1400°C for 60h with a gas velocity of 130-170 m/s.

Temperature (°C)	Depletion Depth (μm)
1200	6.06 ± 1.0
1300	16.6 ± 1.9
1400	39.1 ± 1.9

perature. The smallest pores at 1400°C are larger than many of the pores at 1300°C and all of the pores seen in the 1200°C exposure. Measurements for the average SiO_2 depletion depth at each temperature are given in Table 3.4, with these data plotted in Figure 3.28. At least 25 measurements were taken per cross section, with the uncertainty listed being the standard deviation of these data. Average SiO_2 depletion depth of dense, phase pure $\text{Y}_2\text{Si}_2\text{O}_7$ exposed in the steam-jet furnace with a fused quartz capillary at 1200°C for 60h are shown in red in Figure 3.28 showing agreement with previous work on these materials [12]. Assuming parabolic kinetics hold, the $\ln(\text{depletion depth}^2/\text{time})$ is plotted against inverse temperature in Figure 3.29, showing an activation energy of this reaction of 382 kJ/mol.

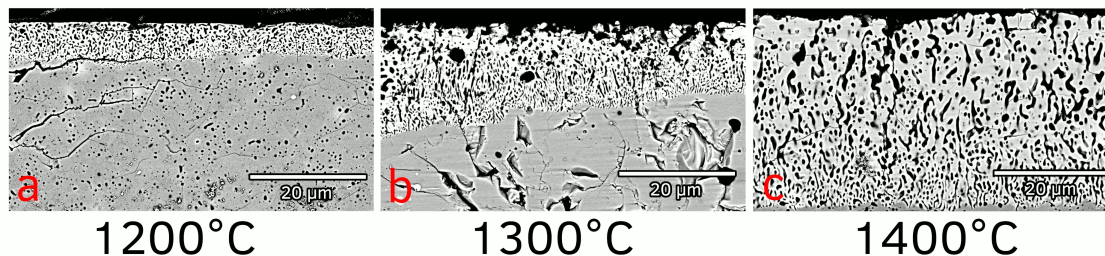


Figure 3.27: A comparison of backscattered electron images taken in cross-section showing the depletion depth for dense, phase pure $\text{Y}_2\text{Si}_2\text{O}_7$ samples exposed at 1200 (a), 1300 (b), and 1400°C (c) for 60h with v_g between 150 and 170 m/s.

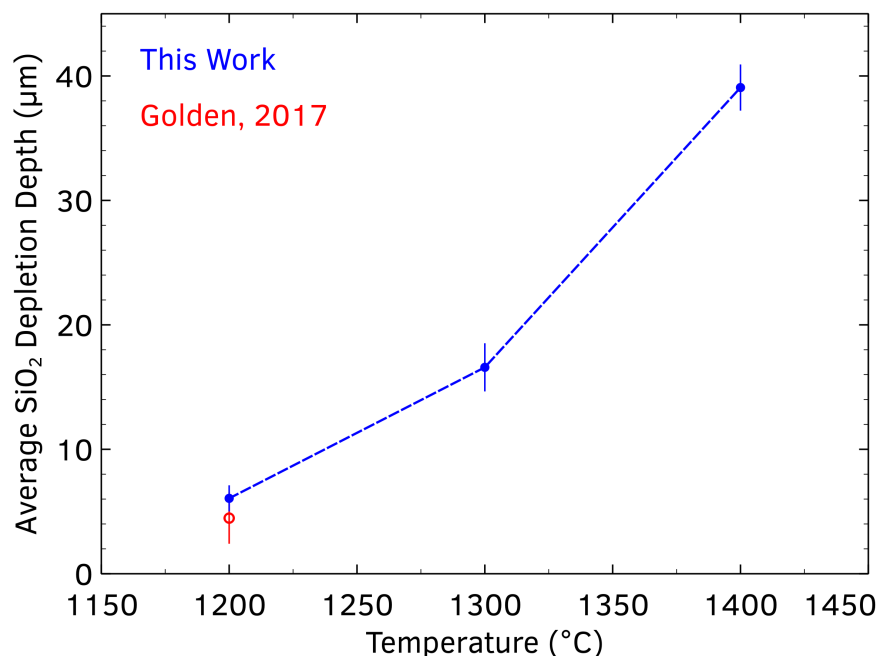


Figure 3.28: Average SiO_2 depletion depth vs. temperature for dense, phase pure $\text{Y}_2\text{Si}_2\text{O}_7$ samples exposed in the steam-jet furnace at 1200, 1300, and 1400°C for 60h with v_g between 150 and 170 m/s. Results from steam-jet exposures carried out using a fused quartz capillary at 1200°C for 60h by Rob Golden (UVA) are shown in red [12].

3.3.4 Velocity Dependence of SiO_2 Depletion in Dense Phase Pure $\text{Y}_2\text{Si}_2\text{O}_7$

Looking at the sample exposed at 1400°C, a velocity dependence can be observed in the same cross section. Figure 3.30 shows images with increasing velocity moving to the right, with the image to the left being the same image shown in Figure 3.27. The thickness of the Y_2SiO_5 layer decreases with increasing velocity, with a pronounced dense Y_2SiO_5 layer being observable in the image in the center. Of particular note is the stark line in the Y_2SiO_5 layer between dense and porous material. The image corresponding to the highest velocity in this cross section shows a nearly completely dense layer of Y_2SiO_5 .

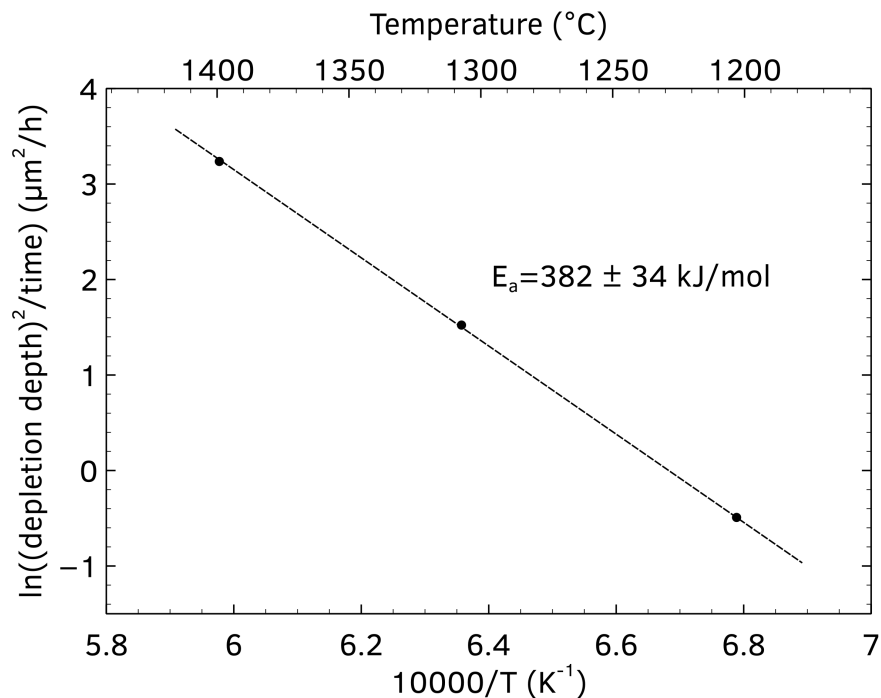


Figure 3.29: $\ln(\text{recession rate}^2)$ vs. $10000/T$ for phase pure $\text{Y}_2\text{Si}_2\text{O}_7$ exposed at 1200, 1300, and 1400°C for 60h, $v_g = 150\text{-}170$ m/s, with a linear fit to the data. The calculated E_a is 382 ± 34 kJ/mol with a 95% confidence interval.

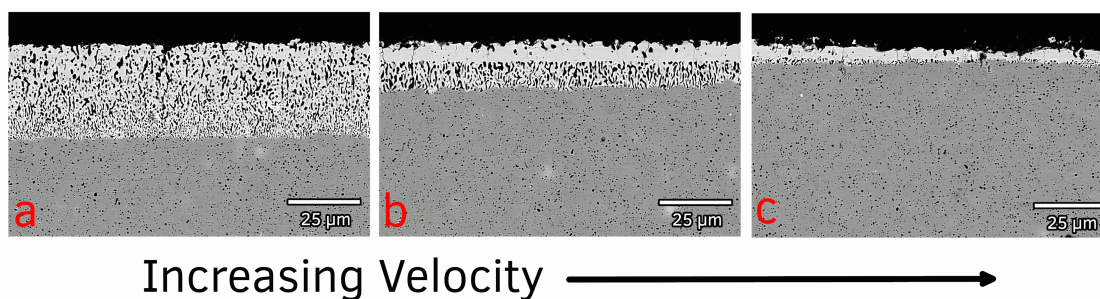


Figure 3.30: Backscattered electron images showing the change in depletion depth and morphology of dense, phase pure $\text{Y}_2\text{Si}_2\text{O}_7$ tested at 1400°C for 60h with approximate velocities of 150 (a), 200 (b), and 240 m/s (c).

3.3.5 Effect of APS on SiO_2 Depletion Kinetics and Microstructural Evolution

Dense APS $\text{Yb}_2\text{Si}_2\text{O}_7$ Coatings Provided by Rolls-Royce

Dense $\text{Yb}_2\text{Si}_2\text{O}_7$ coatings sprayed onto monolithic SiC were received from Rolls-Royce. All APS material described here were of $\text{Yb}_2\text{Si}_2\text{O}_7$, as opposed to the $\text{Y}_2\text{Si}_2\text{O}_7$ chemistry of the SPS samples previously described. SEM images of plan view and cross-sectional views of the coating as-received are shown in Figures 3.31 and 3.32. A mixture of phases can be seen in both images, with the plan view image showing both

splats and smaller grains. Cross-sectional analysis shows splats, cracking, and small amounts of porosity. These dense APS $\text{Yb}_2\text{Si}_2\text{O}_7$ coatings were exposed at 1200, 1300, and 1400°C for 60, 125, and 250h in the steam-jet using the PtRh capillary. Maximum gas velocities range between 230 and 250 m/s.

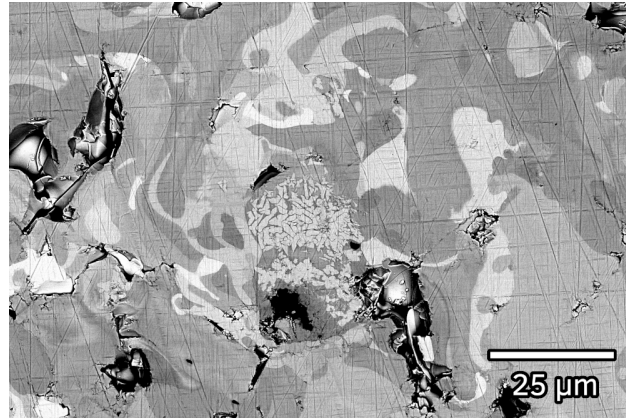


Figure 3.31: A backscattered electron image showing the polished surface in plan view of dense APS $\text{Yb}_2\text{Si}_2\text{O}_7$ coatings provided by Rolls-Royce.

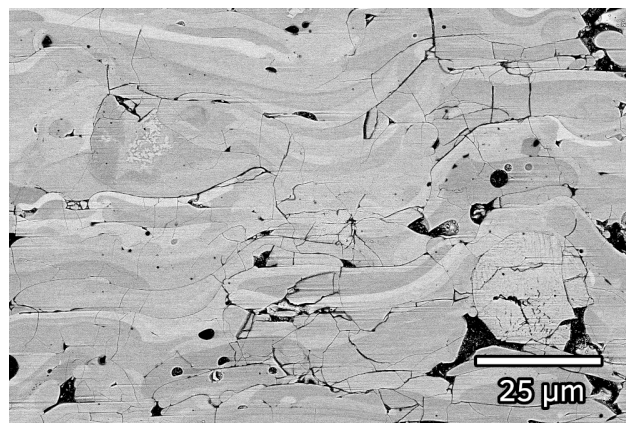


Figure 3.32: A backscattered electron image showing the initial morphology and splat structure in polished cross-section of dense APS $\text{Yb}_2\text{Si}_2\text{O}_7$ coatings provided by Rolls-Royce.

Two trends in microstructure of the surface were observed. Increasing time at the same exposure temperature results in porosity increases. Increasing temperature leads to larger pores and the possibility of Yb_2O_3 formation qualitatively consistent with results for SPS materials. A collage of plan view images from all times and temperatures can be found in Figure 3.33. Thin ligaments of Yb_2O_3 are observed in the exposures at 1300°C for 250h and 1400°C for 125 and 250h. These ligaments contrast with the small equiaxed grains that make up the porous Y_2SiO_5 structure observed in the other exposures. All samples showed material loss at the steam impingement site due to mechanical erosion, as exemplified in Figure 3.34 which shows the impingement site of a $\text{Yb}_2\text{Si}_2\text{O}_7$ coating exposed at 1400°C for 60h. A set of stitched images are presented

in Figure 3.35 to show the erosion experienced at the impingement site from the cross-sectional view. Cross-sectional images at points outside the impingement site are typically characterized to gain understanding of operative thermochemical degradation mechanisms without complications of mechanical erosion.

Cross-sectional analysis showed a general increase in depletion layer thickness with increasing time and temperature. Pore size also increased dramatically with increasing temperature. Figure 3.36 shows a collage of cross-sectional images from all times and temperatures tested. It should be noted that in Figure 3.36 (b) a large crack can be seen penetrating into the coating with SiO_2 depletion observed deeper along this crack than the surrounding material. XRD analysis of as-received APS $\text{Yb}_2\text{Si}_2\text{O}_7$ as well as samples tested for 125h at 1200, 1300, and 1400°C is shown in Figure 3.37. The coating as-received is mostly amorphous, with some $\text{Yb}_2\text{Si}_2\text{O}_7$ and Yb_2SiO_5 crystalline peaks present. After exposure at all temperatures the dominant phase present is Yb_2SiO_5 , with the sample exposed at 1200°C still having some $\text{Yb}_2\text{Si}_2\text{O}_7$ detectable. Yb_2O_3 forms at all temperatures, with increasing abundance with increasing temperature.

The microstructure of the underlying coating played a large role in determining local depletion depth and morphology. Figure 3.38 is a micrograph taken from a cross-section of a sample exposed at 1400°C for 125h and shows how the local microstructure can change depletion behavior. The blue arrow points out where a crack was present in the coating, with increased depletion following this crack deeper into the coating than the surrounding layer. The red circle highlights an area of unreacted $\text{Yb}_2\text{Si}_2\text{O}_7$ surrounded by Yb_2SiO_5 forming from two fronts. The first is the main depletion layer growing from the surface deeper into the coating, the second is the depletion occurring around the large pores surrounding the unreacted area. The splat structure also plays a role in how depletion proceeds over time. Figure 3.39 shows an example of a SiO_2 -poor splat formed during APS processing causing the depletion layer directly above the splat to stop, while continuing deeper into the coating in areas where the splat is not present.

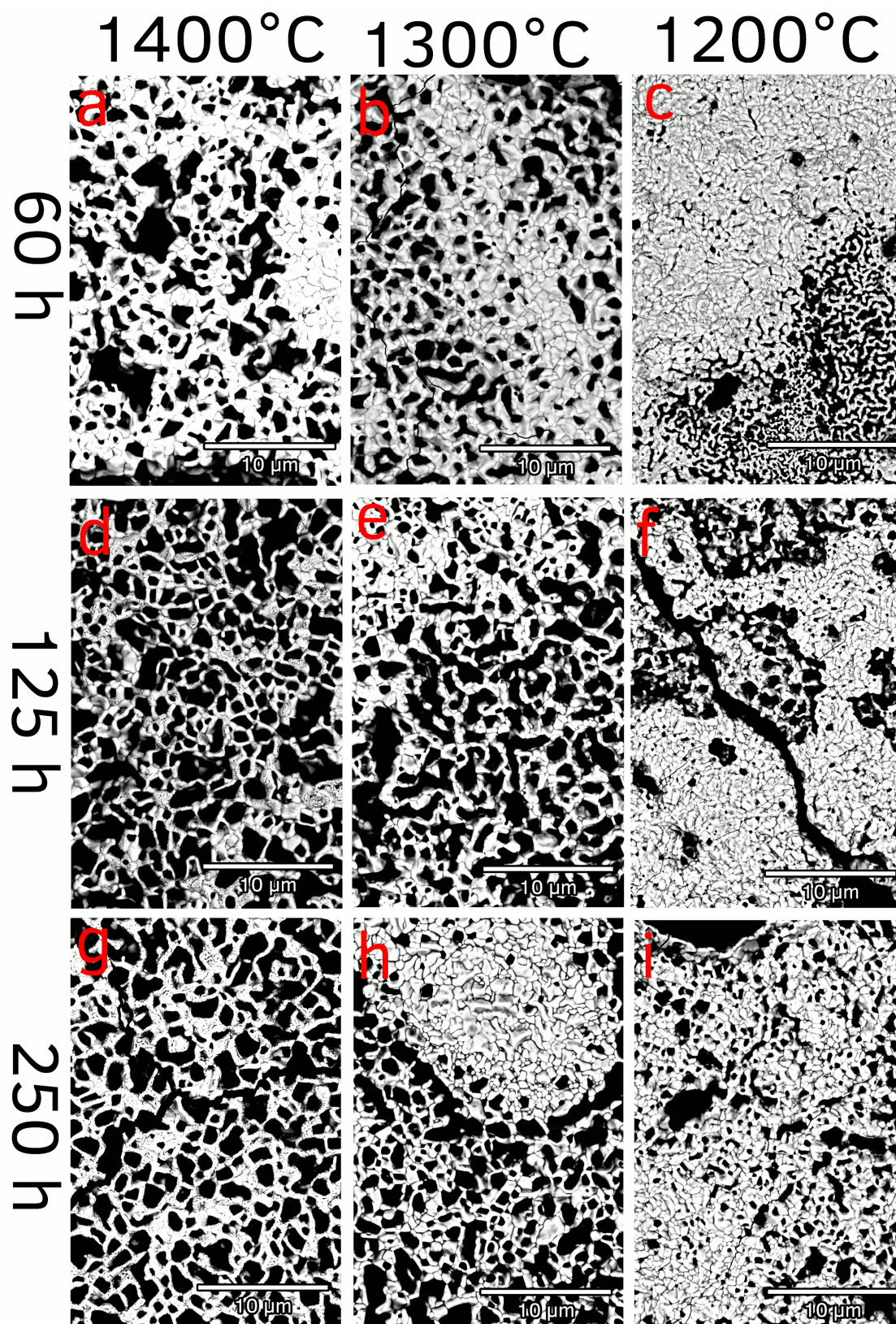


Figure 3.33: A collection of backscattered electron images showing the surface morphology of 1 mm downstream of the impingement site on dense APS $\text{Yb}_2\text{Si}_2\text{O}_7$ coatings exposed at 1200 ($v_g = 175$ m/s), 1300 ($v_g = 185$ m/s), and 1400°C ($v_g = 195$ m/s) for 60, 125, and 250h.

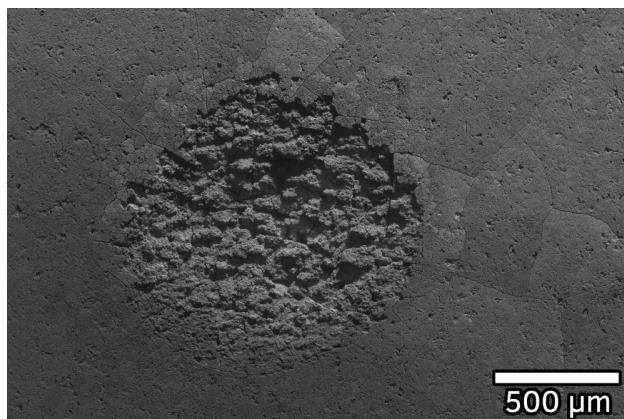


Figure 3.34: A backscattered electron image showing the typical material loss (erosion) experienced at the steam impingement site by dense APS $\text{Yb}_2\text{Si}_2\text{O}_7$ coatings exposed in the steam-jet furnace at 1400°C for 60h. The $v_g = 250$ m/s at the center of the impingement site.

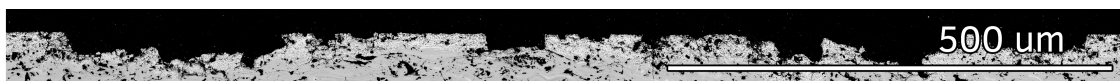


Figure 3.35: Stitched backscattered electron images showing material loss (erosion) experienced at the steam impingement site by dense APS $\text{Yb}_2\text{Si}_2\text{O}_7$ coatings exposed in the steam-jet furnace at 1200°C for 250h. The highest v_g experienced in this area was 230 m/s.

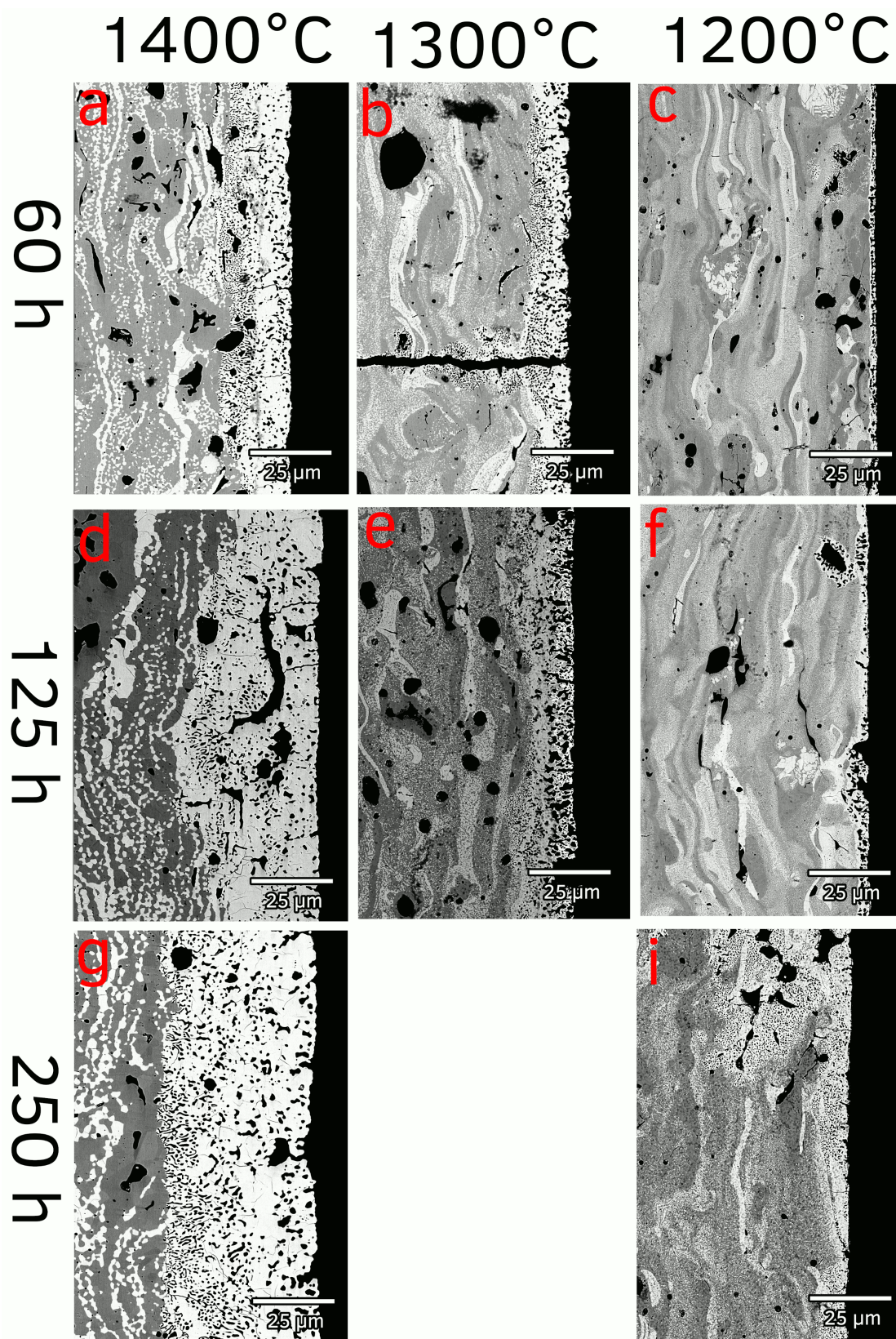


Figure 3.36: Backscattered electron images showing representative cross-sections on APS $\text{Yb}_2\text{Si}_2\text{O}_7$ coatings exposed at 1200, 1300, and 1400°C for 60, 125, and 250h with v_g between 150 and 200 m/s represented here. The steam-exposed surface is on the right side of all images.

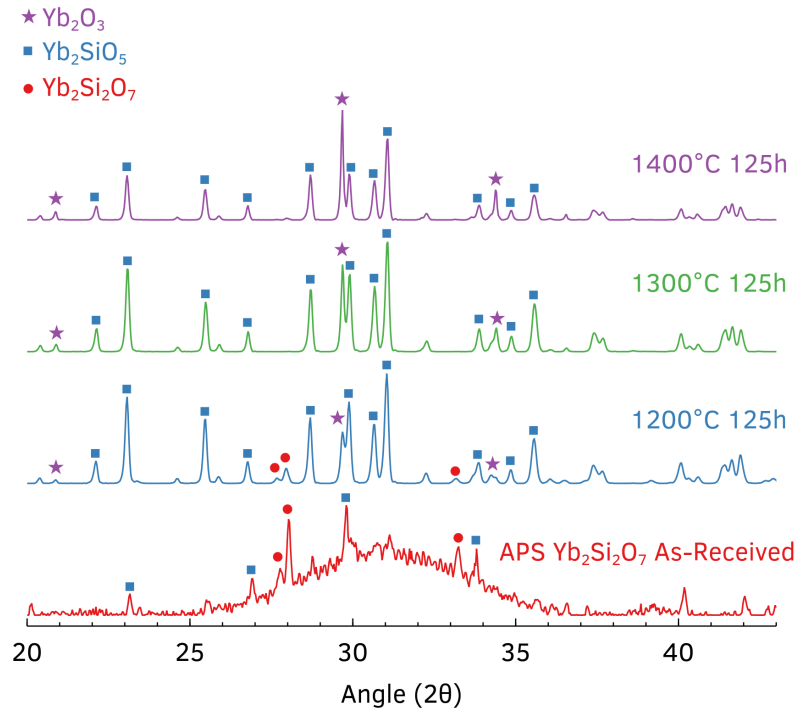


Figure 3.37: XRD results for APS Yb₂Si₂O₇ as-received as well as after exposure in the steam-jet furnace for 125h at 1200, 1300, and 1400°C. After exposure in the steam-jet furnace the dominant phase present is Yb₂SiO₅ at all temperatures. Yb₂O₃ becomes more abundant with increasing temperature.

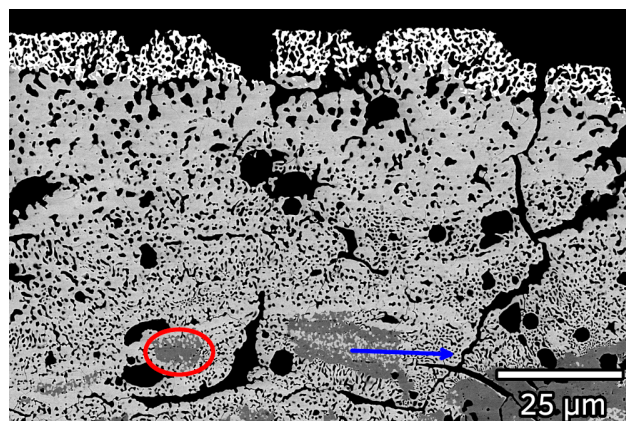


Figure 3.38: A backscattered electron image showing the complex microstructure of the depletion layer that results from local cracks, blue arrow, and pores found in a dense APS Yb₂Si₂O₇ coatings exposed in the steam-jet furnace at 1400°C for 125h with an approximate surface gas velocity of 190 m/s. The red circle denotes an area of unreacted coated surrounded by Yb₂SiO₅ formed from several reaction fronts due to these local microstructures.

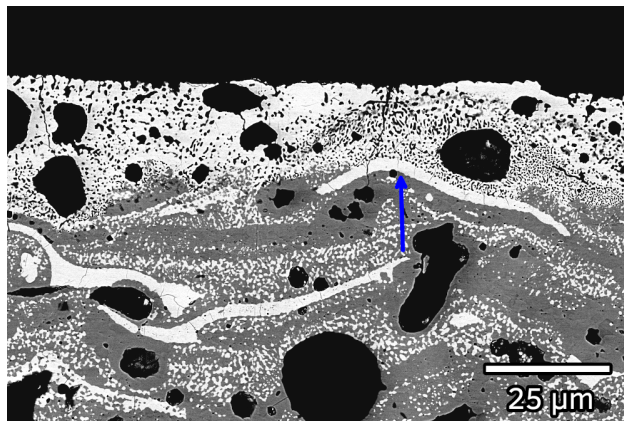


Figure 3.39: A backscattered electron image showing an example of an SiO₂-poor splat, blue arrow, from the initial processing of the APS coating arresting progress of the depletion layer in a dense APS Yb₂Si₂O₇ coatings exposed in the steam-jet furnace at 1300°C for 125h with a surface gas velocity of approximately 150 m/s.

Porous APS $\text{Yb}_2\text{Si}_2\text{O}_7$ Coatings Provided by Rolls-Royce

A second set of intentionally porous APS $\text{Yb}_2\text{Si}_2\text{O}_7$ coatings sprayed on monolithic SiC substrates were received from Rolls-Royce. The composition of these coatings was similar to the dense APS coatings shown in Figures 3.31 and 3.32 when received. Non-equilibrium phases were present, along with a complex splat structure. However, Figure 3.40 shows the plan view of one of the porous coatings after initial bake out. Multiple large pores can be observed on the surface.

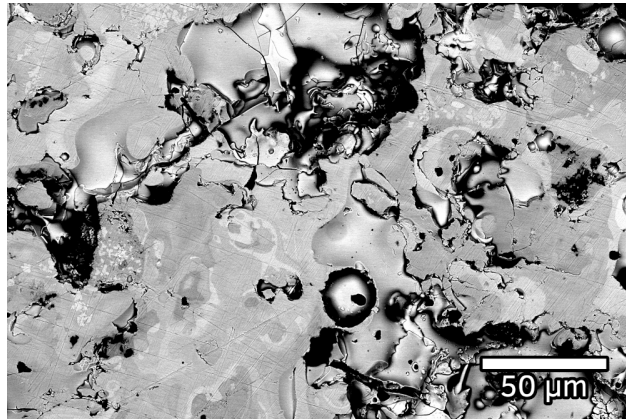


Figure 3.40: A backscattered electron image showing the polished morphology in plan view of porous APS $\text{Yb}_2\text{Si}_2\text{O}_7$ coatings provided by Rolls-Royce.

These porous APS $\text{Yb}_2\text{Si}_2\text{O}_7$ coatings were exposed at 1200, 1300, and 1400°C for 60, 125, and 250h in the steam-jet. Maximum gas velocities range between 230-250 m/s. A montage of both plan view and cross-sectional images taken of these samples are shown in Figures 3.41 and 3.42. The plan view images look similar to those found in the dense APS coatings. The major difference between the porous and dense APS coatings can be seen in cross-section. While the same trend of increasing depletion thickness and more coarsened pores with increasing time and temperature is observed, the porous APS coatings allow for SiO_2 depletion much deeper into the coating. The local depth of SiO_2 depletion increases due to the increase in porosity. The large pores allow for SiO_2 depletion around the edges of the pores as water vapor can reach deeper into the coating, similar to the effect seen in Figures 3.38 and 3.39. These pores also act as fast diffusion pathways such as in Figure 3.42 (i) where the overall depletion depth is much greater below the large pore on the right of the figure than on the left.

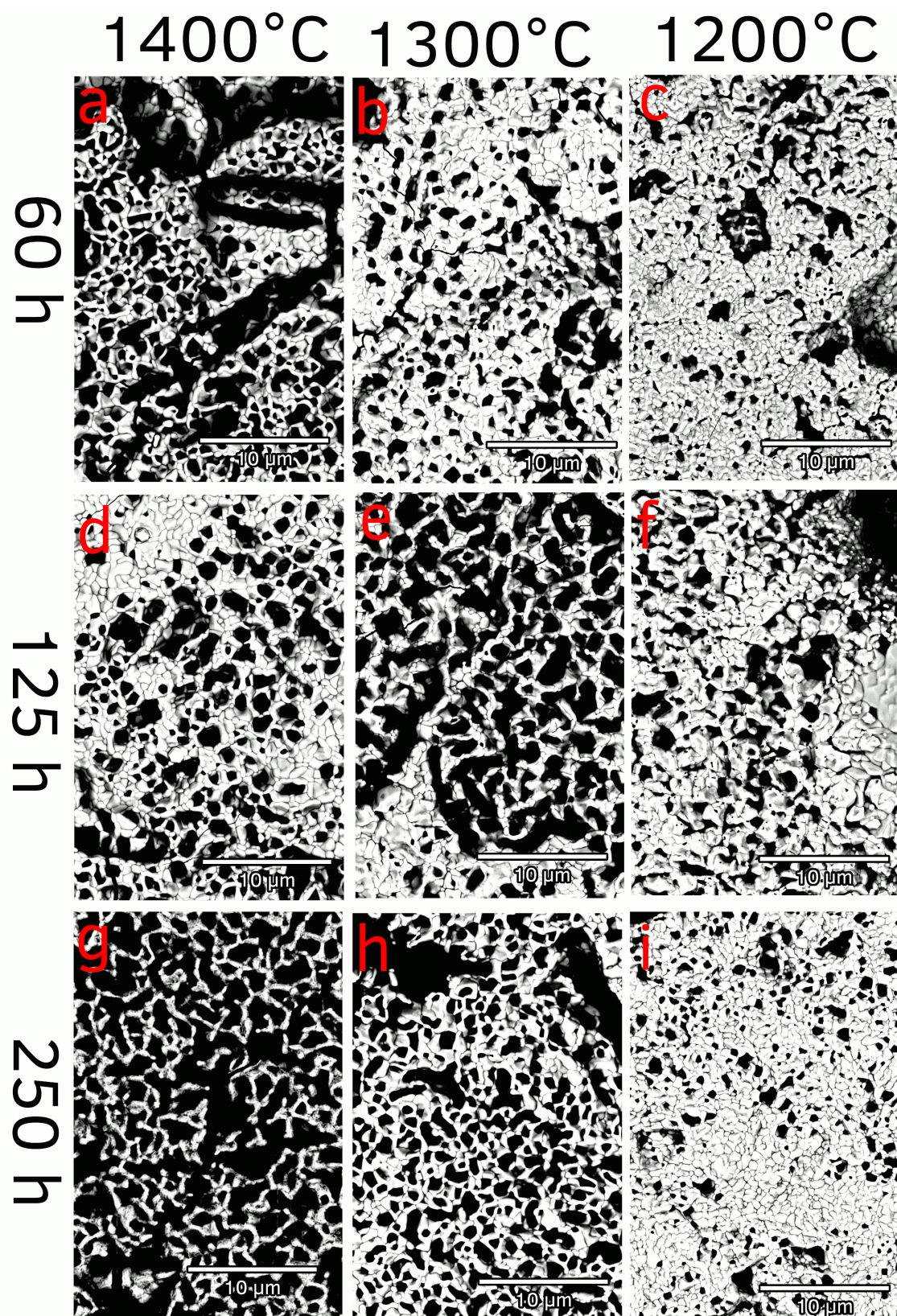


Figure 3.41: A collection of backscattered electron images showing the surface morphology of 1 mm downstream of the impingement site on porous APS $\text{Yb}_2\text{Si}_2\text{O}_7$ coatings exposed at 1200 ($v_g = 175$ m/s), 1300 ($v_g = 185$ m/s, and 1400°C ($v_g = 195$ m/s) for 60, 125, and 250h.

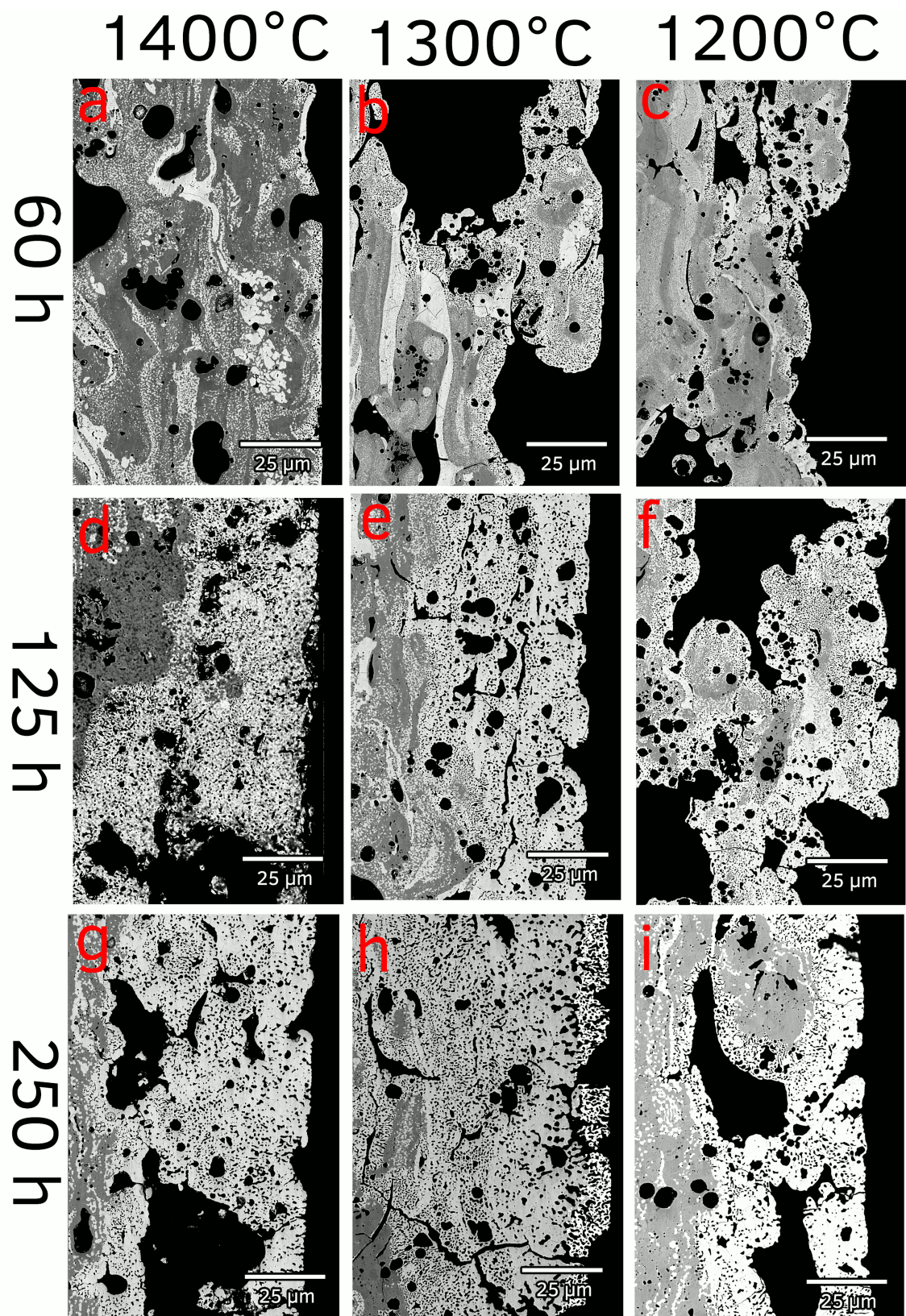


Figure 3.42: A collection of backscattered electron images showing the cross-sectional morphology on porous APS $\text{Yb}_2\text{Si}_2\text{O}_7$ coatings exposed at 1200, 1300, and 1400°C for 60, 125, and 250h with v_g between 150 and 200 m/s represented here. The steam-exposed surface is on the right side of all images.

3.4 Discussion

3.4.1 SiO₂ Volatility

The experimental and calculated results for SiO₂ volatility are shown in Table 3.5. This table is the same as Table 3.2 and is repeated here for convenience. Experimental results show a minimum, the smooth profile, and maximum, the deep pit, SiO₂ recession of 350 μm and 525 μm respectively after exposure in the steam-jet furnace at 1400°C for 60 h. Using the flux equation given by Equations 3.1 and 3.2 a SiO₂ recession rate of 6.39 μm/h is calculated using a maximum gas velocity of 250 m/s, predicting a total recession of 383.4 μm over a 60 h test. This calculated value is in good agreement with the minimum recession assumed as a smooth profile for both 8 and 60h exposures.

The H₂O(g) flow is assumed laminar. The equation for the Reynolds number is given in Equation 3.3, with calculations for the experimental conditions giving a Reynold's number of 7150. This value is much lower than the laminar-turbulent transition for a flat plate geometry ($5 \cdot 10^5$), suggesting the laminar flow hypothesis is reasonable. This theory has previously been applied successfully to predict volatilization behavior of SiO₂, Cr₂O₃, and Al₂O₃. [2] [58] [50].

$$Re_L = \frac{\rho'vL}{\eta} \quad (3.3)$$

The 1400°C testing temperature is about 300°C below the melting point of SiO₂, 1723°C. It is therefore possible that the temperature is high enough that high velocity steam-jet could shear the viscous SiO₂. The area directly surrounding the impingement site is higher than the base material in Figure 3.4. It should also be noted that the small areas not detected in the optical profilometry, many of which show up in Figure 3.7, could be pits forming from PtRh debris or liquid H₂O(g) droplets ejected from the capillary. Pits show up more frequently near the SiO₂ impingement site, corresponding with higher velocity regions. These features are not observed in the Y₂O₃, Y₂SiO₅, or Y₂Si₂O₇ samples suggesting that the hardness of the test specimen plays a role in resisting erosion.

Table 3.5: Bounded experimental recession rate results of SiO₂ exposures to H₂O(g) at 1400°C and a maximum gas velocity of 250 m/s compared to calculation. Reproduced here for convenience.

	Recession (μm)		Recession Rate (μm/h)		Calculated rate from Equations 3.1 and 3.2
	8h	60h	8h	60h	
min	50	350	6.25	5.83	6.39
max	75	525	8.75	9.38	

3.4.2 Time Dependence of the Reaction Between $\text{H}_2\text{O}(\text{g})$ and $\text{Y}_2\text{Si}_2\text{O}_7$

The porous Y_2SiO_5 layer found on the dense, phase pure $\text{Y}_2\text{Si}_2\text{O}_7$ samples after exposure at 1400°C for 60, 125, and 250h show a coarsening of the pore structure with increased time. The elongated pores perpendicular to the interface between Y_2SiO_5 and $\text{Y}_2\text{Si}_2\text{O}_7$ grow longer with time, but do not change their shape at 125h, while at 250h the pores at this interface are more equiaxed.

The SiO_2 depletion depth data follow a linear fit when plotted against $t^{1/2}$, demonstrates parabolic kinetics and a diffusion controlled reaction between $\text{H}_2\text{O}(\text{g})$ and $\text{Y}_2\text{Si}_2\text{O}_7$. These results are in agreement with previous results by Golden that showed parabolic kinetics for SiO_2 depletion from $\text{Y}_2\text{Si}_2\text{O}_7$ at 1200°C in the steam-jet furnace using a fused quartz capillary [12]. The diffusion of either $\text{H}_2\text{O}(\text{g})$ in or $\text{Si}(\text{OH})_4(\text{g})$ out of the porous layer is the most likely candidate for the process that is controlling the rate of reaction. Because the surface of the $\text{Y}_2\text{Si}_2\text{O}_7$ surface is exposed to 1 atm $\text{H}_2\text{O}(\text{g})$ an excess of reactant throughout the experiment makes $\text{Si}(\text{OH})_4(\text{g})$ product diffusion out of the system most likely to be controlling.

3.4.3 Temperature Dependence of the Reaction Between $\text{H}_2\text{O}(\text{g})$ and $\text{Y}_2\text{Si}_2\text{O}_7$

The data presented in Figure 3.28 show an exponential relation between SiO_2 depletion depth and temperature. Because parabolic kinetics are observed, the $\ln(\text{depletion depth})^2/\text{time}$ at 60h for 1200, 1300, and 1400°C is plotted against inverse temperature, shown in Figure 3.29, with the calculated $E_a = 382$ kJ/mol.

The SiO_2 depletion measurements gathered for the phase pure $\text{Y}_2\text{Si}_2\text{O}_7$ sample exposed at 1400°C for 125h is plotted alongside depletion measurements made by Golden on phase pure $\text{Y}_2\text{Si}_2\text{O}_7$ samples exposed in the steam-jet using a fused quartz capillary at 1000, 1100, and 1200°C for 125h, shown in Figure 3.43 [12]. The exponential relation between SiO_2 depletion depth and temperature is even more obvious in this plot, with a sharp increase between 1200 and 1400°C . The natural logarithm of these rates are then plotted against inverse temperature and shown in Figure 3.44 alongside the data from this study collected on phase pure $\text{Y}_2\text{Si}_2\text{O}_7$ exposed in the steam-jet furnace at 1200- 1400°C for 60h. The plot shows that a change in mechanism is likely between 1000 and 1100°C . The activation energy calculated from the data for 1100, 1200, and 1400°C 125h is 461 kJ/mol, higher the activation energy for data at 60h of 382 kJ/mol. The activation energy of the reaction between $\text{Y}_2\text{Si}_2\text{O}_7$ and $\text{H}_2\text{O}(\text{g})$ is about 6 times higher than the activation energy of the reaction between SiO_2 and $\text{H}_2\text{O}(\text{g})$, approximately 60 kJ/mol.

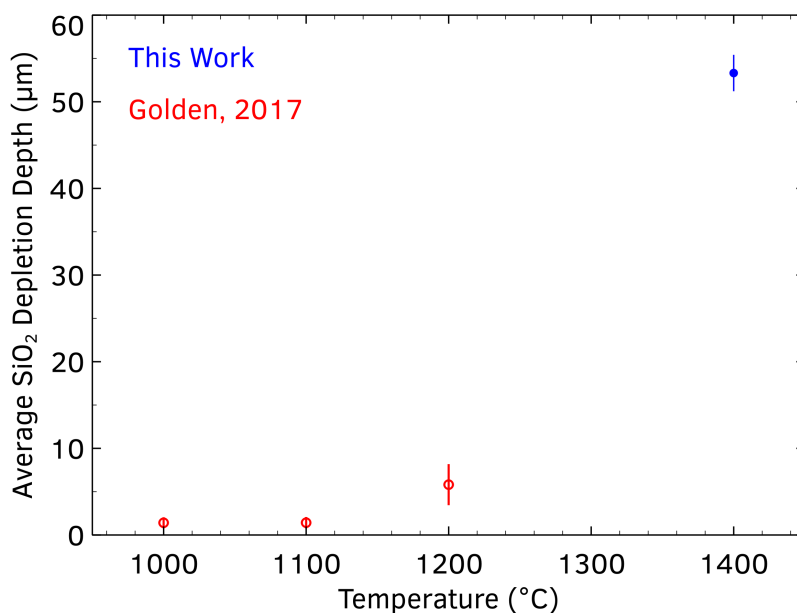


Figure 3.43: Average SiO₂ depletion depth vs. temperature for phase pure Y₂Si₂O₇ exposed at 1000, 1100, 1200, and 1400°C for 125h.

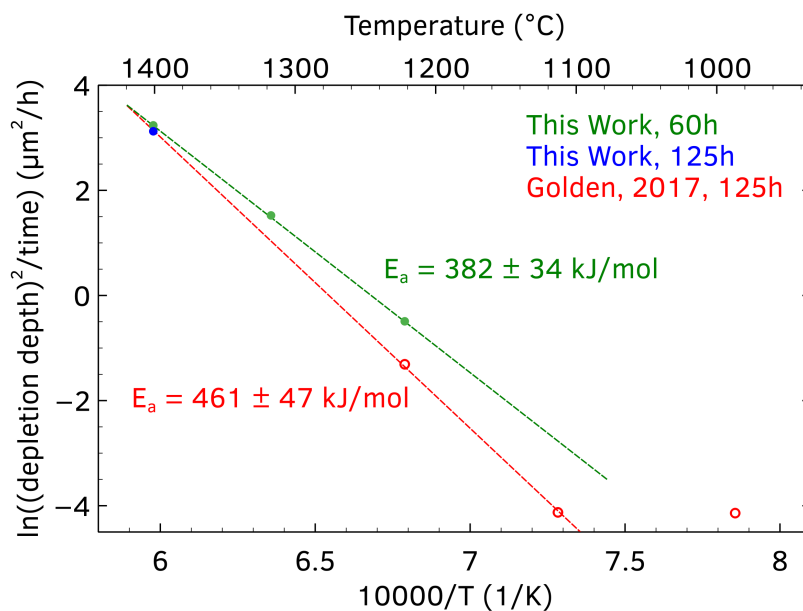


Figure 3.44: The natural log of (depletion rate)² plotted against inverse temperature for phase pure Y₂Si₂O₇ exposed in the steam-jet furnace at 1000 - 1400°C for 60 and 125h. The activation energy for depletion at 125h is higher, 461 ± 47 kJ/mol within a 95% confidence interval, compared to at 60h, 382 ± 34 kJ/mol. This suggests that the activation energy of the reaction between Y₂Si₂O₇ and H₂O(g) increases with time. The depletion mechanism seems to change between 1000 and 1100°C, as there is a discontinuity in the data at 1100°C.

3.4.4 Effect of Velocity on SiO₂ Volatility in Disilicates

In this study, variation in microstructure of porous Y₂SiO₅ formed from Y₂Si₂O₇ was observed as a function of velocity, with the formation of a dense Y₂SiO₅ layer at higher velocities. The transition point between a completely porous Y₂SiO₅ layer and the formation of the dense Y₂SiO₅ layer occurs at a $v_g \approx 170$ m/s. At lower velocities the Y₂SiO₅ layer is porous. The kinetics of the formation of this porous Y₂SiO₅ layer were discussed earlier [59]. Increasing velocity above ~ 170 m/s reduces the total thickness of the Y₂SiO₅ layer, with the dense Y₂SiO₅ layer accounting for a larger percentage of the overall Y₂SiO₅ thickness. This decrease in overall layer thickness can be attributed to densification of the Y₂SiO₅ layer both within and outside the impingement area, as well as erosion occurring in the impingement site. Erosion can occur at the highest velocities due to impingement of particles on the porous structure of the Y₂SiO₅ and the degraded structural integrity. The densification of Y₂SiO₅ acts as a barrier to further ingress of H₂O(g), slowing the formation of further porous Y₂SiO₅ thereby also limiting erosion. Possible mechanisms for formation of the dense Y₂SiO₅ layer are described in Section 3.4.5.

In both Y₂Si₂O₇ and Y₂SiO₅ samples, the formation of Y₂O₃ on the surface of Y₂SiO₅ was observed at velocities >175 m/s. However, the surfaces of the two samples are different, despite the presence of Y₂O₃ on both. Thicker formations of Y₂O₃ were observed on the surface of Y₂SiO₅ samples as compared to Y₂Si₂O₇ samples, attributed to the presence of Y₂SiO₅ from the beginning of the test. The Y₂Si₂O₇ sample surface is dominated by the formation of Y₂SiO₅ with trace amounts of Y₂O₃ overall, seen in Figures 3.12 and 3.13, while the Y₂SiO₅ sample showed less surface modification from the thin layer of Y₂O₃ that formed, shown in Figure 3.18. Additionally, the equilibrium partial pressure of Si(OH)₄(g) at 1400°C for Y₂SiO₅ reacting with H₂O(g) (Reaction 3) is $9.8 \cdot 10^{-9}$ atm (calculated based on the activity of SiO₂ in the Y₂O₃-Y₂SiO₅ phase field) compared to $1.8 \cdot 10^{-6}$ atm for Y₂Si₂O₇ reacting with H₂O(g) (calculated using Factsage and data from Fabrichnaya, et al.) (Reaction 2) [53] [10] [54]. The Si(OH)₄(g) that diffuses outward from the reaction interface to the surface of the sample in Y₂Si₂O₇ exposures could suppress the further loss of SiO₂ from Y₂SiO₅ to form Y₂O₃. The formation of the dense layer of Y₂SiO₅ at higher velocities in the Y₂Si₂O₇ tests then likely plays a role in the formation of Y₂O₃ on these samples by lowering the local partial pressure of Si(OH)₄(g).

The overall reaction depths in both Y₂Si₂O₇ and Y₂SiO₅ are several times lower than the recession found in SiO₂ samples exposed in H₂O(g) for the same time. The reduced activity of SiO₂ at 1650°C in the Y₂Si₂O₇ + Y₂SiO₅ phase field (0.28) and Y₂SiO₅ + Y₂O₃ phase field ($1.5 \cdot 10^{-3}$) [8] reduces the equilibrium partial pressure of Si(OH)₄(g) and the corresponding flux as given by Equation 3.1. Therefore, a Y₂Si₂O₇ EBC allows for selective removal of SiO₂ from the coating system at rates slower than pure SiO₂. As SiO₂ is

lost from the $Y_2Si_2O_7$, Y_2SiO_5 then Y_2O_3 are observed, consistent with the equilibrium Y_2O_3 - SiO_2 phase diagram.

3.4.5 Possible Mechanisms for the Formation of Dense Monosilicate Layers

At $H_2O(g)$ velocities approaching 200 m/s the monosilicate layer that forms from reaction between the initial disilicate and water vapor begins to exhibit a dense structure, as compared to the structure with $\sim 25\%$ porosity observed at lower velocities. This feature is best seen in Figure 3.30 which shows the progression of the Y_2SiO_5 microstructure formed from $Y_2Si_2O_7$ with increasing velocity. The center image shows a sharp divide between the porous and dense microstructures. This same phenomenon is observed in APS coatings as well, though the initial microstructure of those coatings makes it difficult to see such a sharp divide. The mechanism for this densification is still not clear from current observations. Several hypotheses for the formation of this dense layer are presented next.

The most straightforward explanation of this densification is that the monosilicate sinters over time. The monosilicate at the specimen surface formed from the reaction between disilicate and water vapor first, so this material would sinter all through the testing time. There are several arguments against this hypothesis. Densification through sintering is a function of temperature, not velocity. However, as seen in Figure 3.30, the microstructure changes dramatically within the same cross section on the same sample, with the only variable being a change in velocity. In fact, the areas exposed to a higher velocity of H_2O are likely cooler than the areas of low velocity as they undergo convective cooling. A temperature difference of $30^\circ C$ is expected moving from areas exposed to velocities of 150 m/s relative to those at 200 m/s. This was determined from furnace temperature calibration where the thermocouple is manually manipulated into place and movements of 1-5 mm from the outlet of the capillary result in temperature drops of 30 - $50^\circ C$. However a lower temperature exists in the higher velocity areas where the densification is observed. This rules out temperature dependant sintering as the explanation for dense RE_2SiO_5 formation.

The second hypothesis for densification of the monosilicate layer is that the rare earth oxide formed on the surface of the porous monosilicate structure reacts with $Si(OH)_4(g)$ diffusing outward from the $RE_2Si_2O_7/RE_2SiO_5$ interface to form monosilicate again. The reaction of monosilicate with $H_2O(g)$ to form rare earth oxide was observed for the SPS Y_2SiO_5 tested in the steam-jet at velocities approaching 200 m/s. When phase pure Y_2O_3 was exposed in the steam-jet the area outside of the highest velocity areas reacted with contaminant $Si(OH)_4(g)$ to form Y_2SiO_5 , suggesting this reaction is possible. The diffusion of $Si(OH)_4(g)$ outward from the reaction interface between disilicate/monosilicate through the pores in the monosilicate/rare earth oxide would enable RE_2O_3 to react with $Si(OH)_4(g)$ to form monosilicate, filling in

the pore structure and densifying the system. An argument against this hypothesis is that the reaction of porous $\text{RE}_2\text{O}_3 + \text{Si}(\text{OH})_4(\text{g})$ to form RE_2SiO_5 fills only about half the pore volume based on the change in molar volume change of the reaction.

A third hypothesis combines the previous one but adds the diffusion of rare earth ions to fill the excess pore volume. Recent research showed that in oxygen or water vapor activity gradients across dense rare earth silicates, rare earth ions diffuse toward the higher oxidant activity, resulting in SiO_2 formations on the low oxidant activity side [60]. The $\text{RE}_2\text{Si}_2\text{O}_7$ surface is exposed directly in the steam-jet to a total pressure of 1 atm of $\text{H}_2\text{O}(\text{g})$. In a dense coating system the activity of the oxidant will decrease across the thickness of the coating from the gas phase to the underlying thermally grown oxide. This gradient across the thickness of the coating would drive rare earth ions to diffuse toward the $\text{RE}_2\text{Si}_2\text{O}_7$ surface exposed to the steam-jet. These RE ions would oxidize immediately to form rare earth oxide. This oxide would then react readily with $\text{Si}(\text{OH})_4(\text{g})$ diffusing outward from the reaction interface to form monosilicate. This would fill in pores with added mass through the diffusion of rare earth ions. This hypothesis addresses the required volume change, but a gradient in $\text{H}_2\text{O}(\text{g})$ partial pressure across free standing $\text{RE}_2\text{Si}_2\text{O}_7$ is not present in steam-jet tests. Furthermore, solid state diffusion of RE ions is slow relative to $\text{Si}(\text{OH})_4(\text{g})$ transport through the porous Y_2SiO_5 . A fourth related hypothesis is that a chemical potential gradient of RE oxide exists from the steam-facing surface to the $\text{RE}_2\text{Si}_2\text{O}_7$ substrate driving transport of RE ions toward the reaction interface. The excess RE oxides react with outward diffusing $\text{Si}(\text{OH})_4(\text{g})$ to form RE_2SiO_5 . This hypothesis suffers from the same limitation, in that solid state diffusion of RE ions is slow relative to gas phase transport. However, surface diffusion of RE-containing species might be sufficiently rapid for this mechanism to occur.

3.4.6 Stability of Y_2O_3

Previous reports by Courcot et al. [38] [61] of reaction of Y_2O_3 with high-temperature $\text{H}_2\text{O}(\text{g})$ to form $\text{YOOH}(\text{g})$ and $\text{Y}(\text{OH})_3(\text{g})$ would suggest a Y_2O_3 recession mechanism similar to SiO_2 in the steam-jet. However, no recession of Y_2O_3 was observed. Faceting occurs in the presence of the high-velocity $\text{H}_2\text{O}(\text{g})$ forming low surface energy orientations, but profilometry showed no loss of material. The stability of Y_2O_3 in high-temperature water vapor is confirmed. These findings are supported by the presence of Y_2O_3 as a product found on the surface of both $\text{Y}_2\text{Si}_2\text{O}_7$ and Y_2SiO_5 steam-jet exposures.

Faceting on the surface of the Y_2O_3 is attributed to enhanced surface diffusion in the presence of $\text{H}_2\text{O}(\text{g})$. This same effect has been observed previously by Opila and Myers in Al_2O_3 exposed to low velocity mixtures of oxygen and water vapor [50]. The enhanced surface diffusion allows for the rearrangement of grains on the surface to the lowest energy orientation. This is not indicative of a volatilization reaction occurring, as optical

profilometry shows no recession. While optical profilometry shows a slight curvature in the measurement across the impingement site, it should be noted that the measured range is only 2 μm across 5.5 mm of the coupon surface, which is within the error of the measurement.

The formation of Y_2SiO_5 on the surface of the Y_2O_3 sample at $\text{H}_2\text{O}(\text{g})$ velocities below 150 m/s is due to the presence of contaminant $\text{Si}(\text{OH})_4(\text{g})$ in the furnace. As noted in Section 3.4.4, the equilibrium partial pressure of $\text{Si}(\text{OH})_4(\text{g})$ for Y_2SiO_5 is $9.8 \cdot 10^{-9}$, with a ΔG_{rxn}° calculated in Factsage at 1400°C of -317 kJ [53][10][54], suggesting even low levels of SiO_2 impurities can result in Y_2SiO_5 formation from Y_2O_3 . In high velocity regions, $\text{H}_2\text{O}(\text{g})$ limits the transport of $\text{Si}(\text{OH})_4(\text{g})$ contamination.

3.4.7 Air Plasma Sprayed $\text{Yb}_2\text{Si}_2\text{O}_7$ Microstructure and Kinetics of SiO_2 Depletion

The fundamental SiO_2 depletion mechanisms at work in Section 3.4.4 do not change when moving from SPS $\text{Y}_2\text{Si}_2\text{O}_7$ to the $\text{Yb}_2\text{Si}_2\text{O}_7$ APS system. The APS processing introduces splats, cracks, and extra pores into the starting material. As seen in Figure 3.38, the extent and location of the depletion layer follows the presence of cracks and pores that were present in the starting material. This is in contrast to Figure 3.12, which shows a uniform depletion layer thickness in a dense, phase pure $\text{Y}_2\text{Si}_2\text{O}_7$ sample. While cracks and pores can be present in material processed by SPS, their existence is more common in APS. These cracks and pores act as fast diffusion pathways both for $\text{H}_2\text{O}(\text{g})$ into and $\text{Si}(\text{OH})_4(\text{g})$ out of the porous Y_2SiO_5 . Large pores, especially, act as areas of fast gas exchange. These large pores, in contrast to the small open pore network created from the formation of Yb_2SiO_5 , allow for direct diffusion outward to the surface of the coating.

Cracks and pores also leave the material more vulnerable to mechanical erosion than a dense material. Cracks can open further during thermal cycling, allowing for deeper access for SiO_2 depletion. A high density of pores in the coating results in ligaments that are weaker than dense material. This weakness is showcased in the impingement site overview shown in Figure 3.34 where a large amount of material has been eroded. While this is partly due to the $\sim 25\%$ porosity that forms on the reaction between $\text{H}_2\text{O}(\text{g})$ and $\text{Yb}_2\text{Si}_2\text{O}_7$, the underlying structure of the material adds additional weakness. The $\text{Yb}_2\text{Si}_2\text{O}_7$ material lost during testing, whether to SiO_2 depletion or mechanical degradation, is highest in the impingement area.

In contrast, the Yb_2SiO_5 splats slow the depletion front. These splats are SiO_2 -poor, and so act as barriers to SiO_2 depletion. The reaction front moves laterally around the splats increasing the diffusion distance of $\text{Si}(\text{OH})_4$ out of the coating around the splats, slowing the process.

The evolution of the splat microstructure with time and temperature causes these splats to be less protective. As seen in Figure 3.36 comparing micrographs obtained after exposure at 1200°C 60h to 1400°C 250h the splat structure equilibrates towards more monosilicate and less non-equilibrium phases. As the splats equilibrate they break up into more equiaxed grains, rather than staying as elongated splats. This follows from minimization of energy decreasing the surface area to volume ratio of the grains due to Rayleigh instability, observed previously in thin films and bulk alumina [62] [63]. Over time, this causes these grains to be less protective to the advance of depletion. As the splat breaks up, rendering less protection to the advance of the depletion front, attack between grains is observed.

Densification of the Yb_2SiO_5 layer that forms from reaction between $\text{Yb}_2\text{Si}_2\text{O}_7$ and H_2O occurs in the APS coatings as well. These dense layers are not as delineated as that seen in Figure 3.30, and contain larger pores. These pores may exist in the starting material. It is also possible that pores coalesce into larger pores. The densification of the Yb_2SiO_5 layer does still allow for the formation of Yb_2O_3 .

In summary, the microstructure of APS coatings provides two differences relative to SPS material: cracks and pores present in the microstructure allow for deeper SiO_2 depletion and material loss, while SiO_2 -poor splats allow for slowing of the depletion front. These two effects compete with one another. Creating a dense coating with many low- SiO_2 content splats near the surface of the coating would result in a lower average depletion than dense SPS material. However, as seen in Chapter 2, such a structure would result in mismatches in the thermal expansion between $\text{RE}_2\text{Si}_2\text{O}_7$ and RE_2SiO_5 in the coating. These mismatches would impact processing as well as in testing and use. Making a dense APS coating with variable phases and chemistry would require microstructural optimization to minimize SiO_2 depletion.

3.5 Conclusions

SiO_2 volatilizes readily in high-temperature, high-velocity water vapor, with a smooth recession profile except for large pits (presumably mechanical damage) that form at the highest velocities. Recession rates observed with a maximum gas velocity of 250 m/s are in good agreement with predictions based on laminar gas boundary layer theory. $\text{Y}_2\text{Si}_2\text{O}_7$ exhibited SiO_2 volatility forming a porous Y_2SiO_5 layer at velocities <170 m/s. A dense Y_2SiO_5 layer formed on $\text{Y}_2\text{Si}_2\text{O}_7$ at higher velocities with the further loss of SiO_2 to form surface Y_2O_3 . Y_2SiO_5 samples also lost SiO_2 through volatilization to form Y_2O_3 . Y_2O_3 showed no evidence of volatilization in the presence of high-temperature, high-velocity water vapor, instead faceting to low-energy surfaces. The Y_2O_3 -containing line compounds of the $\text{Y}_2\text{O}_3 - \text{SiO}_2$ system show progressively more stability with the decrease in SiO_2 content. This increasing stability with SiO_2 loss bodes well for

$\text{Y}_2\text{Si}_2\text{O}_7$ use as an EBC as its reaction products with steam are more stable, protecting it from further volatilization.

Several hypotheses were presented for how Y_2SiO_5 densifies in the steam-jet. Two activity gradient hypotheses are the most complete in their explanation of the densification. This activity gradient theory requires solid state, grain boundary, or surface diffusion of RE ions in order to fill the pores that typically form from the reaction of $\text{RE}_2\text{Si}_2\text{O}_7$ with $\text{H}_2\text{O}(\text{g})$.

Silica depletion behavior in APS $\text{Yb}_2\text{Si}_2\text{O}_7$ coatings varied depending on the local microstructure. Pores and cracks increased SiO_2 depletion locally while SiO_2 -poor splats provided barriers to further depletion. The relative importance of these effects changes with time and temperature. The splats break into smaller grains with increasing time and temperature, however, so their depletion barrier capability decreases with increased exposure time and temperature. Porous APS coatings showed deeper depletion of SiO_2 compared to dense coatings.

3.6 Recommendations for Future Work

Further temperature dependence measurements must be made to determine the rate limiting step for the depletion of SiO_2 from $\text{RE}_2\text{Si}_2\text{O}_7$ systems. Current hypotheses suggest that diffusion of $\text{Si}(\text{OH})_4(\text{g})$ out of the system is the rate limiting step, but this has not been confirmed.

The fundamental questions left unanswered include determination of the mechanism causing the densification of monosilicate during steam-jet exposure. It is not clear what role gas velocity plays in this process. Characterization of the dense monosilicate layer may elucidate how it is formed. Determining why dense monosilicates form slowly in moderate velocities while forming directly on the disilicate interface at high velocities would contribute to mechanistic understanding.

It is uncertain whether the heterogeneous microstructure of APS coatings is beneficial to coating life compared to phase pure materials. SiO_2 -poor splats (e.g. RE_2SiO_5) act as barriers which slow depletion, but present thermomechanical challenges due to CTE mismatch with the substrate. Cracks and pores increase SiO_2 -depletion rates as they allow for deeper diffusion of $\text{H}_2\text{O}(\text{g})$ into the coating and fast pathways of diffusion for $\text{Si}(\text{OH})_4(\text{g})$ out. It is unclear whether SiO_2 -poor splats, pores, or cracks dominate over longer periods of time. It is also not clear that these effects will impact overall coating life. Maximum testing times have been limited to 250h. Longer testing is needed to determine if these effects impact material life when compared to phase pure materials.

New processing paths with APS should be explored, taking advantage of the ability of the splats to slow depletion. Graded compositions, where the SiO_2 content of the coating decreases moving from substrate

to surface in a controlled gradient should be explored to test the resilience of these low-SiO₂ phases in a heterogeneous microstructure.

Chapter 4

Lifetime Modeling of EBC Thermochemical Stability in High-Temperature, High-Velocity Water Vapor

4.1 Objectives

The objective of this research is to develop a computational model for SiO_2 depletion from $\text{RE}_2\text{Si}_2\text{O}_7$ that captures experimental observations and allows for predictive capability. Necessary components of the model are: 1. the reaction of $\text{RE}_2\text{Si}_2\text{O}_7$ with $\text{H}_2\text{O}(\text{g})$ to form RE_2SiO_5 and $\text{Si}(\text{OH})_4(\text{g})$; 2. microstructural evolution through coarsening of grains and the pore structure; 3. gas transport of $\text{H}_2\text{O}(\text{g})$ inward through a gas boundary layer and porous reaction product; 4. gas transport of $\text{Si}(\text{OH})_4(\text{g})$ outward through the porous reaction product and gas boundary layer; 5. variations of kinetics with respect to temperature, pressure, velocity, and the thermodynamics of reactions in the system.

A computational model of SiO_2 depletion from rare earth silicate systems is needed to predict thermochemical lifetimes. Lifetime prediction has been constrained by test time and the characterization techniques available in the laboratory. This work outlines the first computational model of selective removal of SiO_2 from the rare earth silicate materials encountered in high-temperature, high-velocity water vapor environments. This computational model encapsulates the complex microstructural, kinetic, and thermodynamic

processes that arise in this material system as SiO_2 is selectively removed from rare earth silicates as observed experimentally in the previous chapter. The removal of SiO_2 from $\text{RE}_2\text{Si}_2\text{O}_7$ to form RE_2SiO_5 and porosity are the basic phenomena captured in this model. These pores also evolve over time through coarsening and coalescence. The diffusion of $\text{Si}(\text{OH})_4(\text{g})$ out of the system through the pore structure that forms is simulated in this computation model. The partial pressure of $\text{Si}(\text{OH})_4(\text{g})$ in each cell is also a control for the reaction of $\text{RE}_2\text{Si}_2\text{O}_7$ and RE_2SiO_5 with $\text{H}_2\text{O}(\text{g})$, based on thermodynamic values calculated and present in the previous chapter. All of this information is then tied to physical time and length scales through comparison with experimental results. Once these connections have been made the model can be run for increasingly long periods of time to allow for testing of the system at timescales not possible in the laboratory. This allows for prediction of the microstructural development and SiO_2 depletion kinetics in time regimes well outside of experimental reach.

4.2 Methods

A computational model using the Stochastic Parallel PARTicle Kinetic Simulator (SPPARKS) framework, developed at Sandia National Laboratories, is used as the basis for this EBC life prediction effort [64]. The SPPARKS framework uses Monte Carlo methods and partial differential equation (PDE) solvers to model phenomena at various scales of length and time.

The grain coarsening, surface diffusion, and reaction portions of the model were handled by a Potts model. This Potts model used the rejection Kinetic Monte Carlo (rKMC) method to simulate time in the system by examining events and determining if they are successful or not based on a set of rules aimed at energy minimization. In this framework one unit of energy is added to the simulation every time neighboring sites have unlike states. For example in Figure 4.1 each color represents the different states in an example system. States in this case represent either different chemical phases or grain orientations. The green hashed cell boxed in bold black is being considered for coarsening neighboring grains. In this system the energy state of the green hashed cell is 5 because this cell has five neighbors of unlike states, 4 red and 1 orange. There are then three possible outcomes for this cell: (i) Switch state to red, coarsening the red grain, decreasing the energy of the site to 4, (ii) Switch state to orange, coarsening the orange grain, increasing the energy of the site to 7, (iii) Stay green, rejecting any event from occurring, keeping the energy of the site at 5. From this example it can be seen that the state of the site would change to red, the lowest energy scenario, coarsening the red grain and reducing the energy of the system

Surface diffusion of solid material was considered on the gas sites only. This surface diffusion allows for coarsening of the pore structure. Figure 4.2 shows a scenario that could occur when surface diffusion is

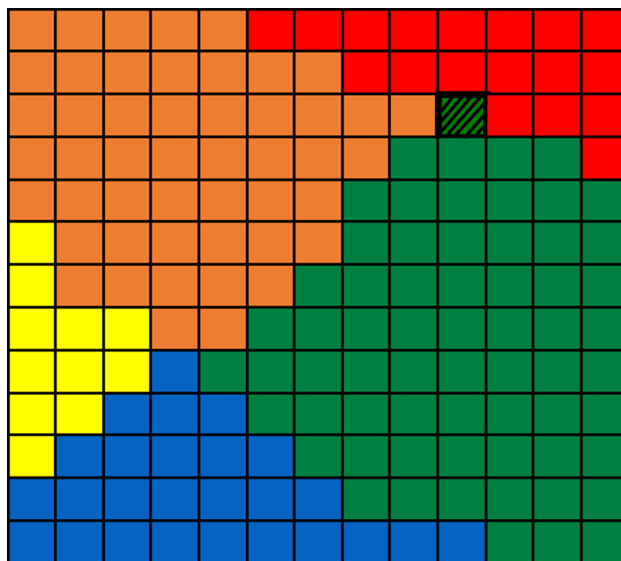


Figure 4.1: A simplified example in 2D of neighboring grains interacting and possibly coarsening. The green hashed cell in bolded black is the cell considered in the example described in the text.

considered. The yellow cells in this case are solid ($\text{RE}_2\text{Si}_2\text{O}_7$ or RE_2SiO_5) sites and black cells are gas sites, with the circles in this example used as site identifiers. A random neighbor of the gas site will be selected and the two sites will swap states. Again, the aim is to reduce the energy of the system overall, leading to coarsening of the pore structure. The example given in Figure 4.2 does not lead to a reduced energy of the system, but many events like this will lead to a rounding of the pores that reduces the energy of each pore.

In Version 1 of the model two methods were employed to capture the reaction between $\text{Y}_2\text{Si}_2\text{O}_7$ and $\text{H}_2\text{O}(\text{g})$. The reaction control was a threshold of the partial pressure of $\text{Si}(\text{OH})_4(\text{g})$. If a solid $\text{RE}_2\text{Si}_2\text{O}_7$ site had three neighbor $\text{RE}_2\text{Si}_2\text{O}_7$ sites and two gas sites a reaction was attempted. If the gas sites had a partial pressure of $\text{Si}(\text{OH})_4(\text{g})$ of 1.0 atm the reaction had a 0% chance of occurring, with an increasing probability as partial pressure decreased. For example, with 0.5 atm of $\text{Si}(\text{OH})_4(\text{g})$ a reaction had 50% chance of occurring and 0.25 atm of $\text{Si}(\text{OH})_4(\text{g})$ meant a 75% chance. If this criterion is met then a reaction is allowed. The reaction transforms the original $\text{RE}_2\text{Si}_2\text{O}_7$ site to a RE_2SiO_5 state along with two randomly selected $\text{RE}_2\text{Si}_2\text{O}_7$ neighbors. A fourth $\text{RE}_2\text{Si}_2\text{O}_7$ neighbor then transforms to a gas site. The ratio of three RE_2SiO_5 to one gas site transformations reflect the $\sim 25\%$ pore volume formed with RE_2SiO_5 from the reaction between $\text{RE}_2\text{Si}_2\text{O}_7$ and $\text{H}_2\text{O}(\text{g})$. An illustration of this reaction is given in Figure 4.3. New gas sites created during the reaction had their concentration of $\text{Si}(\text{OH})_4(\text{g})$ set to 1.0 atm. The control of the reaction by the inverse linear proportionality between partial pressure and probability was computationally fast, but was inaccurate in modeling the observed system.

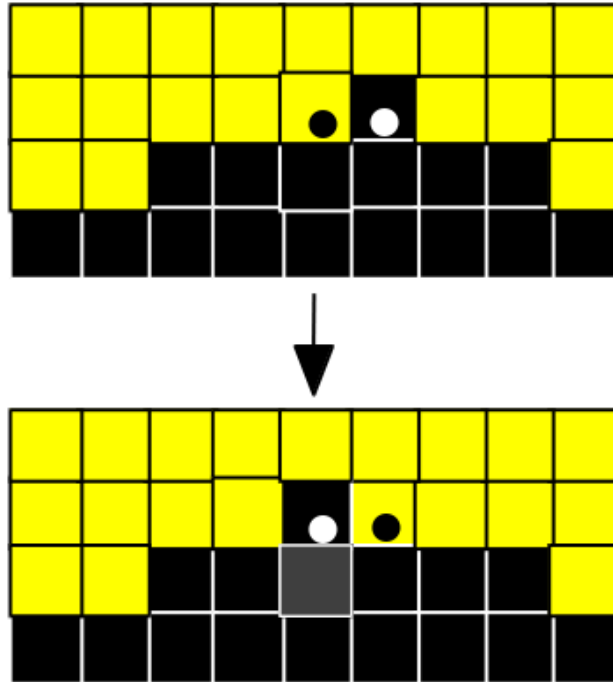


Figure 4.2: A simplified example of a solid grain neighboring a pore and surface diffusion occurring. The solid grain (either $\text{RE}_2\text{Si}_2\text{O}_7$ or RE_2SiO_5) is yellow and the pore is black. The example shown here does not change the energy of the system.

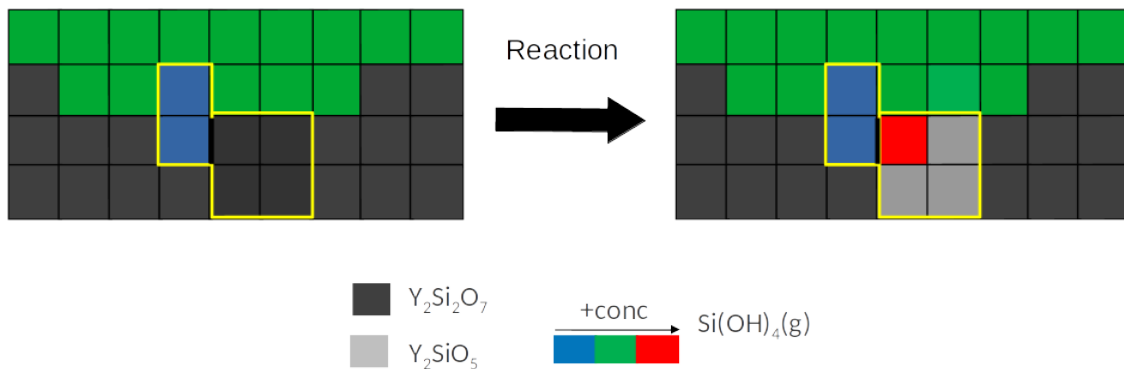


Figure 4.3: A simplified example of a reaction between $\text{RE}_2\text{Si}_2\text{O}_7$ and $\text{H}_2\text{O}(\text{g})$ that occurs in the model presented in 2D. The red cells indicate the highest concentration of $\text{Si(OH)}_4(\text{g})$. After the reaction between $\text{H}_2\text{O}(\text{g})$ and $\text{RE}_2\text{Si}_2\text{O}_7$ has occurred the new gas site has a high concentration of $\text{Si(OH)}_4(\text{g})$. This will then diffuse out of the system.

In Version 2, the gas phase neighbors to the reaction $\text{RE}_2\text{Si}_2\text{O}_7$ site are required to have a partial pressure of $\text{Si(OH)}_4(\text{g})$ less than $3.5 \cdot 10^{-5}$ atm. If this criterion is met then a reaction is allowed, no further probability was included. The mechanics of the reaction were not changed other than the resultant partial pressure of $\text{Si(OH)}_4(\text{g})$ in the new gas site, which was set to an $\text{Si(OH)}_4(\text{g})$ partial pressure of $5 \cdot 10^{-5}$ atm.

A finite differences model is used to simulate molecular diffusion of $\text{Si(OH)}_4(\text{g})$ away from the reaction surface using Fick's Second Law. Finite differences are calculated using the equation

$$\frac{\delta^2 c}{\delta x^2} = c_{x+1} - 2c_x + c_{x-1} \quad (4.1)$$

where x is the current raster position in the computational model. Finite differences are repeated in all dimensions, considering the nearest neighbors of the current cell. All of the flux values are then summed. Once the flux sum value is computed for a cell it is then copied into a new matrix and the value at the next cell is computed. The final concentration value at each cell is then calculated using the following equation:

$$c[i] = c_{old}[i] + (diffusionratio \cdot D) \cdot val \quad (4.2)$$

where val is the summed fluxes in all dimensions, D is the unitless diffusion coefficient, and diffusion ratio is the number of diffusion steps carried out between each Monte Carlo step of the Potts model, in this case 10.

An additional Potts rule is used to handle the $\text{Si(OH)}_4(\text{g})$ removal from the system. Because experimental conditions at the surface of the coating include $\text{H}_2\text{O}(\text{g})$ velocities in the range of 150 – 180 m/s a rule was implemented that any cells with $\text{Si(OH)}_4(\text{g})$ partial pressure greater than 0 would have their partial pressures set to 0 if that cell is above the original surface of the coating. This simulates the rapid supply of $\text{H}_2\text{O}(\text{g})$ and removal of $\text{Si(OH)}_4(\text{g})$. Simulations of microstructural evolution of $\text{RE}_2\text{Si}_2\text{O}_7$ and $\text{H}_2\text{O}(\text{g})$ were carried out for 200 – 5000 Monte Carlo time steps with a starting microstructure of one single state for $\text{RE}_2\text{Si}_2\text{O}_7$ and several layers of gas states above this single grain, simulating the surface of an EBC coating. Simulation box size was $50x50x200$.

A Version 3 of the model was developed that adjusted the $\text{Si(OH)}_4(\text{g})$ concentration threshold for the reaction between $\text{RE}_2\text{Si}_2\text{O}_7$ and $\text{H}_2\text{O}(\text{g})$ to $1.8 \cdot 10^{-6}$ atm to better align with the activity data used to calculate the reaction threshold of RE_2SiO_5 and $\text{H}_2\text{O}(\text{g})$. The $\text{Si(OH)}_4(\text{g})$ sink at the top of the simulations was also modified in the simulation space to more closely mirror a gas boundary layer changing with velocity across the surface of the sample. The intention with this addition was to achieve a change in depletion depth in accordance with velocity effects observed in experimental results. The sink begins at a defined level above the leading edge of the surface of the $\text{RE}_2\text{Si}_2\text{O}_7$ sites in the initial simulation box. The sink then begins to move away from the initial $\text{RE}_2\text{Si}_2\text{O}_7$ surface moving in the x direction of the simulation box. The growth of the RE_2SiO_5 layer is modeled by a $\text{sqrt}(x)$ dependence. With this change in the sink behavior the simulation space was changed to $1000x50x500$ in order to simulate a large distance in the x direction corresponding with a change in the velocity along the surface of the sample. Periodicity of the simulation box was also changed with the addition of the gas boundary layer. The simulation box is no longer periodic in the x direction so as to not allow flow of gas between low and high velocity areas. All of these simulations were run on the Chama cluster at Sandia.

Experimental results presented in the previous chapter show a complex mechanism occurring with the densification of RE_2SiO_5 and the formation of RE_2O_3 on the surface above these dense areas. This simulation does not incorporate these phenomena and instead intends to model conditions at 1200°C with velocities below 175 m/s where dense RE_2SiO_5 is not observed.

4.3 Results

A simulation using Version 1 (the computationally fast model) that was first developed is shown in Figure 4.4 with progression from 50 to 200 time steps. The reaction in this case had linear kinetics, rather than parabolic kinetics observed experimentally for dense phase pure $\text{RE}_2\text{Si}_2\text{O}_7$ as discussed earlier. The presented example was computationally fast but failed to simulate the observed reaction kinetics for phase pure $\text{Y}_2\text{Si}_2\text{O}_7$. The diffusion coefficient for $\text{Si}(\text{OH})_4(\text{g})$ outward, D , was lowered leading to parabolic reaction kinetics and computationally expensive simulations. Figure 4.5 shows the progression of the model results with parabolic reaction kinetics (Version 2) from 50 – 5000 Monte Carlo steps. The RE_2SiO_5 grains and pore structure here continued to be physically realistic. The simulation reaches the same RE_2SiO_5 layer depth in 5000 timesteps as Version 1 simulations did in 25.

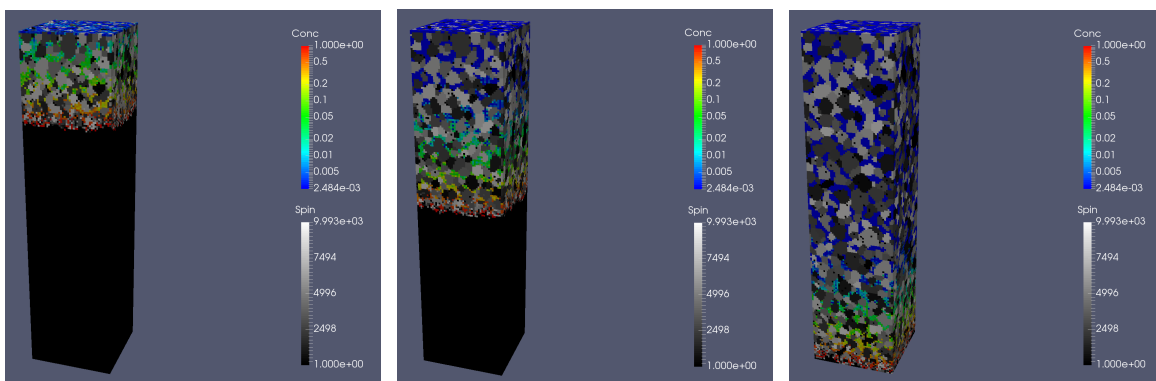


Figure 4.4: Still images from a Version 1 simulation animation of the $\text{RE}_2\text{Si}_2\text{O}_7$ EBC coating reacting with water vapor resulting in linear reaction kinetics. Time steps are 50, 100, 200, moving from left to right. The initial simulation box was simply a single $\text{RE}_2\text{Si}_2\text{O}_7$ grain with several elements of gas states above. Black areas are $\text{RE}_2\text{Si}_2\text{O}_7$, gray areas are different grains of RE_2SiO_5 , and the colors represent $\text{Si}(\text{OH})_4(\text{g})$ partial pressures.

Version 3 of the simulation included larger simulation boxes to allow for the gas boundary layer to grow across the surface of the sample. Images from steps 100, 500, and 1000 in this simulation are shown in Figure 4.6 comparing the gas boundary behavior and depth of the reaction front. The reaction front moves further into the $\text{RE}_2\text{Si}_2\text{O}_7$ with time and the concentration of $\text{Si}(\text{OH})_4(\text{g})$ near the surface of the solid sample decreases with time as well.

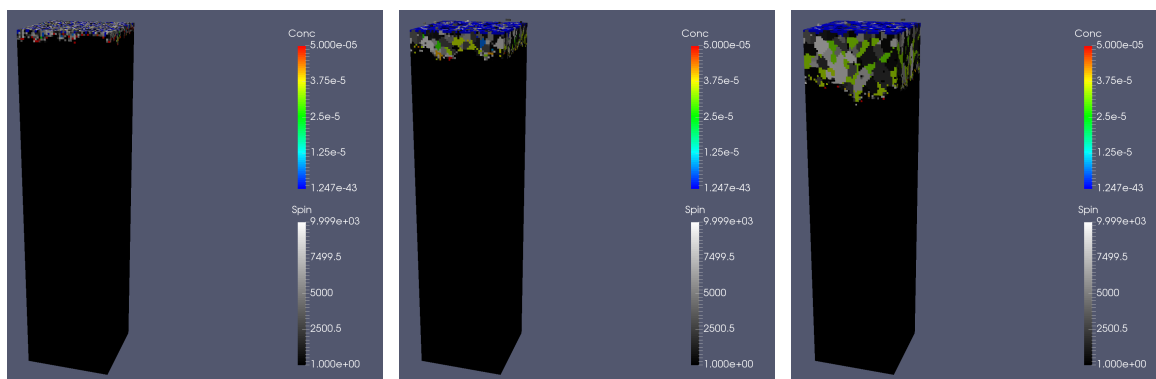


Figure 4.5: Still images from a Version 2 simulation animation of the $\text{RE}_2\text{Si}_2\text{O}_7$ EBC coating reacting with water vapor resulting in parabolic reaction kinetics. Time steps are 50, 1000, 5000, moving from left to right. The initial simulation box was simply a single $\text{RE}_2\text{Si}_2\text{O}_7$ grain with several elements of gas states above. Black areas are $\text{RE}_2\text{Si}_2\text{O}_7$, gray areas are different grains of RE_2SiO_5 , and the colors represent $\text{Si}(\text{OH})_4(\text{g})$ partial pressures.

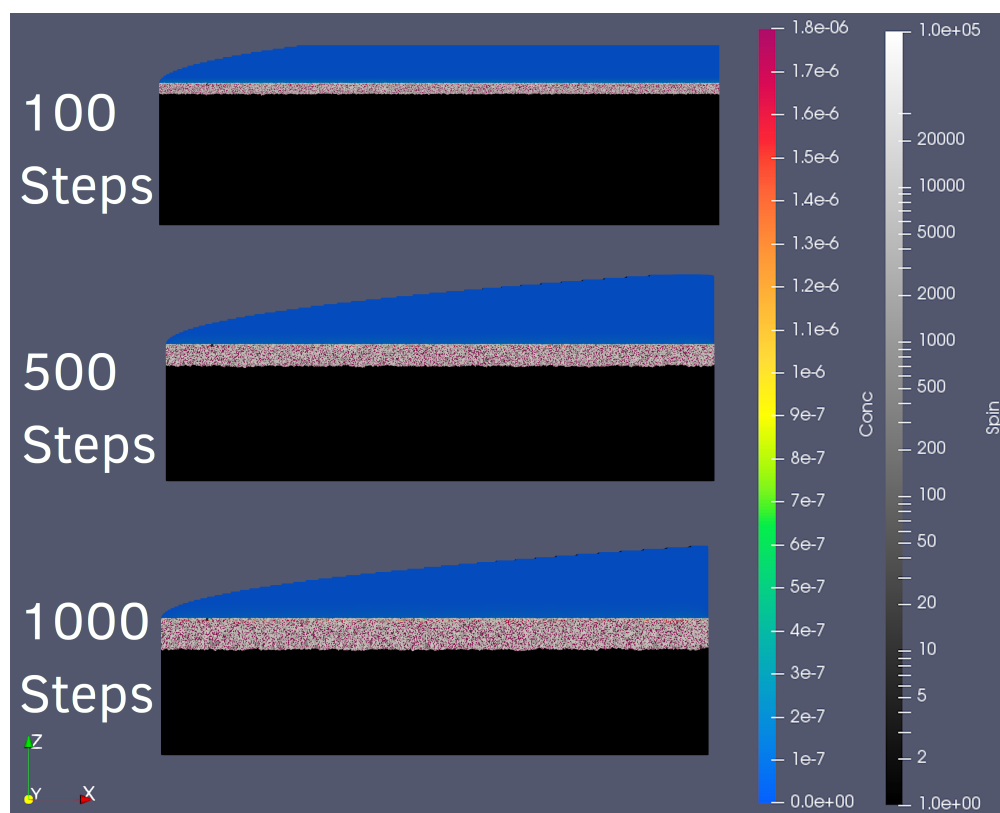


Figure 4.6: Comparison of the Version 3 simulation after 100, 500, and 1000 steps. The gas boundary layer saturates over time. Black areas are $\text{RE}_2\text{Si}_2\text{O}_7$, gray areas are different grains of RE_2SiO_5 , and the colors represent $\text{Si}(\text{OH})_4(\text{g})$ partial pressures.

Zoomed in images from the area on the left of the simulation box where velocity is modeled to be highest are shown in Figure 4.7 to allow for investigation of the pore structure evolution over time. The pores begin

small and often elongated in the image shown for step 100. At the reaction interface small elongated pores are seen extending from the surface of the $\text{RE}_2\text{Si}_2\text{O}_7$, often a single site wide. This agrees with experimental observations that show elongated pores forming perpendicular to the reaction interface shortly after reaction between $\text{RE}_2\text{Si}_2\text{O}_7$ and $\text{H}_2\text{O}(\text{g})$. Over time the pores become more equiaxed and larger, moving from step 500 to 1000. The elongated small pores at the reaction interface do remain in all steps, though, circled in blue in Figure 4.7. Looking at the image from step 1000 there seems to be a stronger orientation preference moving from the surface of the sample to the reaction interface, with pores near the reaction interface being less equiaxed. These views also show in more detail the change in concentration of $\text{Si}(\text{OH})_4(\text{g})$ near the solid/gas interface.

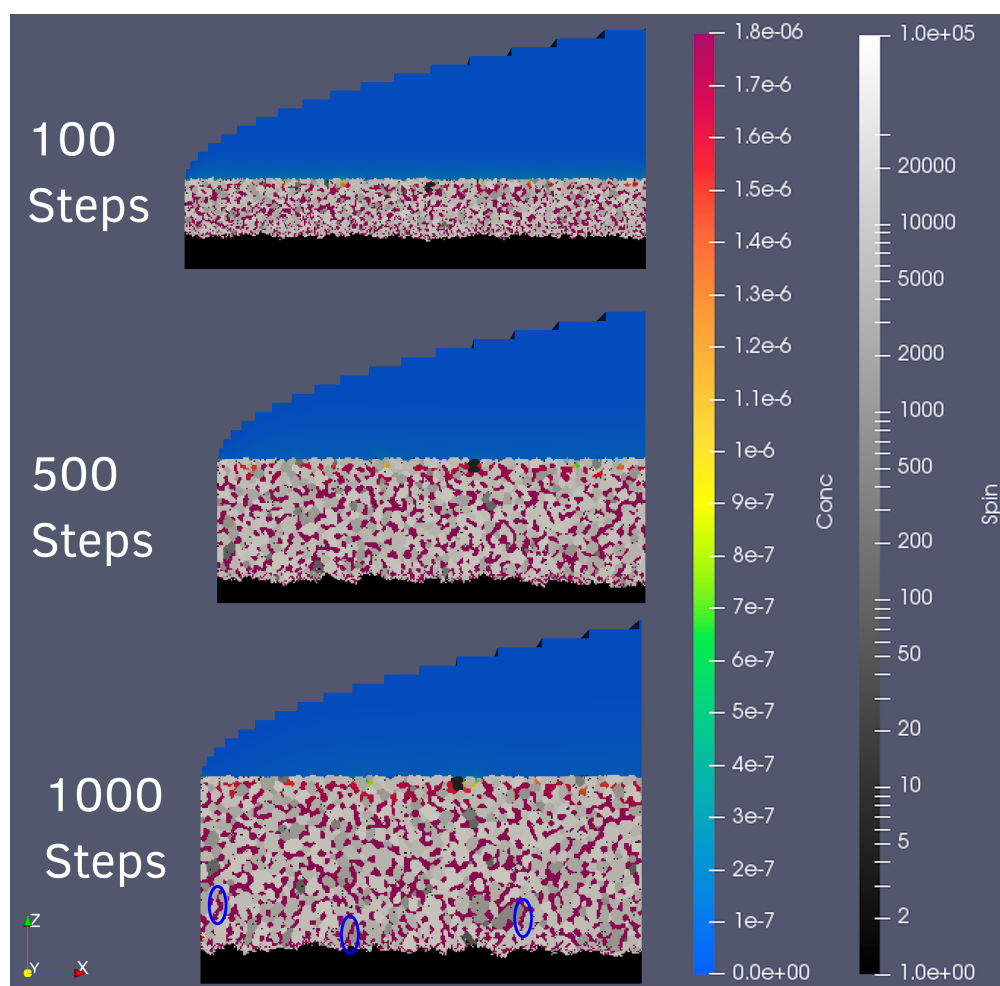


Figure 4.7: A comparison of a cropped in view of each Version 3 simulation box showing the pore detail over time. Black areas are $\text{RE}_2\text{Si}_2\text{O}_7$, gray areas are different grains of RE_2SiO_5 , and the colors represent $\text{Si}(\text{OH})_4(\text{g})$ partial pressures.

Comparing the cropped image of the simulation after 500 steps with micrographs from experimental results allows for linking these simulations to physical length and time. Figures 4.8, 4.9, and 4.10 show

side-by-side comparisons of micrographs taken from the cross section of an SPS $Y_2Si_2O_7$ sample exposed in the steam-jet at 1200°C for 60h and the cropped image of the simulation after 500 steps. The pore structure in these images is similar, including the small pores perpendicular to the reaction interface. The average SiO_2 depletion depth in the experimental images is 6.2 microns in 60 hours of exposure. The depletion layer in the simulation images is 80 sites deep. This corresponds to 13 sites per micron. An hour of experimental time corresponds to 8.3 simulation steps.

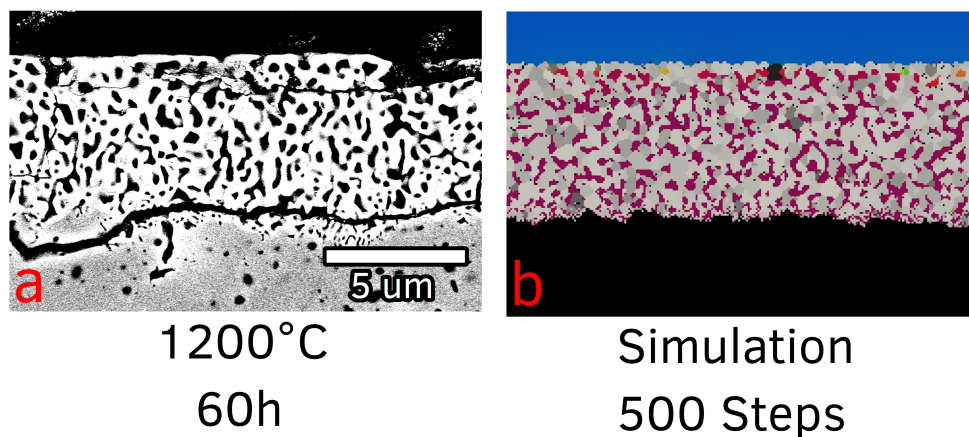


Figure 4.8: Direct comparison between a backscattered electron cross-sectional image from an SPS $Y_2Si_2O_7$ sample exposed in the steam-jet furnace at 1200°C for 60h and a simulation after 500 steps. The experimental depletion depth is $6.5\ \mu\text{m}$ over 60h, with the simulation depth being 80 sites.

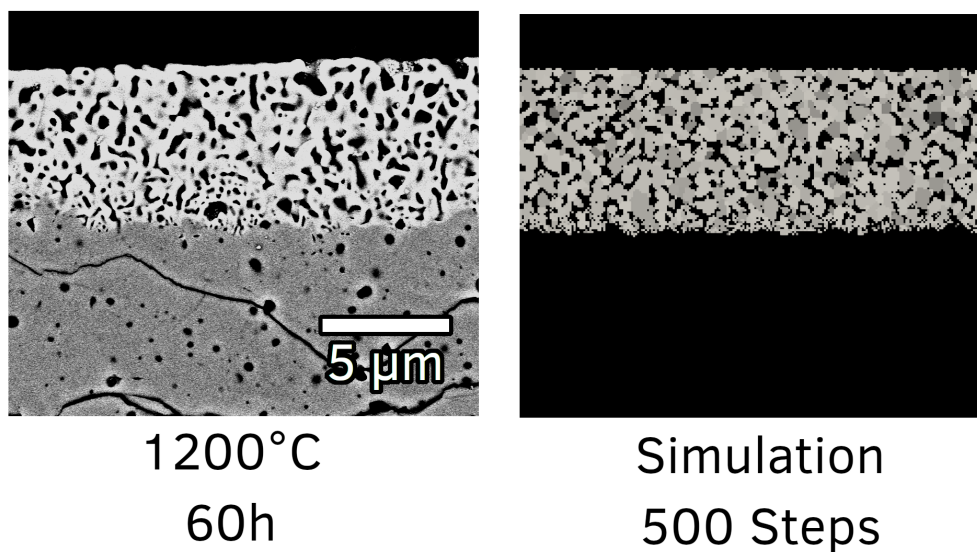


Figure 4.9: Direct comparison between a backscattered electron cross-sectional image from an SPS $Y_2Si_2O_7$ sample exposed in the steam-jet furnace at 1200°C for 60h and a simulation after 500 steps. The experimental depletion depth is $6.3\ \mu\text{m}$ over 60h, with the simulation depth being 80 sites.

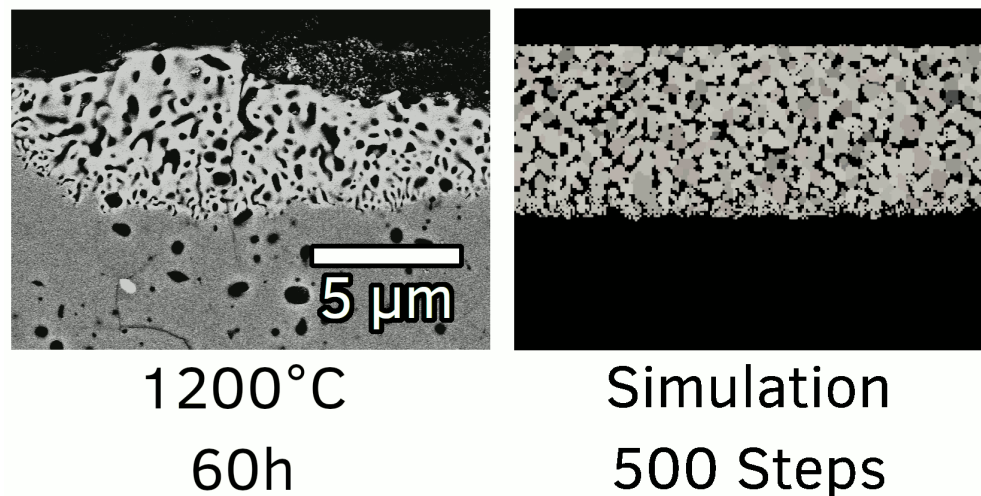


Figure 4.10: Direct comparison between a backscattered electron cross-sectional image from an SPS $Y_2Si_2O_7$ sample exposed in the steam-jet furnace at 1200°C for 60h and a simulation after 500 steps. The experimental depletion depth is $5.7 \mu\text{m}$ over 60h, with the simulation depth being 80 sites.

4.4 Discussion

Plots of the number of RE_2SiO_5 cells as a function of time for models Version 1 and 2 are shown in Figure 4.11. This figure provides a comparison of the reaction kinetics between model Versions 1.0 and 2.0 because the number of RE_2SiO_5 cells directly describes the rate that the reaction between $RE_2Si_2O_7$ and $H_2O(g)$ is progressing.

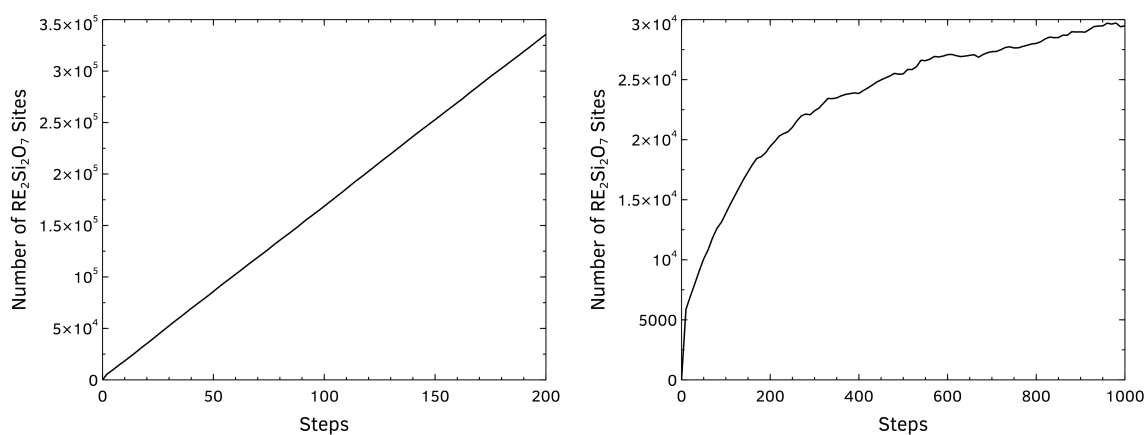


Figure 4.11: Total number of RE_2SiO_5 sites present in the simulation plotted over number of timesteps. Left is Version 1, right is Version 2.

The Version 1 reaction kinetics according to Figure 4.11 (left) are clearly linear, which does not agree with experimental results presented in Chapter 3. However, this simulation does have pore features and

RE_2SiO_5 grain sizes and shapes that are well matched to experimental observation. The RE_2SiO_5 grains closer to the reaction interface are smaller compared to the surface of the coating and RE_2SiO_5 grains have a round character that is to be expected of the coarsened physical system. It should be noted that there are unreacted portions of $\text{RE}_2\text{Si}_2\text{O}_7$ trapped in many of these RE_2SiO_5 grains. This is an anomaly that is present in both current models as a result of the simple four site transformation that occurs during reaction. Overall, this simulation demonstrated that all the phenomena relating to the reaction of water vapor with $\text{RE}_2\text{Si}_2\text{O}_7$ EBCs could be captured in a model and provide accurate physical features, but needed revision with respect to reaction kinetics.

The Version 2 simulation, shown in Figure 4.11 (right) better represents the reaction kinetics while maintaining realistic physical microstructural features.

Model Version 3 has progressed to a point where pore structure and size closely mirror experimental results obtained using the steam-jet furnace. Figure 4.8 shows varying pore sizes and shapes in the simulation, similar to what is found in the micrograph next to it. Figure 4.12 confirms that the model follows parabolic kinetics, with the number of new RE_2SiO_5 sites appearing decreasing with time. Because the Potts model is rule based it necessitates that a mechanism be understood before it can be included in the simulation. This model does allow extrapolation of results past time scales accessible in the laboratory, and the ability to probe interactions at temperatures outside the range studied experimentally.

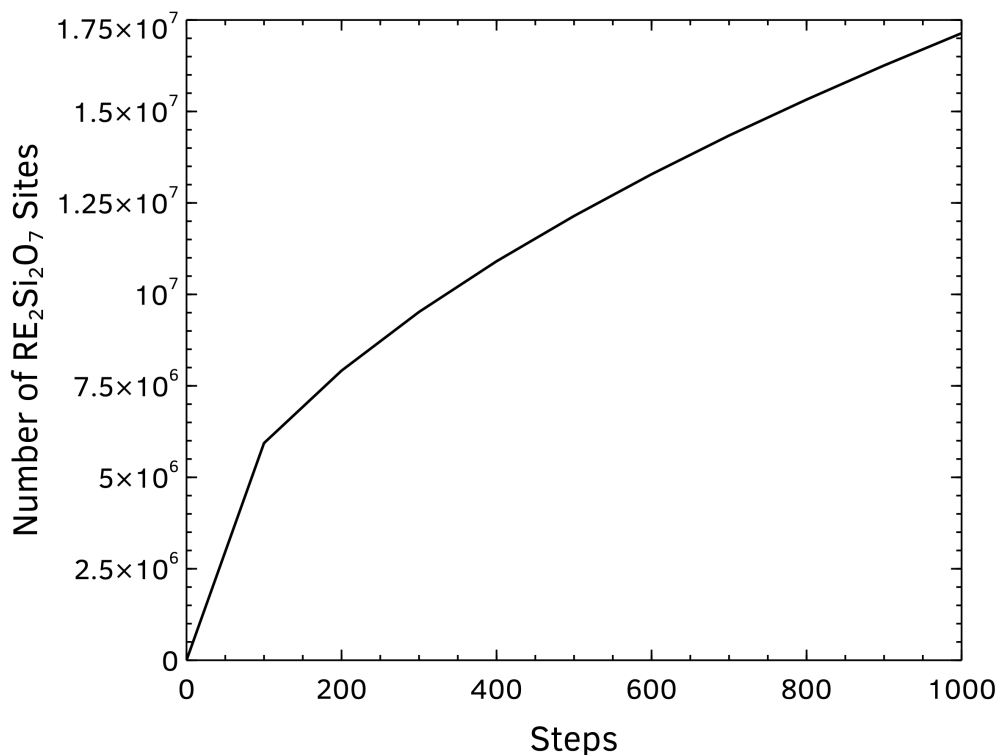


Figure 4.12: Total number of RE_2SiO_5 sites present in simulation Version 3 plotted over time steps.

It should be noted that while a gas boundary layer has been included in the model, as seen in the results with a $\text{Si(OH)}_4(\text{g})$ sink above the gas boundary line, currently this implementation does not result in a $\text{Si(OH)}_4(\text{g})$ concentration gradient with boundary layer thickness. The surface $\text{H}_2\text{O}(\text{g})$ velocity is not currently represented in this model and so increasing velocity $0 < v < 175$ m/s does not result in increased SiO_2 depletion depth, as would be expected based on experimental results in the previous chapter. Two possibilities are offered to explain why the gas boundary layer is not producing the expected concentration gradient. First, the boundary layer thickness is small in relation to the diffusion rate of $\text{Si(OH)}_4(\text{g})$. A slower diffusion rate of $\text{Si(OH)}_4(\text{g})$ would cause the distance from $\text{Si(OH)}_4(\text{g})$ boundary layer sink to the surface of the $\text{RE}_2\text{Si}_2\text{O}_7$ to be more consequential. A second possibility is that the simulations currently are unable to capture both the short times of diffusion for $\text{Si(OH)}_4(\text{g})$ through the gas boundary layer and the long experimentation times.

The simulation results presented for Version 3 of the model are computationally expensive. However, the simulations allow for SiO_2 depletion and microstructural evolution to be determined 13.33 times faster than in real time. 60h of experimentation represented in 500 steps of simulation required 4.5h of computation time. So, for example, 10,000 hours (approximately 14 months) of real world exposure could be simulated in approximately one month of computation time. Reducing the computational time further could be accomplished through optimization of the rules used in the model or using a larger number of compute nodes. Simulations also allow for discontinuous experimentation to take place, with the end state of one simulation used to run further simulations.

4.5 Conclusions

A hybrid Potts/diffusion model has been implemented using the SPPARKS framework developed at Sandia National Laboratories. The model uses a Monte Carlo method to simulate events such the reaction of $\text{RE}_2\text{Si}_2\text{O}_7$ and RE_2SiO_5 with $\text{H}_2\text{O}(\text{g})$ to form $\text{Si(OH)}_4(\text{g})$ and reduce the SiO_2 content in the solid state, grain coarsening, and surface diffusion. The diffusion of $\text{Si(OH)}_4(\text{g})$ product outward is handled through a finite differences method. The simulations display microstructural features similar to those observed experimentally such as porosity and RE_2SiO_5 grains that coarsen with time. Importantly, simulated reactions using Versions 2 and 3 exhibit parabolic kinetics consistent with experimental results for dense phase pure $\text{RE}_2\text{Si}_2\text{O}_7$ materials. In its current form every 80 Monte Carlo steps in the simulation is equivalent to 1 hour of experimental time, and 13 site lengths correspond to 1 micron.

4.6 Recommendations for Future Work

While the current model closely resembles the results obtained from phase pure SPS $Y_2Si_2O_7$, the ultimate goal of the model would be to more closely approximate the behavior of APS coatings. The first step on this path is to incorporate multiple $RE_2Si_2O_7$ grains into the initial simulation box of the same size and shape of grains found in SPS $Y_2Si_2O_7$. The next step would be to introduce features in the initial state of the system that approximate SiO_2 -poor RE_2SiO_5 splats found in the initial APS microstructures. This process could begin with manual input, placing the splats individually, by copying a reference APS cross-sectional image. Later, randomization rules could be used to create simulated APS microstructures where a predetermined size distribution and volume fraction of RE_2SiO_5 splats are placed by an algorithm.

Calculation of the gas boundary layer thickness representative of the experiments would be an important step in improving the model accuracy, thereby accounting for observed gas velocity dependence. Because number of sites have been tied to a physical length, the gas boundary layer programmed into the model could then be accurately modeled to these experimental conditions. The boundary layer could initially be represented by certain user defined heights in steps to match the experimental data. A more accurate representation would be the use of a mathematical function that closely emulates the thickness of the gas boundary layer. Incorporating temperature effects in the model can be accomplished by changing the reaction threshold of the partial pressure of $Si(OH)_4(g)$. Micrographs obtained at different times and temperatures should be utilized to further link the model and experiment.

Another important mechanism that should be added to the model is not yet understood: the densification of the RE_2SiO_5 layer observed in high velocity regions of specimens after steam-jet testing. Hypotheses for the formation of the dense RE_2SiO_5 could be tested in this model framework. This densification is observed to be a prerequisite for widespread formation of RE_2O_3 on the surface of steam-jet samples. Determination of this mechanism would allow for more accurate simulations of EBC behavior in regions experiencing velocities greater than 175 m/s.

Chapter 5

Summary and Impact

The objective of this research was to determine what effect, if any, the air plasma spray (APS) process may have on the lifetime of rare earth disilicates (REDS) as environmental barrier coatings (EBCs). $Y_2Si_2O_7$ coatings and phase pure samples of $Y_2Si_2O_7$ and Y_2SiO_5 were fabricated at UVA, Y_2O_3 samples were provided by MaTek, and $Yb_2Si_2O_7$ coatings were provided by Rolls-Royce Corporation. Dilatometry, differential scanning calorimetry (DSC), and room temperature as well as high-temperature XRD were used to study the thermal behavior of the phase pure and APS materials. An updated steam-jet furnace was developed that allowed for testing the thermochemical stability of these materials in high-temperature, high-velocity $H_2O(g)$ without the impact of $Si(OH)_4(g)$ contaminants at temperatures above $1200^\circ C$. A first-of-its-kind 3D computational model was developed using the Stochastic Parallel Particle Kinetic Simulator (SPPARKS) software to model the microstructural evolution of $RE_2Si_2O_7$ over time during steam-jet testing with the goal of lifetime determination for EBCs.

DSC and XRD of APS $Y_2Si_2O_7$ coatings fabricated at UVA showed that as-sprayed coatings were mostly amorphous, but crystallinity was restored when annealed above $1050^\circ C$. While the starting powder in these processes was pure β - $Y_2Si_2O_7$ the crystallized coatings contained α , β , and ζ - $Y_2Si_2O_7$ polymorphs along with Y_2SiO_5 . Dilatometry revealed that these additional polymorphs in the APS structure raised the bulk coefficient of thermal expansion (CTE) of the coating initially. However, with subsequent dilatometry and XRD measurements the bulk CTE of the coating decreased due to the equilibration of the α and ζ polymorphs to β , though the overall CTE remained higher than phase pure $Y_2Si_2O_7$. High-temperature XRD of phase pure $Yb_2Si_2O_7$, Yb_2SiO_5 , $Y_2Si_2O_7$, and Y_2SiO_5 performed at the Advanced Photon Source at Argonne National Laboratory allowed for the measurement of anisotropy in these rare earth silicates. $Yb_2Si_2O_7$, Yb_2SiO_5 , and Y_2SiO_5 had monoclinic structures with large amounts of anisotropy, while $Y_2Si_2O_7$ mostly

displayed an orthorhombic structure during measurement. The $\text{Yb}_2\text{Si}_2\text{O}_7$ and Yb_2SiO_5 measurements, in particular are new. All of these results combine to show the difficulty in making a coating from these materials, as their thermal cycling behavior is likely to cause stresses and cracking due to difference in their thermal expansion in each direction. These high-temperature XRD results will be published in the future, either in Powder Diffraction or the Journal of the American Ceramic Society.

Steam-jet testing of phase pure materials at temperatures above 1200°C using a PtRh capillary allowed for a full understanding of the thermochemical stability of the Y_2O_3 - SiO_2 system in high-temperature, high-velocity water vapor. Previous literature had shown the volatility of Y_2O_3 , not SiO_2 , in high-temperature water vapor[39]. This current work shows no such volatility occurring after 60h of exposure in the steam-jet furnace at 1400°C . The reaction of Y_2SiO_5 with $\text{H}_2\text{O}(\text{g})$ to form Y_2O_3 was also observed for the first time in high-temperature, high-velocity water vapor, requiring velocities above 170 m/s. This reaction was observed both on phase pure Y_2SiO_5 and from Y_2SiO_5 that had resulted from the reaction between $\text{Y}_2\text{Si}_2\text{O}_7$ and $\text{H}_2\text{O}(\text{g})$. Densification of product Y_2SiO_5 was also observed at velocities above 170 m/s, with increasing velocities above 170 m/s showing a decrease in SiO_2 depletion depth. All of these results were novel, and have been published in the Journal of the American Ceramic Society. The activation energy of the reaction between $\text{Y}_2\text{Si}_2\text{O}_7$ and $\text{H}_2\text{O}(\text{g})$ was measured and found to be 382 kJ/mol after 60h of exposure in the steam-jet furnace. This is approximately six times greater than the activation energy of the reaction between SiO_2 and $\text{H}_2\text{O}(\text{g})$.

For the first time dense and abradable APS $\text{Yb}_2\text{Si}_2\text{O}_7$ coatings provided by Rolls-Royce Corporation were also tested in the steam-jet at temperatures of 1200, 1300, 1400°C for 60, 125, and 250h to determine if a difference in thermochemical stability was observed compared to phase pure materials. The APS materials showed increased erosion of Yb_2SiO_5 at the impingement site of testing. While erosion of the porous product RE_2SiO_5 is common, even in phase pure materials, the increased porosity and cracking from the APS process made the product Yb_2SiO_5 more easy to remove. Large pores and cracks were seen to be fast pathways for the diffusion of $\text{H}_2\text{O}(\text{g})$ into the system, causing increased local SiO_2 depletion. SiO_2 -poor splats that occur naturally from the APS process were found to slow the SiO_2 depletion front. These splats act as physical barriers, requiring that the reaction front proceed around them and increasing the diffusion distance of $\text{Si}(\text{OH})_4(\text{g})$ out of the system. The abradable coatings experienced greater amounts of local SiO_2 depletion due to the increased number of pores. These results will be written up and published in the Journal of the American Ceramic Society.

A first-of-its-kind computational model was developed to simulate the microstructural evolution of $\text{RE}_2\text{Si}_2\text{O}_7$ reacting with $\text{H}_2\text{O}(\text{g})$ in steam-jet conditions. This model has undergone several iterations so far. Version 1 of this model captured some features of the system, such as pore shape, but had linear kinet-

ics, rather than the experimentally observed parabolic kinetics. Versions 2 and 3 of the model corrected this kinetic issue. Version 3 of the model also introduced a gas boundary layer to the model in an attempt to capture the velocity effects observed experimentally on phase pure and APS rare earth silicates. The model was able to be correlated to physical length and time using cross-sectional micrographs from experimentally tested samples. In its current form 80 Monte Carlo steps corresponds to 1 hour of experimental time, and 13 site lengths corresponds to a measurement of 1 micron. This model currently allows for 10,000 hours of experimental exposure to be simulated in one month of computation time. These results can be written and submitted soon, but the model has much room for future work. The incorporation of additional initial microstructural features to more closely mimic an APS material being the primary area of work.

The findings of this dissertation demonstrate new findings in the thermomechanical and thermochemical behavior of rare earth silicates. These findings combined together give a picture of rare earth disilicates in all important factors: while CTE match between $Y_2Si_2O_7$, $Yb_2Si_2O_7$ and SiC is good, the anisotropy of both of these materials, and the polymorphism of $Y_2Si_2O_7$ especially, require extra consideration. The CTE of an APS coating cannot be assumed to be close to the phase pure materials they are sprayed from, either. The thermochemical stability of these silicates increases with decreasing SiO_2 content, as expected. The behavior of these systems above 170 m/s requires further research to understand the mechanism causing densification of RE_2SiO_5 and the decrease in SiO_2 depletion depth with increasing velocity. APS materials show weaknesses and strengths arising from their inhomogeneous microstructures. These facets must be leveraged in order to best serve the coating need of the EBC. A lifetime model capturing the microstructural evolution of the rare earth disilicate system has been made that allows for lifetime testing to occur much faster than experimentation would allow. Ultimately, the knowledge on the rare earth silicate systems as EBC coatings has been pushed forward both on a fundamental science and engineering level.

Bibliography

- [1] G. Gardiner. “Aeroengine Composites, Part 1: The CMC invasion”. In: *Composites World* (2015). URL: <https://www.compositesworld.com/articles/aeroengine-composites-part-1-the-cmc-invasion>.
- [2] Elizabeth J Opila and Raiford E Hann. “Paralinear Oxidation of CVD SiC in Water Vapor”. In: *Journal of the American Ceramic Society* 80.1 (1997), pp. 197–205.
- [3] Raymond C. Robinson and James L. Smialek. “SiC recession caused by SiO₂ scale volatility under combustion conditions: I. Experimental results and empirical model”. In: *Journal of the American Ceramic Society* 82.7 (1999), pp. 1817–1825. ISSN: 00027820. DOI: [10.1111/j.1151-2916.1999.tb02004.x](https://doi.org/10.1111/j.1151-2916.1999.tb02004.x).
- [4] Elizabeth J. Opila, James L. Smialek, Raymond C. Robinson, Dennis S. Fox, and Nathan S. Jacobson. “SiC Recession Caused by SiO₂ Scale Volatility under Combustion Conditions: II, Thermodynamics and Gaseous-Diffusion Model”. In: *Journal of the American Ceramic Society* 82.7 (1999), pp. 1826–1834. ISSN: 00027820. DOI: [10.1111/j.1151-2916.1999.tb02005.x](https://doi.org/10.1111/j.1151-2916.1999.tb02005.x).
- [5] Émilien Darthout, Aurélie Quet, Nadi Braïdy, and François Gitzhofer. “Lu₂O₃-SiO₂-ZrO₂ Coatings for Environmental Barrier Application by Solution Precursor Plasma Spraying and Influence of Precursor Chemistry”. In: *Journal of Thermal Spray Technology* 23.3 (2013), pp. 325–332. ISSN: 1059-9630. DOI: [10.1007/s11666-013-9987-7](https://doi.org/10.1007/s11666-013-9987-7).
- [6] Hagen Klemm. “Silicon nitride for high-temperature applications”. In: *Journal of the American Ceramic Society* 93.6 (2010), pp. 1501–1522. ISSN: 00027820. DOI: [10.1111/j.1551-2916.2010.03839.x](https://doi.org/10.1111/j.1551-2916.2010.03839.x).
- [7] I A Bondar. “Rare-earth silicates”. In: *Ceramics International* 8.3 (1982), pp. 83–89. DOI: [10.1016/0272-8842\(82\)90022-0](https://doi.org/10.1016/0272-8842(82)90022-0).

- [8] Nathan S Jacobson. “Silica activity measurements in the Y_2O_3 - SiO_2 system and applications to modeling of coating volatility”. In: *Journal of the American Ceramic Society* 97.6 (2014), pp. 1959–1965. DOI: [10.1111/jace.12974](https://doi.org/10.1111/jace.12974).
- [9] N A Toropov and I A Bondar. “Silicates of the Rare Earth Elements Communication 3, Phase Diagram of the Binary System Yttrium Oxide-Silica”. In: *Bulletin of the Academy of Sciences of the USSR Division of Chemical Science* 10.4 (1961), pp. 502–508. ISSN: 0568-5230. DOI: [10.1007/BF00909109](https://doi.org/10.1007/BF00909109).
- [10] Huahai Mao, Malin Selleby, and Olga Fabrichnaya. “Thermodynamic reassessment of the Y_2O_3 - Al_2O_3 - SiO_2 system and its subsystems”. In: *Calphad: Computer Coupling of Phase Diagrams and Thermochemistry* 32.2 (2008), pp. 399–412. ISSN: 03645916. DOI: [10.1016/j.calphad.2008.03.003](https://doi.org/10.1016/j.calphad.2008.03.003).
- [11] Olga Fabrichnaya, Hans Jürgen Seifert, Reinhold Weiland, Thomas Ludwig, Fritz Aldinger, and Alexandra Navrotsky. “Phase equilibria and thermodynamics in the Y_2O_3 - Al_2O_3 - SiO_2 system”. In: *Zeitschrift für Metallkunde* 92.9 (2001), pp. 1083–1097. ISSN: 0044-3093.
- [12] R A Golden. “Matrix Development for Water Vapor Resistant SiC-Based Ceramic Matrix Composites”. PhD thesis. University of Virginia, 2017.
- [13] Gustavo C.C. C Costa and Nathan S. Jacobson. “Mass Spectrometric Measurements of the Silica Activity in the Yb_2O_3 - SiO_2 System and Implications to Assess the Degradation of Silicate-based Coatings in Combustion Environments”. In: *Chemistry of Materials* (2015).
- [14] J. Felche. “Polymorphism and Crystal Data of the Rare-earth Disilicates of type $RE_2Si_2O_7$ ”. In: *Journal of the Less-Common Metals* 21 (1970), pp. 1–14.
- [15] Laura R. Turcer and Nitin P. Padture. “Towards multifunctional thermal environmental barrier coatings (TEBCs) based on rare-earth pyrosilicate solid-solution ceramics”. In: *Scripta Materialia* 154 (2018), pp. 111–117. ISSN: 13596462. DOI: [10.1016/j.scriptamat.2018.05.032](https://doi.org/10.1016/j.scriptamat.2018.05.032). URL: <https://doi.org/10.1016/j.scriptamat.2018.05.032https://linkinghub.elsevier.com/retrieve/pii/S1359646218303269>.
- [16] Ingo Hartenbach, Steffen F. Meier, and Thomas Schleid. “ ζ - $Y_2[Si_2O_7]$: Ein neuer Strukturtyp in der Yttrialit-Reihe / ζ - $Y_2[Si_2O_7]$: A New Structure Type within the Yttrialite Series”. In: *Zeitschrift für Naturforschung B* 61.9 (2006), pp. 1054–1060. ISSN: 1865-7117. DOI: [10.1515/znb-2006-0902](https://doi.org/10.1515/znb-2006-0902).
- [17] Ziqi Sun, Meishuan Li, and Yanchun Zhou. “Recent progress on synthesis, multi-scale structure, and properties of Y-Si-O oxides”. In: *International Materials Reviews* 59.7 (2014), pp. 357–383. ISSN: 0950-6608. DOI: [10.1179/1743280414Y.0000000033](https://doi.org/10.1179/1743280414Y.0000000033).

- [18] Bradley T Richards and Haydn N G Wadley. “Plasma spray deposition of tri-layer environmental barrier coatings”. In: *Journal of the European Ceramic Society* 34.12 (2014), pp. 3069–3083. ISSN: 09552219. DOI: [10.1016/j.jeurceramsoc.2014.04.027](https://doi.org/10.1016/j.jeurceramsoc.2014.04.027).
- [19] Bradley T Richards, Hengbei Zhao, and Haydn N G Wadley. “Structure, composition, and defect control during plasma spray deposition of ytterbium silicate coatings”. In: *Journal of Materials Science* 50.24 (2015), pp. 7939–7957. DOI: [10.1007/s10853-015-9358-5](https://doi.org/10.1007/s10853-015-9358-5).
- [20] Bradley T Richards. “Ytterbium Silicate Environmental Barrier Coatings”. PhD thesis. 2015.
- [21] J. W. Nowok, J. P. Kay, and R. J. Kulas. “Thermal expansion and high-temperature phase transformation of the yttrium silicate Y_2SiO_5 ”. In: *Journal of Materials Research* 16.08 (2001), pp. 2251–2255. ISSN: 0884-2914. DOI: [10.1557/JMR.2001.0309](https://doi.org/10.1557/JMR.2001.0309).
- [22] Ziqi Sun, Yanchun Zhou, Jingyang Wang, and Meishuan Li. “Thermal properties and thermal shock resistance of γ - $Y_2Si_2O_7$ ”. In: *Journal of the American Ceramic Society* 91.8 (2008), pp. 2623–2629. ISSN: 00027820. DOI: [10.1111/j.1551-2916.2008.02470.x](https://doi.org/10.1111/j.1551-2916.2008.02470.x).
- [23] Alberto J Fernández-Carrión, Mathieu Allix, and Ana I Becerro. “Thermal expansion of rare-earth pyrosilicates”. In: *Journal of the American Ceramic Society* 96.7 (2013), pp. 2298–2305. ISSN: 00027820. DOI: [10.1111/jace.12388](https://doi.org/10.1111/jace.12388).
- [24] M D Dolan, B Harlan, J S White, M Hall, S T Misture, S C Bancheri, and B Bewlay. “Structures and anisotropic thermal expansion of the α , β , γ , and δ polymorphs of $Y_2Si_2O_7$ ”. In: *Powder Diffraction* 23.1 (2008), pp. 20–25. DOI: [10.1154/1.2825308](https://doi.org/10.1154/1.2825308).
- [25] Kang N Lee. “Protective coatings for gas turbines”. In: *The gas turbine handbook* (2006), pp. 419–437.
- [26] Nasrin Al Nasiri, Niranjana Patra, Denis Horlait, Daniel Doni Jayaseelan, and William E. Lee. “Thermal Properties of Rare-Earth Monosilicates for EBC on Si-Based Ceramic Composites”. In: *Journal of the American Ceramic Society* 99.2 (2016), pp. 589–596. ISSN: 15512916. DOI: [10.1111/jace.13982](https://doi.org/10.1111/jace.13982).
- [27] Henry M. O’Byrne, Patrick K. Gallagher, and G.W. Berkstresser. “Thermal Expansion of Y_2SiO_5 Single Crystals”. In: *Journal of the American Ceramic Society* 71.1 (1988), pp. C–42–C–43. ISSN: 0002-7820. DOI: [10.1111/j.1151-2916.1988.tb05779.x](https://doi.org/10.1111/j.1151-2916.1988.tb05779.x).
- [28] Koichiro Fukuda and Hiroyuki Matsubara. “Anisotropic thermal expansion in yttrium silicate”. In: *Journal of Materials Research* 18.7 (2003), pp. 1715–1722. ISSN: 08842914. DOI: [10.1557/JMR.2003.0236](https://doi.org/10.1557/JMR.2003.0236).

- [29] R A Golden; E J Opila. “A method for assessing the volatility of oxides in high-temperature high-velocity water vapor”. In: *J. Eur. Ceram. Soc.* 36 (2016), pp. 1135–1147. DOI: [10.1016/j.jeurceramsoc.2015.11.016](https://doi.org/10.1016/j.jeurceramsoc.2015.11.016).
- [30] Marco Fritsch and Hagen Klemm. “The water vapor hot gas corrosion of MGC materials with Al₂O₃ as a phase constituent in a combustion atmosphere”. In: *Journal of the European Ceramic Society* 28.12 (2008), pp. 2353–2358. ISSN: 09552219. DOI: [10.1016/j.jeurceramsoc.2008.01.007](https://doi.org/10.1016/j.jeurceramsoc.2008.01.007).
- [31] Marco Fritsch. “Heißgaskorrosion keramischer Werkstoffe in H₂O-haltigen Rauchgasatmosphären”. PhD thesis. 2008, p. 193.
- [32] Marco Fritsch, Hagen Klemm, Matthias Herrmann, and Bjoern Schenk. “Corrosion of selected ceramic materials in hot gas environment”. In: *Journal of the European Ceramic Society* 26.16 (2006), pp. 3557–3565. ISSN: 09552219. DOI: [10.1016/j.jeurceramsoc.2006.01.015](https://doi.org/10.1016/j.jeurceramsoc.2006.01.015).
- [33] Shunkichi Ueno, D Doni Jayaseelan, Tatsuki Ohji, and Hua-Tay Lin. “Recession mechanism of Lu₂Si₂O₇ phase in high speed steam jet environment at high temperatures”. In: *Ceramics International* 32.7 (2006), pp. 775–778. DOI: [10.1016/j.ceramint.2005.05.014](https://doi.org/10.1016/j.ceramint.2005.05.014).
- [34] Shunkichi Ueno, Tatsuki Ohji, and Hua-tay Lin. “Recession behavior of Yb₂Si₂O₇ phase under high speed steam jet at high temperatures”. In: *Corrosion Science* 50 (2008), pp. 178–182. DOI: [10.1016/j.corsci.2007.06.014](https://doi.org/10.1016/j.corsci.2007.06.014).
- [35] Shunkichi Ueno, Tatsuki Ohji, and Hua-Tay Lin. “Recession behavior of Lu₂SiO₅ under a high speed steam jet at high temperatures”. In: *Ceramics International* 37.4 (2011), pp. 1185–1189. ISSN: 02728842. DOI: [10.1016/j.ceramint.2010.11.029](https://doi.org/10.1016/j.ceramint.2010.11.029).
- [36] Kang N Lee, Dennis S Fox, and Narottam P Bansal. “Rare earth silicate environmental barrier coatings for SiC/SiC composites and Si₃N₄ ceramics”. In: *Journal of the European Ceramic Society* 25.10 SPEC. ISS. (2005), pp. 1705–1715. DOI: [10.1016/j.jeurceramsoc.2004.12.013](https://doi.org/10.1016/j.jeurceramsoc.2004.12.013).
- [37] Kang N Lee, Dennis S Fox, Jeffrey I Eldridge, Dongming Zhu, Raymond C Robinson, Narottam P Bansal, and Robert A Miller. “Upper Temperature Limit of Environmental Barrier Coatings Based on Mullite and BSAS”. In: *Journal of the American Ceramic Society* 8.86 (2003), pp. 1299–1306.
- [38] Emilie Courcot, Francis Rebillat, Francis Teyssandier, and Caroline Louchet-Pouillier. “Thermochemical stability of the Y₂O₃-SiO₂ system”. In: *Journal of the European Ceramic Society* 30.4 (2010), pp. 905–910. ISSN: 09552219. DOI: [10.1016/j.jeurceramsoc.2009.09.007](https://doi.org/10.1016/j.jeurceramsoc.2009.09.007).

- [39] Emilie Courcot, Francis Rebillat, Francis Teyssandier, and Caroline Louchet-Pouillier. “Stability of rare earth oxides in a moist environment at high temperatures-Experimental and thermodynamic studies. Part I: The way to assess thermodynamic parameters from volatilisation rates”. In: *Journal of the European Ceramic Society* 30.9 (2010), pp. 1903–1909. ISSN: 09552219. DOI: [10.1016/j.jeurceramsoc.2010.02.011](https://doi.org/10.1016/j.jeurceramsoc.2010.02.011).
- [40] R B Potts and C. Domb. “Some generalized order-disorder transformations”. In: *Mathematical Proceedings of the Cambridge Philosophical Society* 48.01 (1952), p. 106. ISSN: 0305-0041. DOI: [10.1017/S0305004100027419](https://doi.org/10.1017/S0305004100027419).
- [41] Barry A Cipra. “An Introduction to the Ising Model”. In: *The American Mathematical Monthly* 94.10 (1987), p. 937. DOI: [10.2307/2322600](https://doi.org/10.2307/2322600).
- [42] Eric R Homer, Veena Tikare, and Elizabeth A Holm. “Hybrid Potts-phase field model for coupled microstructural – compositional evolution”. In: *Computational Materials Science* 69 (2013), pp. 414–423. ISSN: 0927-0256. DOI: [10.1016/j.commatsci.2012.11.056](https://doi.org/10.1016/j.commatsci.2012.11.056).
- [43] Z. A. Jones, P. Sarin, R. P. Haggerty, and W. M. Kriven. “CTEAS: A graphical-user-interface-based program to determine thermal expansion from high-temperature X-ray diffraction”. In: *Journal of Applied Crystallography* 46.2 (2013), pp. 550–553. ISSN: 00218898. DOI: [10.1107/S0021889813002938](https://doi.org/10.1107/S0021889813002938).
- [44] Johannes Schindelin et al. “Fiji: an open-source platform for biological-image analysis”. In: *Nature methods* 9.7 (2012), pp. 676–682.
- [45] Fivos Perakis et al. “Diffusive dynamics during the high-to-low density transition in amorphous ice”. In: *Proceedings of the National Academy of Sciences* 114.31 (2017), pp. 8193–8198. ISSN: 0027-8424. DOI: [10.1073/pnas.1705303114](https://doi.org/10.1073/pnas.1705303114). eprint: <https://www.pnas.org/content/114/31/8193.full.pdf>. URL: <https://www.pnas.org/content/114/31/8193>.
- [46] Lawrie B Skinner, Chris J Benmore, and John B Parise. “Area detector corrections for high quality synchrotron X-ray structure factor measurements”. In: *Nuclear Instruments and Methods in Physics Research Section A: Accelerators, Spectrometers, Detectors and Associated Equipment* 662.1 (2012), pp. 61–70.
- [47] B. H. Toby and R. B. Von Dreele. “GSAS-II: the genesis of a modern open-source all purpose crystallography software package”. In: *Journal of Applied Crystallography* 46.2 (2013), pp. 544–549.
- [48] S Stecura and W.J. Campbell. *Thermal expansion and phase inversion of rare-earth oxides*. Tech. rep. U.S. Atomic Energy Commission: Divison of Technical Information Extension, 1960. DOI: [10.2172/4840970](https://doi.org/10.2172/4840970).

- [49] dos Santos e Lucato SL, Sudre OH, and Marshall DB. “A method for assessing reactions of water vapor with materials in high-speed, high-temperature flow”. In: *J. Am. Ceram. Soc.* 94 (2011), s186–s195. DOI: [10.1111/j.1551-2916.2011.04556.x](https://doi.org/10.1111/j.1551-2916.2011.04556.x).
- [50] Elizabeth J Opila and Dwight L Myers. “Alumina volatility in water vapor at elevated temperatures”. In: *Journal of the American Ceramic Society* 87.9 (2004), pp. 1701–1705. ISSN: 00027820. DOI: [10.1111/j.1551-2916.2004.01701.x](https://doi.org/10.1111/j.1551-2916.2004.01701.x).
- [51] Geiger GH and Poirier DR. *Transport phenomena in metallurgy*. Vol. 63. Addison-Wesley Reading, MA, 1973.
- [52] Gaskell D. *An introduction to transport phenomena in materials engineering*. Momentum Press New York, NY, 2012.
- [53] P Chartrand S A Deckerov G Eriksson A E Gheribi K Hack I H Jung Y B Kang J Melançon A D Pelton S Petersen C Robelin. J Sangster C. W. Bale E. Bélisle and M-A. Van Ende. “Factsage Thermochemical Software and Databases, 2010 – 2016”. In: *Calphad* 54 (2016), pp. 35–53.
- [54] Hans J. Seifert et al. “Yttrium silicate coatings on chemical vapor deposition-SiC-precoated C/C-SiC: Thermodynamic assessment and high-temperature investigation”. In: *Journal of the American Ceramic Society* 88.2 (2005), pp. 424–430. ISSN: 00027820. DOI: [10.1111/j.1551-2916.2005.00077.x](https://doi.org/10.1111/j.1551-2916.2005.00077.x).
- [55] ANSYS® Academic Research CFX, Release 18.1. URL: [ansys.com](https://www.ansys.com).
- [56] Svehla RA. “Estimated viscosities and thermal conductivities of gases at high temperatures”. In: *NASA Tech Reports* R-132 (1962).
- [57] Slattery JC and Bird RB. “Calculation of the diffusion coefficient of dilute gases and of the self-diffusion coefficient of dense gases”. In: *AIChE J.* 4.2 (1958), pp. 137–142.
- [58] H. C. Graham and H. H. Davis. “Oxidation/Vaporization Kinetics of Cr_2O_3 ”. In: *Journal of the American Ceramic Society* 54.2 (1971), pp. 89–93. ISSN: 0002-7820. DOI: [10.1111/j.1151-2916.1971.tb12225.x](https://doi.org/10.1111/j.1151-2916.1971.tb12225.x).
- [59] Golden RA, Mueller K, and Opila EJ. “Thermochemical stability of $\text{Y}_2\text{Si}_2\text{O}_7$ in high-temperature water vapor”. In: *J. Am. Ceram. Soc.* (2020).
- [60] M. Wada, T. Matsudaira, N. Kawashima, D. Yokoe, T. Ogawa, S. Kitaoka, and M. Takata. “Mass transfer in $\text{Yb}_2\text{Si}_2\text{O}_7$ under oxygen and water vapor potential gradients at high temperatures”. In: *43rd International Conference and Exposition on Advanced Ceramics and Composites*. 2019.

- [61] Emilie Courcot, Francis Rebillat, Francis Teyssandier, and Caroline Louchet-Pouillier. “Stability of rare earth oxides in a moist environment at elevated temperatures-Experimental and thermodynamic studies. Part II: Comparison of the rare earth oxides”. In: *Journal of the European Ceramic Society* 30.9 (2010), pp. 1911–1917. ISSN: 09552219. DOI: [10.1016/j.jeurceramsoc.2010.02.012](https://doi.org/10.1016/j.jeurceramsoc.2010.02.012).
- [62] FF Lange and DR Clarke. “Morphological changes of an intergranular thin film in a poly crystalline spinel”. In: *Journal of the American Ceramic Society* 65.10 (1982), pp. 502–506.
- [63] Jürgen Rödel and Andreas M Glaeser. “Anisotropy of grain growth in alumina”. In: *Journal of the American Ceramic Society* 73.11 (1990), pp. 3292–3301.
- [64] Steve Plimpton, Aidan Thompson, and Alex Slepoy. *Stochastic Parallel PARTicle Kinetic Simulator*. 2012.